Abstract

The dynamics of vortex flow in confined geometries can be explored with weak-pinning channels of superconducting a-NbGe surrounded by strong-pinning NbN channel edges. Periodic constrictions of the channel walls lead to strong oscillations of the critical current, which we observe through transport measurements of the vortex dynamics. We explore the role of the shape and periodicity of the confining potential, as well as intervortex interactions, by fabricating a variety of samples that me measure over a range of temperatures. We have also fabricated asymmetric weak-pinning channels in a superconducting thin-film strip. We present measurements of vortex dynamics in the channels and compare these with similar measurements on a set of uniform-width channels. While the uniform-width channels exhibit a symmetric response for both directions through the channel, the vortex motion through the asymmetric channels is quite different, with substantial asymmetries in both the static depinning and dynamic flux flow. This vortex ratchet effect has a rich dependence on magnetic field and driving force amplitude. By varying the channel geometry and configuration, we are able to explore our model for the asymmetric confinement of the vortices in the ratchet. At high vortex densities, vortex interactions both within channels and between vortices in neighboring channels can often lead to a reversal of the effective ratchet potential and a strong enhancement of ratchet signal. These effects may be due to the vortex collective motions at such high vortex density regimes. Our findings demonstrate the rich dynamics of vortex interactions in confined geometries and asymmetric potential landscapes. We address the edge barrier effect and propose the future directions and the potential methods to avoid this effect.

Vortex Dynamics in Nanostructured Superconducting Weak-Pinning Channels

BY

KANG YU

B.S. Central University for Nationalities Beijing, 1998

DISSERTATION

Submitted in partial fulfillment of the requirements for the
degree of Doctor of Philosophy in Physics
in the Graduate School of Syracuse University

May 2010

Approved ________________________
Prof. Britton Plourde

Date ________________________

Copyright 2010 Kang Yu

All rights Reserved

Committee Approval Page

Contents

1 Overview **1**

2 Brief survey of superconductivity and vortex physics **5**

2.1 Introduction 5

2.2 Key properties of vortices 9

3 Superconducting nanostructures for controlling vortex dynamics **15**

3.1 Introduction 15

3.2 Survey of studies of vortices in periodic pinning structures 16

3.2.1 Nanoscale holes 16

3.2.2 Magnetic dots 20

3.2.3 Other periodic pinning lattice 21

3.3 Summary of previous work on weak-pinning channels 27

3.4 Conclusion 32

4 Superconducting nanostructures with asymmetric pinning potentials: vortex ratchets **33**

4.1 Introduction 33

4.1.1 Rocking ratchet 34

4.2 Survey of vortex ratchets 36

4.2.1 Antidots 37

4.2.2 Asymmetry in pinning density 43

4.2.3 Magnetic dots 45
4.2.4 Ratchet reversal 48
4.3 Conclusion 51

5 Fabrication and measurement scheme 53
5.1 Sample fabrication 53
5.2 Transport measurements 55

6 Vortex dynamics in weak-pinning channels with periodic constrictions 59
6.1 Introduction 59
6.2 Channel configuration 60
6.3 Edge barrier effects on critical currents 62
6.4 Critical current oscillation with controlling confinement 69
6.4.1 Mkrtchyan model for calculating the potential energy in a diamond cell 69
6.4.2 Temperature variation 70
6.4.3 Channel shape variation 72
6.5 Magnetic hysteresis 76
6.6 Dynamical hysteresis in IVCs around the matching peaks 79
6.7 Conclusion 81

7 Asymmetric weak-pinning superconducting channels: vortex ratchets 83
7.1 Introduction 83
7.2 Sample characteristics 84
7.3 Theoretical treatment - calculate potential energy of a vortex with Mkrtchyan model 86
7.4 Critical current measurements on uniform channels 87
7.5 Critical current measurements on ratchet channels 90

7.6 Dynamical flux-flow state - measurement of ratchet rectification signal 91
7.7 Magnetic hysteresis in ratchet channels 97
7.8 Conclusion 98

8 Controlling confinement and interactions in weak-pinning vortex ratchet channels 101

8.1 Introduction 101
8.2 Channel spacing 102
8.3 Ratchet cell shape 106
8.4 Temperature 109
8.5 Ratchet reversals - results and discussion 111
8.6 Conclusion 113

9 Commensurability in weak-pinning ratchet channels with small cell sizes 115

9.1 Introduction 115
9.2 Commensurability effects in ratchet channel measurements 116
9.3 Conclusion and future work 122
  9.3.1 Future directions and challenges 122
  9.3.2 Conclusion 129

Bibliography 131

List of Figures

2.1 Phase diagram of superconductivity 6
2.2 Phase diagram for a type-II superconductor 7
2.3 Measurement of flux flow resistance 11
2.4 An IVC showing nonlinearities at the high flux-flow velocities. 12

3.1 The magnetization curves and pinning force of the antidots 18
3.2 $I_c(H)$ curves for two different current directions 19
3.3 Origin of antidots pinning enhancement 20
3.4 $\rho(B)$ curve of a Nb thin film with Ni dots 21
3.5 The structure of a fivefold Penrose lattice 22
3.6 Image of antidots 23
3.7 $I_c(B)$ for different antidots arrangements 24
3.8 Images of diluted antidot arrays 25
3.9 Sketches of the vortex motion 26
3.10 Irreversibility on a $E - J$ curve 27
3.11 Schematic of vortex lattice in a superconducting channel 28
3.12 $F_p(b)$ curve and continuum model 29
3.13 IVCs in mode-locking measurement 30
3.14 Number of vortex rows in mode-locking measurement 31
3.15 Phase diagram in vortex melting measurement 31

4.1 Schematic of sawtooth potential surface 35

4.2 Diagram of surface thickness ramp ratchet 37
4.3 Simulation results of vortex ratchet response 38
4.4 Contour plot of ratchet rectification 39
4.5 V_{dc} response of an inertia ratchet 41
4.6 V_{dc} showing two rectification peaks 42
4.7 Antidot temperature dependence 43
4.8 Simulation of V_{dc} in asymmetric pinning density 44
4.9 Potential landscape of arrow-shaped pinning lattice 44
4.10 V_{dc} of vortex ratchet with triangular magnetic dots 46
4.11 V_{dc} of vortex ratchet with triangular Co ringlike magnetic dipoles . . 47
4.12 Reversal ratchet with triangular magnetic dots 48
4.13 Multiple ratchet reversals 49

5.1 Fabrication schematic on a bilayer film 53
5.2 Schematic of channel strips 54
5.3 Schematic of measurement setup 55
5.4 IVC measurement scheme 56

6.1 SEM and strip layout 60
6.2 $I_c(H_a)$ of uniform channel 62
6.3 $\bar{B}(H_a)$ with edge barrier 63
6.4 Schematic of a strip 64
6.5 Current density without dome regime 65
6.6 Bare NbGe full field sweep 66
6.7 Flux-density and current density in the dome regime 67
6.8 $I_c(H_a)$ of uniform channels commensurability effect 68
6.9 Contour plot of model potential 70
6.10 $I_c(H_a)$ for a complete field cycle 71
6.11 $I_c(H_a)$ for different T 72

6.12 Schematic of flux distribution 73
6.13 $I_c(H_a)$ with different p 74
6.14 A set of $I_c(H_a)$ for different T 75
6.15 Bare NbGe $I_c(H_a)$ complete retrace 76
6.16 Magnetic hysteresis experiment definition 77
6.17 $I_c(H_a)$ with magnetic hysteresis 78
6.18 Dynamical hysteresis in IV curve 79

7.1 Schematic of strip 84
7.2 AFM of a ratchet cell 85
7.3 Contour plot of model potential for a ratchet cell 87
7.4 $I_c(H_a)$ of uniform channels with linear fit as small fields 88
7.5 $I_c(H_a)$ of uniform and ratchet channels 89
7.6 $I_c(H_a)$ at small and large fields 90
7.7 V_{dc} measurement scheme 92
7.8 V_{dc} *vs.* I_{ac} and H_a for a ratchet sample 92
7.9 $V_{dc}(I_{ac})$ curves at different H_a 93
7.10 IVC out to Larkin-Ovchinnikov instability 94
7.11 A schematic of the linear potential 95
7.12 $V_{dc}(H_a)$ line cut of a ratchet sample with a full field sweep 96
7.13 Schematic of Meissner screening currents 97
7.14 $I_c(H_a)$ and $V_{dc}(H_a)$ of ratchet sample with magnetic hysteresis 98
7.15 Density plot of a ratchet sample with magnetic hysteresis 99

8.1 Density plots with different s 103
8.2 $V_{dc}(H_a)$ line-cuts of different s 104
8.3 $1/H_p$ *vs.* s of ratchet samples 105
8.4 $V_p(s)$ of ratchet samples 105
8.5 Schematic showing different taper shape 106

8.6 $V_{dc}(H_a)$ for different ratchet cell shape 107
8.7 $V_p(b)$ of ratchet samples 107
8.8 $I_c/I_c(0)$ $vs.$ H_a for different b 108
8.9 Maximum ratchet signal as a function of b 109
8.10 λ_{NbGe} $vs.$ T 109
8.11 $V_{dc}(H_a)$ at different T 110
8.12 $V_{dc}(H_a)$ line-cuts of ratchet reversal 111
8.13 $V_{dc}(H_a/H_p)$ line-cuts of ratchet reversal 112
8.14 Ratchet reversal onset field 113

9.1 AFM emage of small size ratchet cell 116
9.2 Density plot of ratchet signal with strong oscillation 117
9.3 Density plot of characteristic frequency of ratchet oscillations 118
9.4 $I_c/I_c(0)(H_a)$ of ratchet samples with different p 118
9.5 Density plots of ratchet signal for different p 119
9.6 Matching fields for different p 120
9.7 $I_c/I_c(0)(H_a)$ of ratchet samples for different s 120
9.8 Density plots of ratchet signal for different s 121
9.9 Matching fields for different s 122
9.10 Corbino measurement setup 124
9.11 SQUID voltmeter mechanism 126
9.12 Corbino measurement data 128

List of Tables

6.1 Diamond shaped samples 61
6.2 Number of dynamic hysteresis 80

Acknowledgments

It is my pleasure to thank all the people who have helped me during my study in Syracuse. First I would like to thank my thesis advisor Britton Plourde for giving me the opportunity to work on such an exciting project and the advices and the encouragements he has given. I also like to thank Tom Heitmann, who had largely involved in the project and shared the best movies and fishing techniques with me. I would like to thank other members in my research group for numerous help during the years. Specially, I would like to thank Chunhua Song for a large amount of work she had done to setup the measurement inset, and Mike DeFeo for building the first current box. I would like to thank our collaborators at Leiden University, Marcel Hesselberth for sputtering the superconducting films for us and Peter Kes for useful discussing and suggestions.

A special thank goes to Arny Honig. He has influenced me in ways ranging from physics to farming, but most importantly is an optimistic life attitude. I also want to thank Arny for inviting me to his Thanksgiving dinners every year. I would like to thank Peter Saulson for his academic mentoring. I also want to thank Lou Buda, Charles Brown, Phil Arnold and Lester Schmutzler for their generous help.

I would like to thank my uncle Anyong Xie for his support both before and after I came to the US. I also like to thank my parents for respecting my career choices and encouraging me to pursue them. Last but not least, I would like to thank my wife for her complete support and understanding throughout the years, and thank my 19-month old daughter for all the joys she brought to me.

Chapter 1

Overview

Recent advances in nanofabrication have led to tremendous possibilities for implementing superconducting pinning structures and controlling the motion of vortices. The dynamics of vortices in confined superconductor geometries has generated much interest, including studies of fundamental properties with vortex matter and devices being based on the motion of the vortices. However a complete appreciation of their properties is an intricate matter. An understanding of vortex interactions, both vortex-vortex interactions and interactions between vortices and their surrounding environments, may allow for the control of vortex dynamics at the mesoscopic scale.

We have fabricated strips with weak-pinning channels across the width for guiding vortices in the presence of transport currents. The vortex dynamics were studied through the standard four-probe measurement technique. The critical current that characterizes the transition from the static state to the flux flow regime was measured as well as the current-voltage characteristics (IVC). Varying the channel geometry and measurement parameters, such as current amplitude, vortex density, and temperature, we can probe the vortex behavior directly.

This thesis presents our investigations of the vortex dynamics in superconducting weak-pinning channels. In Chapter 2, I survey some of the relevant basic concepts of superconductivity, including the Meissner effect, the Ginzburg-Landau theory for providing a phenomenological description of superconductivity and the BCS theory for providing a microscopic theory of superconductivity. I also discuss the vortex response in a superconductor and the relevant concepts for describing vortex dynamics, such as the flux flow resistivity, the vortex pinning by defects, and the Lorentz force caused by applying a transport current to the vortices.

I continue with reviews of previous work on periodic pinning and vortex ratchet effects in Chapter 3 and 4 respectively. Chapter 3 is a review of recent studies on periodic pinning in superconductors. Both theoretical and experimental investigations will be included. I discuss different implementations of artificial pinning in superconducting films, including submicron pinning holes, magnetic dots, and different pinning arrangements of periodic and quasiperiodic pinning arrays. I then introduce the measurements of weak-pinning channels. I compare the different approaches among them and explain the experimental results as well as theoretical simulations.

A review of the studies of the ratchet effect will be presented in Chapter 4. I introduce the ratchet effect in general, then discuss the characteristics of a rocking ratchet, which has an asymmetric spatial potential energy, and can exhibit directed motion when an oscillatory drive is applied to the system. Subsequently, I focus on the discussion of vortex ratchets. I discuss various theoretical proposals and the corresponding experimental implementations. Strong ratchet effects have been demonstrated in numerous experiments. In some cases, there can be the surprising result that the rectification occurs in the opposite direction from what one would expect based on the sense of the asymmetry in the potential.

I introduce the basic experimental techniques used in the experiments in Chapter 5. The standard four-probe approach for measuring IV-curves and the critical current will be presented. In Chapter 6, I present our measurement of vortex dynamics in superconducting weak-pinning channels with periodic constrictions, where even spaced channels, with each channel formed by multiple diamond-shaped cells, were measured with the transport measurement technique. We have studied channels with various periodicities and channel spacing. Interesting features, including strong commensurability in the field dependence of the critical current, magnetic hysteresis in the critical current, and dynamical hysteresis in the vortex motion through the channels are presented in this chapter. I also address some of the influences on edge barrier effects in our results.

The implementation of a vortex ratchet with superconducting weak-pinning channels is presented in Chapter 7. The channels are similar designs to the ones in Chapter 6, but the cells are triangular in shape, forming an asymmetric potential landscape. Strong ratchet effects were observed in our measurements. A rough model of the potential for a vortex in the ratchet cell was proposed. The transition from the static state to dynamical state is investigated in the confined channels. A study of the magnetic hysteresis for these samples shows interesting results both on the critical current and the net vortex drift in response to an oscillatory driving force.

In Chapter 8, I present the experimental studies of the ratchet effects by varying the ratchet parameters, including the ratchet cell shape, channel spacing and the measurement temperatures. Subsequently, we investigate the ratchet response at high vortex densities where we often observe a strong enhancement of the ratchet signal and can sometimes lead to a reversal of the effective ratchet potential. These effects may be due to collective interactions of vortices and I present measurement data in various high vortex density regimes.

I discuss the commensurability in the critical current field dependence in Chapter 9 while we vary the cell period and channel spacing in a set of ratchet samples. Commensurabilities were particularly strong at small cell lengths. I present our measurement results for various sample parameters. The limitations and complications of our experiments are given, particularly with regard to the edge barrier effect. I propose future research directions in which the edge barrier can be avoided with closed circular channels on a Corbino disk geometry. I also present the necessary measurement tool – a picovoltmeter, which we developed by utilizing a Superconducting QUantum Interference Device (SQUID), for probing the flux-flow motion of a small number of vortices at low velocities where the flux-flow voltage is too weak to be observed with a room-temperature amplifier.

Chapter 2

Brief survey of superconductivity and vortex physics

2.1 Introduction

Almost one hundred years ago on April 8, 1911, H. Kamerlingh Onnes discovered superconductivity in liquid helium in Leiden, where zero resistivity of mercury was measured [1, 2]. In his notebook, he wrote "resistance practically zero" [2]. He referred to the phenomenon of zero-resistivity as superconductivity. Subsequent measurements of the resistance for other materials at the liquid helium temperature were performed, and many more metals and alloys were found since then to be superconducting below a well-defined critical transition temperature T_c, or characteristic of the corresponding metals.

More than 20 years after superconductivity was first discovered, Meissner and Ochsenfeld revealed another hallmark of superconductivity in which they discovered the 'perfect diamagnetism' in 1933 [3]. They found that applied magnetic fields will be excluded from entering a superconductor, as one would expect from perfect conductivity. But strikingly, they also discovered that the applied magnetic field at the normal state will be expelled when the superconductor is cooled through T_c.

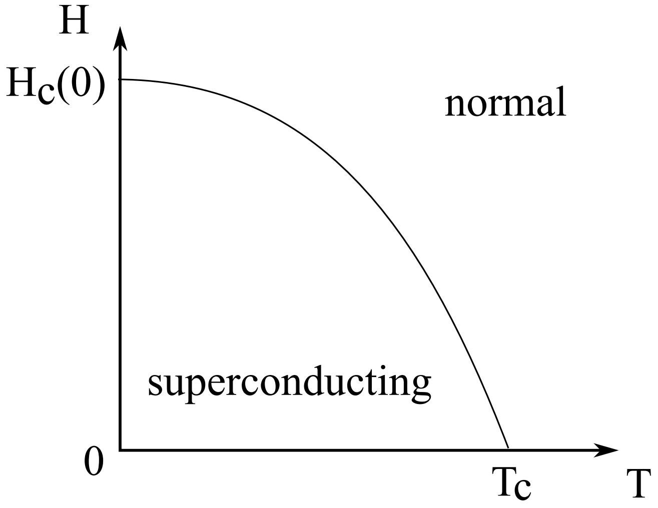

Figure 2.1: $H_c(T)$ showing the phase diagram of superconductivity.

This Meissner effect is independent of whether there was a magnetic field before the superconducting transition or if the field was switched on later, which implies that a critical magnetic field H_c can destroy superconductivity. This critical field H_c separates the normal and superconducting states by a thermodynamic phase-transition (Fig. 2.1).

The first successful phenomenological theory of superconductivity was published in 1935 by brothers F. and H. London [4]. Their theory described two basic electrodynamic properties of superconductivity concerning the characteristics of a perfect conductivity and the Meissner effect. The second London equation also introduced the penetration depth λ, characterizing a length scale over which a magnetic field is exponentially decreased into the superconductor.

Ginzburg and Landau (GL) introduced a theory of the superconducting phase transition in 1950 [5]. In this theory, the superconducting electron density n_s was described by a wave-function ψ

$$n_s = |\psi(x)|^2. \tag{2.1}$$

Another important length scale in superconductivity introduced in the GL theory is coherence length ξ, which characterizes the distance over which the superconducting order parameter can vary. The coherence length ξ is found to diverge as the temperature approaches T_c:

$$\xi \propto (T_c - T)^{-1/2} \tag{2.2}$$

The superconducting order parameter κ was defined in the GL theory by the ratio of the two characteristic lengths

$$\kappa = \frac{\lambda}{\xi} \tag{2.3}$$

One cannot have a general form for describing the temperature dependence of $\lambda(T)$ in terms of the $\lambda(0)$ due to the variation of κ at the zero temperature for different metals [6]. But the dependence based on the "two-fluid" model can practically fulfill the experiment purposes in the limit that the measurement temperature is not close to $T = 0$. Thus $\lambda(T)$ can be described as

$$\lambda(T) \approx \lambda(0)[1 - (T/T_c)^4]^{-1/2}. \tag{2.4}$$

In 1957, based on the GL theory, Abrikosov proved the existence of a so-called intermediate state in type-II superconductors [7]. In this mixed phase of superconducting, above the first transition field H_{c1}, a continuous increase in the flux density

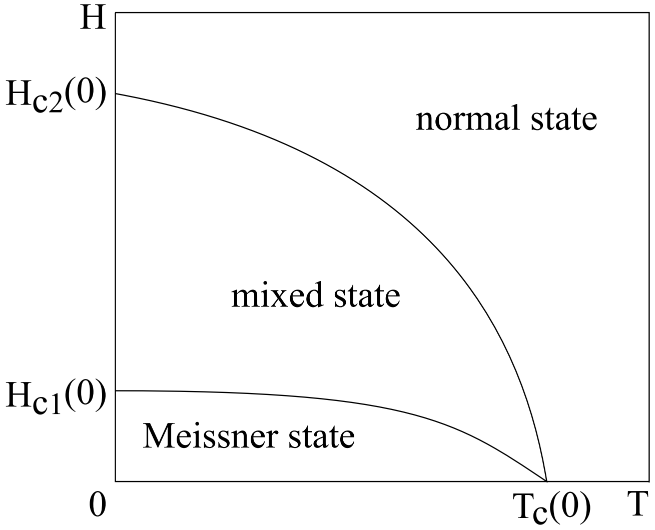

Figure 2.2: Phase diagram for a type-II superconductor.

is expected until the B field reaches another critical field H_{c2}, eventually destroying the superconductivity and entering the normal state (Fig. 2.2). The transition between type-I and type-II superconductivity is well defined by the GL order parameter at $\kappa = 1/\sqrt{2}$. For a pure superconductor, $\kappa \ll 1$, whereas $\kappa > 1/\sqrt{2}$ for a type-II superconductor. Abrikosov also found that the magnetic flux in the mixed state of a type-II superconductor must be quantized in a single quantum of flux

$$\Phi_0 = \frac{h}{2e} = 2.07 \times 10^{-15}\ T - m^2. \tag{2.5}$$

It is often more practical experimentally to work with Φ_0 in CGS units with lengths in μm, because the length and the field in the experiments are usually measured in μm and Oe respectively. In this case, $\Phi_0 = 20.7$ Oe$-\mu m^2$. Each flux is called a vortex, such that the supercurrent circulating around the vortex concentrates the flux toward its core where the order parameter vanishes.

The GL theory is crucial for understanding the macroscopic quantum-mechanical nature of superconductivity. After J. Bardeen, L. N. Cooper and J. R. Schrieffer (BCS) first introduced 'Cooper pairs' in 1957, the microscopic theory of superconductivity finally moved a revolutionary step [8]. At the superconducting state, electrons tend to bind in pairs, thereby having a lower energy level than in the Fermi-sea ground state. The electrons in Cooper pairs interact by exchanging phonons. The BCS theory predicted that a minimum energy $E_g = 2\Delta(T)$ is required to break the Cooper pairs from the ground state. $\Delta(T)$ is the energy gap between the ground state and the quasi-particle excitations of the system, in the order of kT_c, where k is the Boltzmann constant. In 1959, Gor'kov was able to show that the GL theory is a limiting form of the BCS theory when the temperature is near T_c [9].

It is possible to calculate the superconducting parameters in the case of dirty metal, in which the electronic mean free path is shorter than the coherence length. Therefore, the band-structure complication can be neglected in such dirty superconductors [9, 10]. Measuring the slope of $H_{c2}(T)$ at the temperature near T_c,

$$S \equiv -\mu_0 \frac{dH_{c2}}{dT} |_{T_c}, \tag{2.6}$$

where μ_0 is the magnetic permeability in a vacuum, and applying the BCS expressions in Tinkham [6], at zero temperature, one can obtain the effective coherence length $\xi(0)$ and effective penetration depth $\lambda(0)$ [10]:

$$\xi(0) = 1.81 \times 10^{-8} (T_c S)^{-1/2}, \tag{2.7}$$

$$\lambda(0) = 1.05 \times 10^{-3} (\rho_0 / T_c)^{1/2}, \tag{2.8}$$

in SI units such that $[S] = TK^{-1}$, $[\rho_0] = \Omega\ m$ and $[\xi(0)] = [\lambda(0)] = m$.

2.2 Key properties of vortices

Vortex lattice

As described previously, each vortex is surrounded by a circulating screening current. The vortices in a bulk superconductor experience a repulsive force from neighboring vortices due to the interaction with the circulating current. When the vortex spacing is comparable to the penetration depth λ, the vortices will form a triangular array in order to maintain the lowest energy of intervortex interaction. And the triangular lattice constant a_0 can be described as:

$$a_0 = \left(\frac{2}{\sqrt{3}} \right)^{1/2} \sqrt{\frac{\Phi_0}{B}}. \tag{2.9}$$

a_0 is about 5 μm for $B = 1$ G.

Lorentz force

In an ideal bulk superconductor, where there is no pinning of any kind and no surface or edges, any non-zero current applied to the vortex can lead to the movement of the flux lines through the interaction between the applied current and the circulating current around the vortex. The behavior of vortices threaded in a superconductor can be probed by measuring the transport properties. A current density **J** exerts a Lorentz force on a vortex:

$$\mathbf{F_L} = \mathbf{J} \times \Phi_0 \hat{\mathbf{n}}. \tag{2.10}$$

where Φ_0 is the flux quantum, $h/2e$.

Flux-flow

Because the superconductivity is suppressed in the vortex core, the motion of vortices generates a longitudinal voltage, transverse to the direction of the vortex flow. This movement will generate an electrical field that is parallel to the applied current, thus causing the vortex motion to create a non-zero resistance. The flux flow of vortices leads to a dissipation, which can be characterized by the vortex viscosity:

$$\eta = \frac{\Phi_0 B_{c2}}{\rho_n} \tag{2.11}$$

where ρ_n is the normal-state resistivity of the material, and B_{c2} is the upper-critical field [6],[11]. The vortex effective mass is expected to be small enough so that it can only play a role in the vortex motion at an extremely high frequency [12]. Thus, appropriately placed electrical leads can be used to probe this flux-flow voltage. After first treated by Bardeen and Stephen [11], Kim *et al.* [13] experimentally confirmed the flux-flow resistance in type-II superconductors (Fig. 2.3). The sheet resistances of superconducting NbTa and PbIn were measured with the standard transport measurement technique. Section 5.2 will introduce the transport measurement techniques and necessary procedures that must be taken in order to measure the flux-flow voltage described above.

Nonlinearities at high flux-flow velocities

An electronic instability, where an abrupt switching from the superconducting state to the normal state was predicted when the flux-flow velocities in type-II supercon-

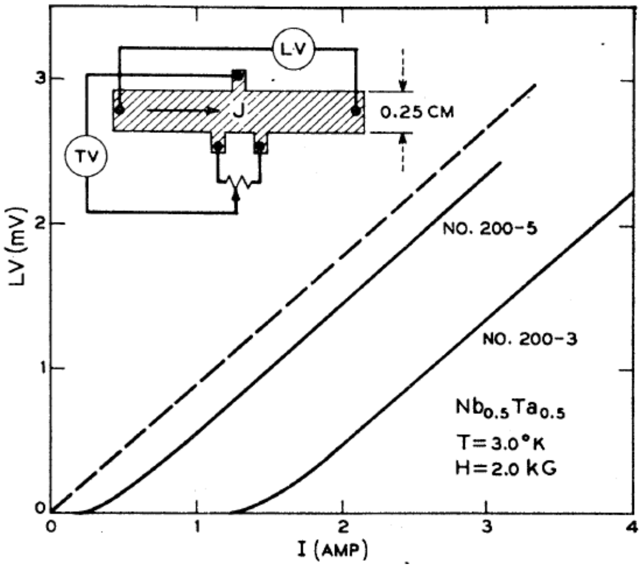

Figure 2.3: The measurement of flux flow resistance in type-II superconductors from Kim *et al.* [13]. Transport voltage LV increases linearly following an initial nonlinear response with applied current I in the type-II superconductor mixed state. Inset, the schematic of the sheet sample and measurement setup. (from Kim *et al.*, 1965, p.A1165)

ductors reach a certain critical limit [14]. Larkin and Ovchinnikov (LO) first reported that this switching instability was caused by the nonequilibrium distribution of the quasiparticles, rather than the instability dominated by heating. The electronic field due to the vortex motion accelerates bound quasiparticles states in the core, causing some to begin leaking out of the vortex core. This can cause the core size to shrink and cause a decrease in the vortex viscosity, thus causing an upwards curvature in the current-voltage characteristics. A generic current-voltage characteristic (IVC) is shown in Figure 2.4.

More recently, Doettinger *et al.* [15] reported the first observation of this effect in high-T_c superconductors, where they can extract the flux-flow critical voltage V^* by fitting the experiment IV characteristics with [15, 16]:

$$I - I_c = \left[\frac{V}{1 + (V/V^*)^2} + V \left(1 - \frac{T}{T_c} \right)^{1/2} \right] \frac{1}{R_f}, \tag{2.12}$$

where R_f is the flux-flow resistance. The vortex critical velocity v_φ^* and the electron-

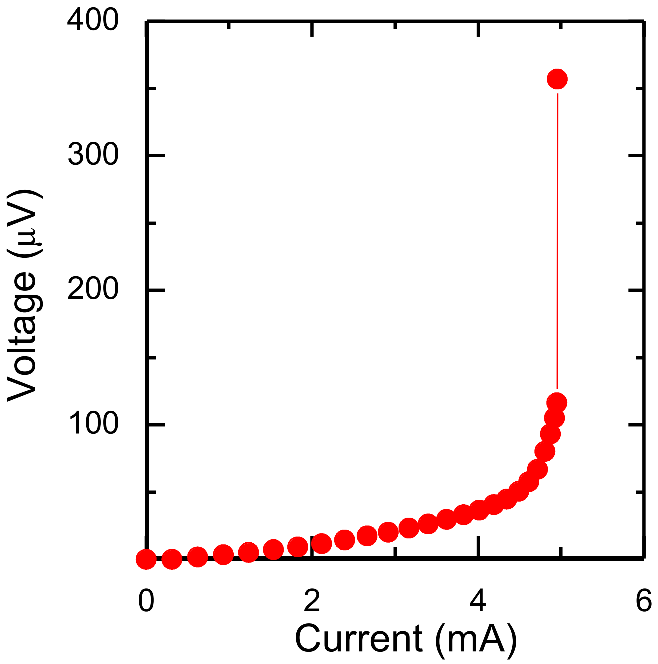

Figure 2.4: An IVC showing nonlinearities at the high flux-flow velocities.

phonon inelastic scattering time τ_{in} can be calculated with the following equation from the LO theory [14, 15]:

$$\mathbf{V}^* = -(\boldsymbol{v}_\varphi^* \times \mathbf{B})\mathbf{L}, \tag{2.13}$$

where B and L are the magnetic field and the sample length between the voltage probes. The vortex critical velocity v_φ^* is about 300 m/s for a NbGe film [17]. A more detailed treatment with consideration of the edge barrier screening effects was reported by Bezuglyj and Shklovskij [18] And the influence of barriers on the vortex entry at surfaces and edges will be discussed in Chapter 6.

Pinning

In order to have a good type-II superconductor for technological applications, so that it can carry high currents in the presence of the flux line without or with little dissipation, the flux lines have to be pinned. This can be achieved usually by artificial means, such as dislocations, radiation-induced pinning defects, materials defects, grain boundaries, nanovoids etc. More recently, with the development in nanofabrication, submicron pinning holes or magnetic dots have been implemented in superconducting thin films in order to increase pinning force. The experimental implementation of artificial pinning sites in superconducting films will be addressed in more detail in subsequent chapters.

When a vortex is near the inhomogeneities in superconductors, the force between the vortex and the defect tends to pin the vortex in place. A calculation carried out by Mkrtchyan and Schmidt shows that it is always energetic favorable for a vortex to be attracted by a cavity in the superconductors [19] before the number of trapped vortices reaches a critical value, which largely depends on the superconductor and the cavity parameters. With vortices pinned in the pinning centers, the superconductors can now sustain a finite current without flux motion and dissipation. The current at which the threshold force is required to cause vortex motion is referred to as the critical current. A more detailed discussion can be found in Chapter 3.

Thin-film superconductors

By solving the combination of the Maxwell's equation and the second London equation, at the limit of $r \gg \lambda$, where r is the distance to the vortex center, one can have the magnetic field of a vortex in a bulk superconductor as [6]:

$$h(r) \approx \frac{\Phi_0}{2\pi\lambda^2}\left(\frac{\pi}{2}\frac{\lambda}{r}\right)^{1/2} e^{-r/\lambda}, \tag{2.14}$$

where $h(r)$ decays exponentially at far distances. When the thickness of the superconductor becomes less than the London penetration length, the vortices undergo a long range vortex-vortex interaction. Pearl [20] calculated that the screening currents do not fall off exponentially in the thin-film limit, but follows a power-law through a longer thin film penetration depth instead [21]:

$$J(r) = \frac{c}{4\pi}\frac{\Phi_0}{\pi}\frac{1}{r^2} \qquad for\ r \gg \lambda_\perp \approx 2\lambda^2/d, \tag{2.15}$$

where d is the thickness of the superconductor, and $d < \lambda$.

Chapter 3

Superconducting nanostructures for controlling vortex dynamics

3.1 Introduction

Reducing the dissipation in type-II superconductors caused by the motion of vortices is an important issue for scientists. In order to achieve the lower dissipation, increasing the vortex pinning would be the first intuitive way to do so. Therefore a larger pinning force f_p and a larger critical current density j_c will be achieved in the superconductor, which can be useful for practical applications.

Recent advances in nanofabrication have enabled implementations of artificial periodic vortex pinning lattices in superconducting films. Such structures are typically produced with arrays of either nanoscale holes through the film [22, 23] or magnetic dots underneath the film [24]. These structures result in a substantial magnetic field-dependence on the critical current.

The critical current in periodic pinning structures typically exhibits commensurate behavior with maxima when the magnetic field corresponds to an integer number of vortices per pinning site. For fields away from these matching points, the dynamics of interstitial vortices, which are not located on the strong pinning sites but are more weakly confined through interactions with the strongly pinned vortices, lead to lower critical currents. Recently, a variety of experiments have been performed on such pinning arrays as well as many simulations of vortex dynamics in these periodic pinning systems.

In this chapter, I will provide highlight of previous work on periodic pinning structures, including some of the simulations and their corresponding implementations, followed by an introduction of superconducting weak-pinning channels, the structure of which will be discussed later in this thesis.

3.2 Survey of studies of vortices in periodic pinning structures

3.2.1 Nanoscale holes

One approach for controlling the vortex motion in superconductors is to create submicron holes by using lithographic and etching techniques. These submicron holes are usually referred to as "antidots" in the thin films, which act as well-defined pinning centers. The pinning holes sometimes do not perforate the film, which is also referred to as "blind dots." Mkrtchyan and Shmidt [19] studied the interaction between a vortex and a cavity in a type-II superconductor theoretically. Under the assumption of the cavity radius $r \ll \lambda$, where λ is the penetration depth, capturing a single vortex by the cavity is always energetically favorable. After a vortex has been captured, the vortex free energy undergoes a qualitative change, and it may result in a potential barrier between the vortex and the cavity so that the capture of subsequent vortices in the cavity largely depends on the superconductor and the cavity parameters, which could be energywise favored or not.

Both the square and rectangular pinning arrays were simulated numerically by Reichhardt *et al.* [25]. The simulation results indicated a strong commensuration enhancement of pinning strength, both in square and rectangular pinning arrays. For rectangular arrays, the commensurability effects at the matching fields depended on whether the driving was along the long or short direction of the arrays. In any case, the pinning force was found to be much higher along the long direction, also referred to as the “hard” direction by the authors, where the matching effects were considerably reduced. The authors also found that for higher fields, the matching effects were reduced and certain peaks were absent.

Before I discuss the experiments on the periodic pinning structures, it is worth noting that all of the antidot experiments have to be performed very close to T_c to avoid the background pinning in the film from dominating the antidot pinning potential [26]

The composite vortex lattice consisting of vortices at the antidots and interstitials was studied by Baert *et al.* [22]. The authors demonstrated the periodic arrays of antidots could be successfully used in order to stabilize such composite flux phases. The authors patterned a square lattice of submicron holes in a Pb/Ge multilayer superconductor. They studied the vortices pinned at the holes and at the interstitial positions. The authors then found that the mobility of the vortices at the interstices were strongly temperature dependent, which made it possible to see the transition between an 'insulating' (fully localized vortices) and a 'metallic' (a collective delocalized state) behavior by tuning the temperature.

In order to find the optimum size for antidots, Moshchalkov *et al.* [27] patterned arrays of submicron holes in superconducting Pb/Ge multilayer and single WGe films. The measurement of magnetization and pinning force showed strong enhancement by the arrays of antidots, as well as matching effects. It was suggested from the experiment that a pinning center with a size(diameter - D) considerably larger than the superconducting coherence length $\xi(T)$ is much more efficient than pinning centers with $D \approx \xi(T)$ (Fig. 3.1). That is, antidots with a larger size than $\xi(T)$ can provide a larger pinning force f_p, and therefore provide a larger critical current density j_c, which is important for practical applications.

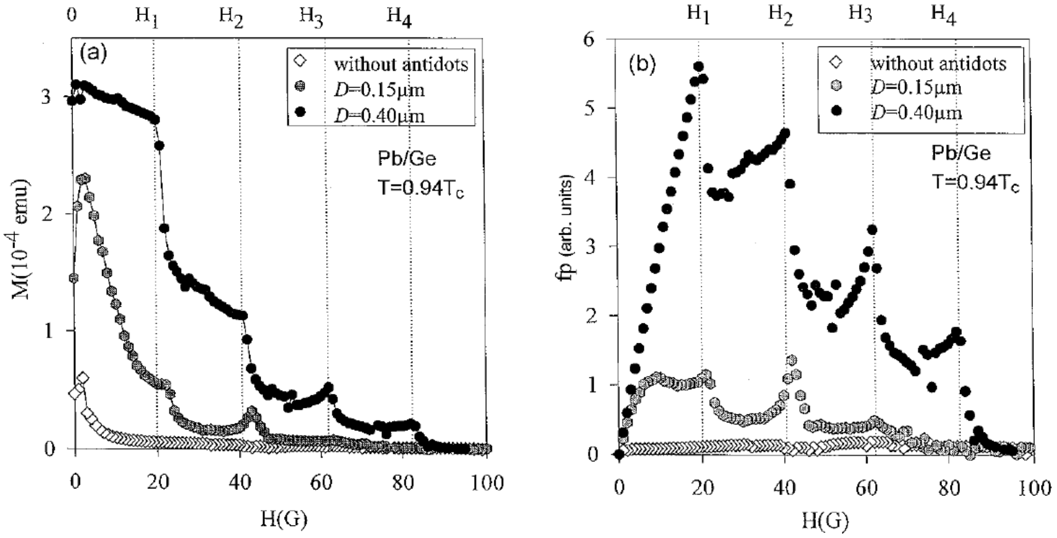

Figure 3.1: The magnetization curves and pinning force of the antidots with different diameters from Moshchalkov *et al.* [27]. (a) The magnetization curves, antidots with diameter $D = 0.15 - 0.4$ μm; (b) The pinning force vs. field. The matching fields are indicated by dashed lines. (from Moshchalkov *et al.*, 1998, p.3616)

The anisotropy in the depinning force and the commensurability effects were experimentally realized by Van Look *et al.* [28]. Instead of employing rectangular pinning arrays, authors in this paper presented measurements on square arrays with rectangular shaped submicron holes, fabricated on a superconductor Pb film by an electron-beam lithography and etching. Both blind dots and antidots were studied in this work. When a current was applied along the long direction of the rectangle, stronger matching effects were shown in both systems than if the current was applied along the short direction (Fig. 3.2). The mechanisms determining the direction was different in the two systems. In the case of the superconducting film with rectangular antidots, the vortex-vortex interaction was found to be anisotropic, which was responsible for the higher critical current. On the contrary, the vortex-vortex interaction was isotropic for the case of rectangular blind antidots. Instead, the shape of the pinning sites and the fact that a vortex could move around freely within the blind antidots caused the anisotropy in the critical current (Fig. 3.2).

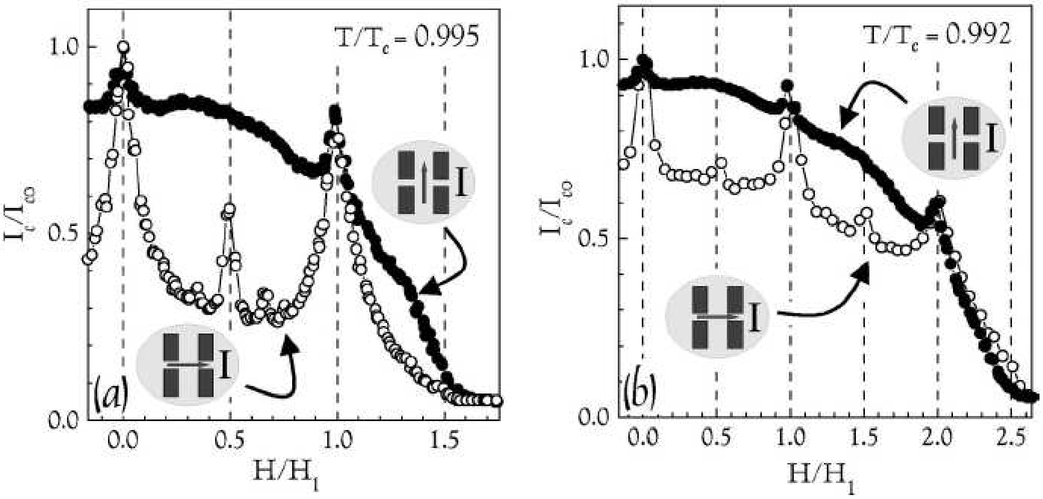

Figure 3.2: Normalized critical currents I_{cx} and I_{cy} as a function of normalized magnetic field H/H_1 from Van Look *et al.* [28], measured with a current in the x (circle) and y directions (dots), respectively. Where (a) $T/T_c = 0.995$ and (b) $T/T_c = 0.992$, and H_1 is the first matching field, corresponds to one vortex per pinning site. (from Van Look *et al.*, 2002, p.214511-2).

The enhancement of the flux pinning strength at the pinning holes is widely assumed to be responsible for the critical current commensurate enhancement. However Patel *et al.* claimed that the origin of the matching effect in such a system is a hole-induced suppression of the critical temperature instead [29]. Superconducting Nb films with triangular arrays of antidots were measured near the zero-field critical temperature, which is required for a typical antidot experiment in order to avoid the background pinning from getting too strong. At those temperatures, the coherence length ξ becomes comparable to the width of the superconductor between the holes. An experimental approach was presented, utilizing a comparison of the magnetic field dependences of the resistance $R(H)$ [Fig. 3.3(a)] and the critical temperature in perpendicular and parallel magnetic field directions. The baseline derived is based on a wire network analysis matched to the $R(H)$ curve [Fig. 3.3(b)]. The authors, then described that the matching effect where the resistance exhibited minima indeed was originated from the hole-induced T_c suppression [29].

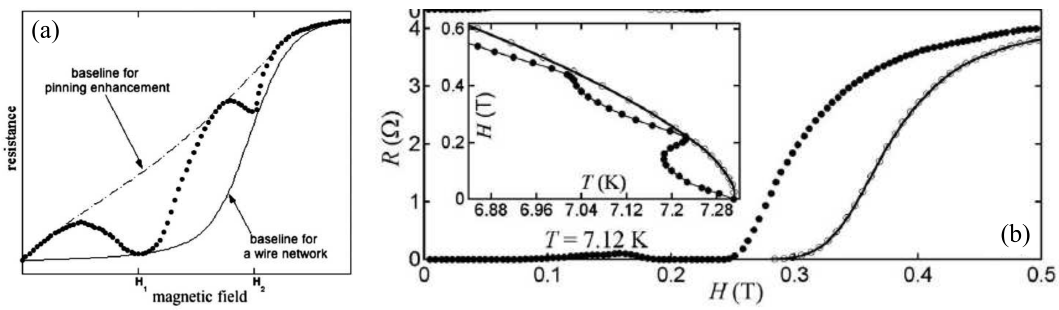

Figure 3.3: Theory proposal and measurements to demonstrate the origin of antidots pinning enhancement from Patel *et al.* [29]. (a) A proposed approach to identify the origin of the matching effect in a superconducting film with a regular hole array. The dots represent typical experimental results. (b) $R(H)$ curves at $T/T_c = 97.4\%$ and $H(T)$ phase diagram (inset) showing open circles obtained in parallel fields form the wire network baselines for those in perpendicular fields (dots). (from Patel *et al.*, 2007, p.020508-1 and p.020508-3).

3.2.2 Magnetic dots

A different approach rather than using antidots for introducing pinning centers in the superconductor is to utilize submicron magnetic dots. Devices with magnetic dots usually consist of arrays of magnetic islands (Ni, Co etc.) on superconducting films (Pb, Nb etc.). Such a system provides a useful tool in understanding the interaction between vortices and material imperfections, and enhances the critical current [30, 31].

Martín *et al.* first reported the study of the pinning interaction between the vortex lattice and ordered arrays of submicron magnetic dots [32]. A triangular array of magnetic Ni dots in a superconducting Nb film was fabricated using electron-beam lithography and liftoff techniques. Periodic minima had been observed in the resistivity as a function of the perpendicular magnetic field (Fig. 3.4), which was carried out with standard transport measurement techniques; this data indicated a strong pinning enhancement at the magnetic dots. The nature of the pinning mechanism induced by magnetic dots was principally determined either by a magnetic interaction between the magnetic dot and the magnetic moment of the vortex, or by a local suppression of the superconductivity due to the ferromagnetic proximity to the magnetic dot [32]. The authors also pointed out that the pinning is the most efficient when ξ, the coherence length, is closest to the size of the pinning site, which was proved otherwise by Moshchalkov *et al.* [27] in an experiment where arrays of antidots were measured as was aforementioned in this chapter.

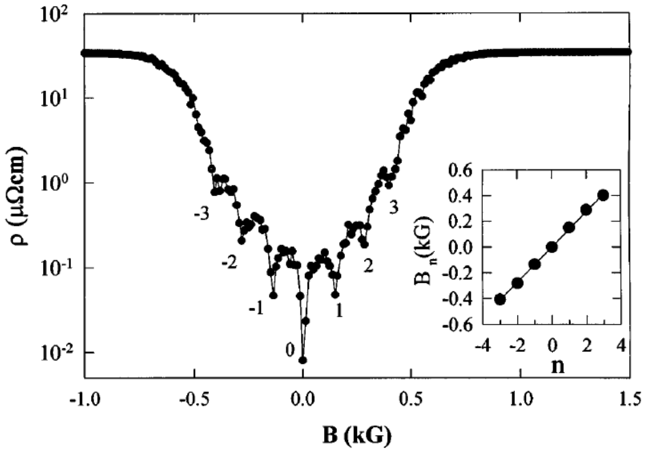

Figure 3.4: $\rho(B)$ curve of a Nb thin film with a triangular array of Ni dots from Martin *et al.* [32]. The lattice constant $d = 410$ nm, $T = 8.2$ K and $J = 2.5 \times 10^4$ A/cm^2. The inset shows essentially a linear dependence of $B_n = n\Delta B_0$ with $\Delta B_0 = 141 \pm 4$G. (from Martin *et al.*, 1997, p.1930)

Similar magnetic dots were studied by Van Bael *et al.* by utilizing magnetization hysteresis loop measurements and scanning-force microscopy [33]. In the experiment, superconducting Pb films were deposited on top of the elongated submicron Co islands. The authors demonstrated with measurement results that the magnetized islands act as strong flux pinning arrays. More studies on square or triangular arrays of magnetic dots, placed underneath or on top of the superconducting film, can be found elsewhere [24, 34, 35].

3.2.3 Other periodic pinning lattice

Periodic pinning experiments beyond the simple periodicities of the initial measurements have been intensively investigated in the last few years, and some different pinning array arrangements will be briefly discussed.

Quasiperiodic lattices

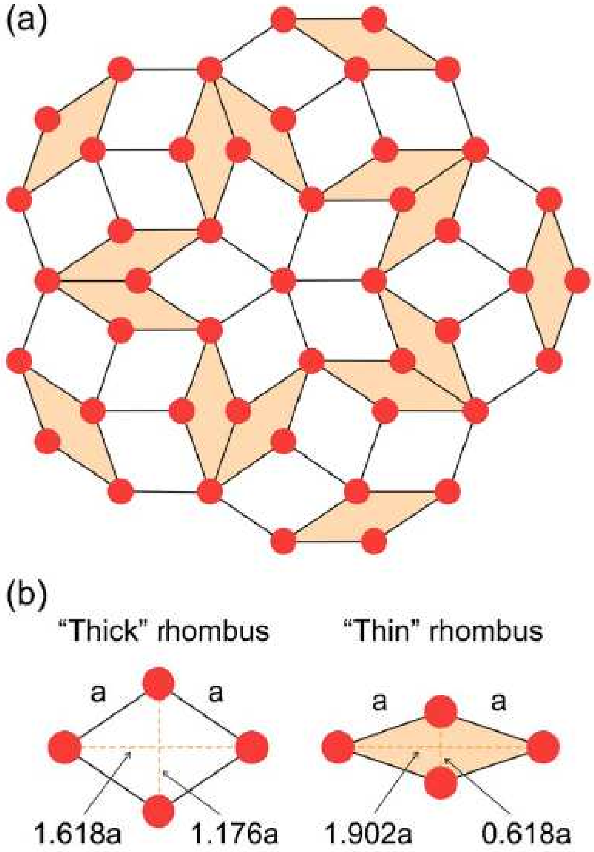

Figure 3.5: The schematic of a fivefold Penrose lattice from Misko *et al.* [36]. (a) The elemental building blocks are rhombuses with equal sides a and angles which are multiples of $\theta = 36°$ and (b) showing two kinds of rhombuses "thin" and "thick" as indicated. (from Misko *et al.*, 2006, p.024522-12)

In addition to the studies of square and triangular arrays, Misk *et al.* had studied the flux pinning interactions in chains of pinning arrays and 2D quasiperiodic, Penrose lattice (Fig. 3.5)pinning arrays [36, 37]. The enhancement of the critical current in films was observed in the simulation results, suggesting that the Penrose lattice provided a tool to control the magnitude, sharpness and position of the peaks of $J_c(\Phi)$, which is important for possible applications.

Experiments for studying such fivefold Penrose pinning arrays have been carried out widely, such as in Ref. [38–40]. I will give a brief review to these references and point out the corresponding key results.

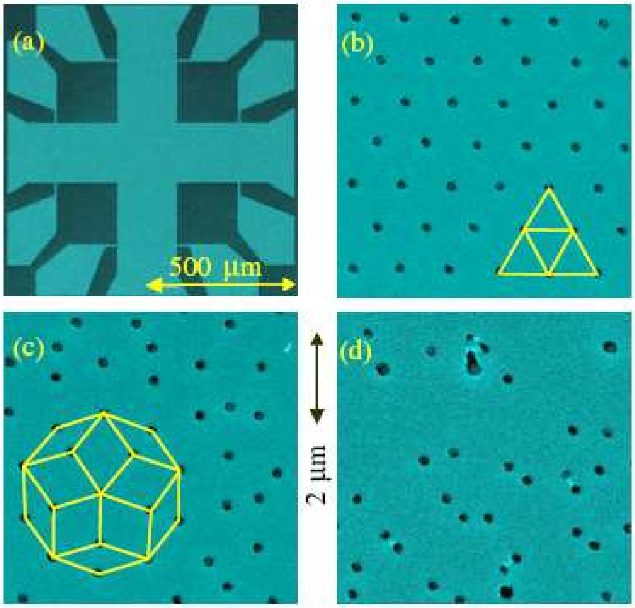

Figure 3.6: Images of antidots in different arrangements from Kemmler *et al.* [40]. (a) Nb sample strip, antidots (125 nm radius) arrays in: triangular lattice (b), Penrose lattice (c), random arrangement (d). (from Kemmler *et al.*, 2006, p.147003-2).

Villegas *et al.* had fabricated arrays of magnetic dots (Ni) in superconducting Nb films, and the magnetoresistance of samples had been studied with transport measurements. The minima of magnetoresistance appeared at the matching fields, corresponding to the increase of the flux pinning. Between the studies with two different quasiperiodic lattices: a Fibonacci sequence/Penrose and pentagonal fractal array, the authors found that the short vortex lattice (VL) correlation length existed in the Fibonacci array. On the contrary, the longer length scales were preserved in the pentagonal fractal array [38]. This implied the long-range correlations of VL in the pentagonal arrays.

A direct comparison in three different periodic arrays and quasiperiodic pinning arrays of antidots in superconducting Nb films has been investigated by Kemmler *et al.* (Fig. 3.6) [40].

In this experiment, essential features in the $I_c(B)$ patterns as predicted by Misko *et al.* [37] were confirmed. There were enhancements of I_c in films with Penrose lattices, but these were not as strong as triangular antidot lattices. Since the enhancements of I_c occurred only at fields close to the matching fields, which corresponded to the artificial pinning arrays, it was possible to have well designed pinning arrays so that the critical current enhancement had a broader distribution in the magnetic field comparing to simple periodic pinning lattices (Fig. 3.7).

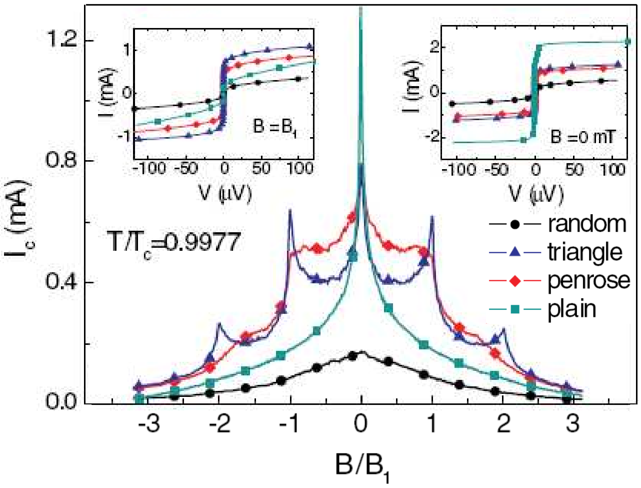

Figure 3.7: Comparison of four different antidots arrangements from Kemmler *et al.* [40]. Inset: IVC at $B = 0$ (right) and $B = B_1$ (left). (from Kemmler *et al.*, 2006, p.147003-2).

A direct imaging of the vortex distribution in a fivefold Penrose array of Co dots using a scanning Hall probe microscope had been carried out by Kramer *et al.* [39]. The experiment result was in strong agreement with the molecular dynamics simulation performed by Misko *et al.* at a field smaller than one vortex per cell [36, 37]. In the mean time, the vortices from ringlike structures at larger fields could stabilize a giant vortex state of two flux quanta at the center of the ring.

Random dilution of pinning

To answer the question of how to maximize the critical current with the smallest possible number of pinning sites, Reichhardt *et al.* studied superconductors with diluted pinning arrays by using numerical simulations [41], where the periodic pinning arrays were diluted by randomly removing a fraction of the pinning sites.

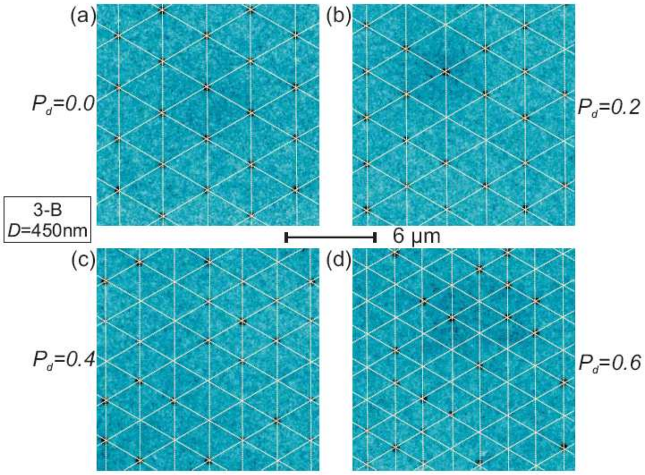

Figure 3.8: Scanning electron microscopy images of Nb thin films with randomly diluted antidot arrays in triangular lattices from Kemmler *et al.* [42]. The lattice constant $a(P_d) = 3.4 - 2.1\mu$m, for dilutions $P_d = 0 - 0.6$, are scaled to maintain a constant antidot density $n_p = 0.1\ \mu\text{m}^{-2}$. D is the diameter of the antidots. (from Kemmler *et al.*, 2009, p.184509-2).

Because the vortices remained correlated even after the pinning array had been diluted (up to 90% dilution rate had been confirmed), pronounced commensurability effects appeared at the same magnetic field strength as in undiluted pinning arrays. Moreover, the authors discovered that the commensuration could occur at fields significantly higher than the matching field (H_1) of an undiluted array. In the case where 90% of the pinning sites being removed, the matching field for a diluted array $H_1^\star = 10H_1$.

This theory was experimentally confirmed by Kemmler *et al.* [42], where periodic arrays of antidots in Nb thin films were investigated with transport measurements (Fig. 3.8).

Vortex dynamics in periodic pinning arrays

The hysteretic dynamics of vortices in periodic arrays of antidots were recently reported by Gutierrez *et al.* [43], where an artificial periodic array of antidots had been investigated with transport measurements. Sudden jumps on the IVCs were observed, which indicated different phases of the vortex dynamics during the measurements (Fig. 3.9).

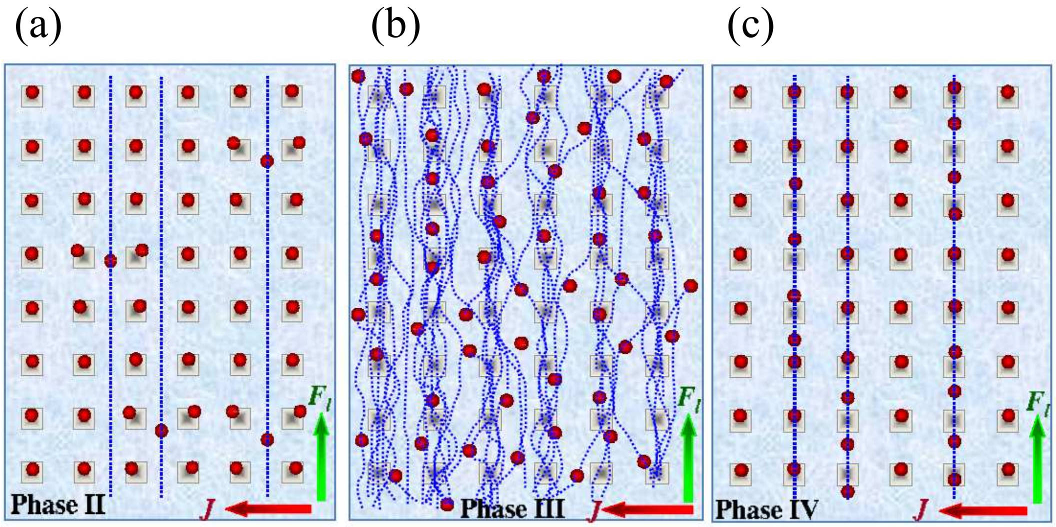

Figure 3.9: Sketches of the vortex motion from Gutierrez *et al.* [43]. (a) the interstitial vortex motion, (b) the turbulent-like 2D motion and (c) the 1D incommensurate row motion. (from Gutierrez *et al.*, 2009, p.140514-2)

When temperatures were near the transition temperature T_c and the magnetic fields were close to the first matching field, dynamic hysteresis effects on the IVCs could be detected (Fig. 3.10). Only interstitial vortices were moving while ramping up the driving force across the II-III boundary, whereas a disordered flow involving all vortices was presented while ramping down the current across the III-II boundary, therefore leading to a higher dissipation.

As reported in previous theoretical work, the transition to turbulent flow related to the interplay between interstitial vortices and those pinned in the antidots [36, 44, 45]. By using molecular dynamics simulations, Reichhardt *et al.* predicted that strong

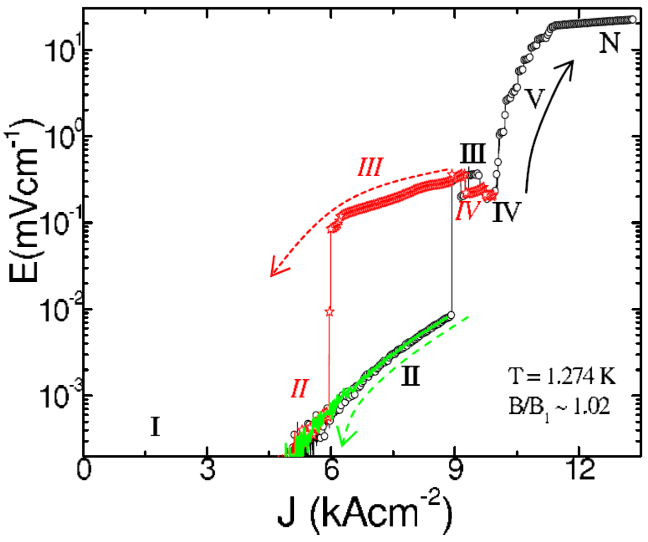

Figure 3.10: $E - J$ curves ramping up and down the driving current from Gutierrez *et al.* [43]. $T = 1.274$ K, $B/B_1 = 1.01$. An irreversibility is presented, and phases are labeled in italics for the ramping down case. (from Gutierrez *et al.*, 2009, p.140514-3)

voltage fluctuations on this phase were caused by the disordered motion of vortices [46].

3.3 Summary of previous work on weak-pinning channels

Vortices flowing through nanofabricated easy flow channels in superconducting films provide a useful system for studying the dynamics of interacting particles moving in tailored confining potentials. The fabrication of weak-pinning channels for guiding vortices through superconducting films at the nanoscale was well established [47, 48]. In the paper by Drift *et al.*, the film consisted of a $\sim$ 500 nm amorphous NbGe and a $\sim$ 50nm polycrystalline NbN on the top. The authors sputtered the double layer structure in a two step process without breaking the vacuum. In order to achieve $\sim$ 100nm channel width, the fabrication involved the electron-beam lithography and reactive dry etching.

Such channels have been employed in a variety of investigations of vortex dynamics with relatively large magnetic fields, typically greater than 10^3 Oe, including experiments on commensurability [48, 49], mode locking [50] and melting in confined geometries [51].

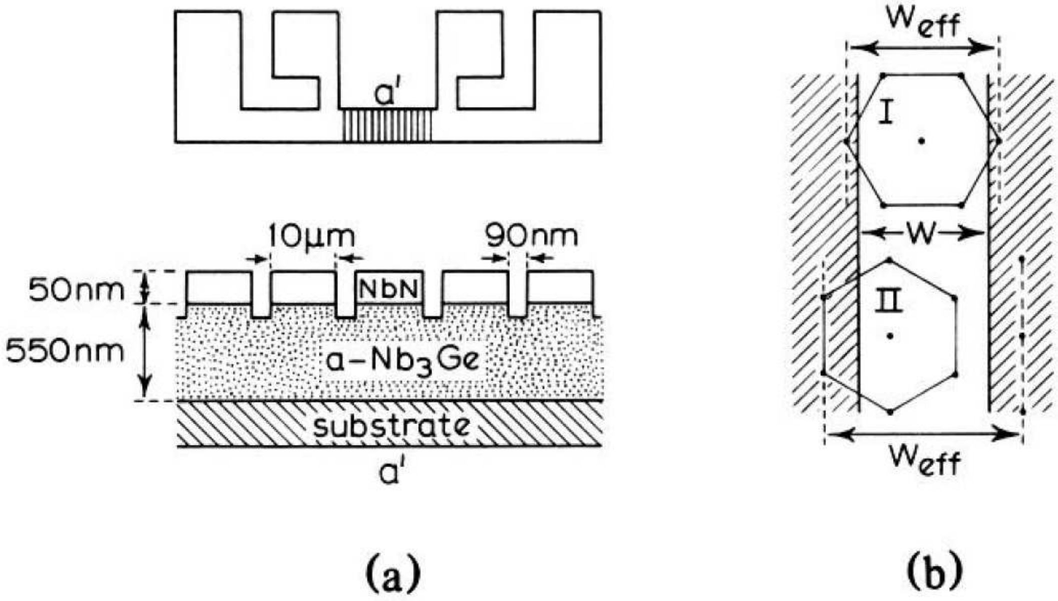

Figure 3.11: Schematic of a vortex lattice in a superconducting channel from Pruymboom *et al.* [48]. (a) the channel structure of a superconducting bi-layer and (b) two different orientations of the FLL for W_{eff}. (from Pruymboom *et al.*, 1988, p.1430)

Pruymboom *et al.* [48] studied a 2D flux-line lattice (FLL) flowing in the weak-pinning channels. With the four-probe technique, the shear strength and the hysteresis effects on the pinning force were directly probed. Fig. 3.11(a) is a schematic of the four-probe configuration and a side view of the channels. Figure 3.11(b) shows the effect width W_{eff} for two different FLL orientations. The flux line shear was described by a continuum approximation,

$$F_p = 2Ac_{66}/W, \tag{3.1}$$

where A is a constant, shear modulus c_{66} can be written as [52]

$$c_{66} = \frac{B_{c2}^2}{8\mu_0\kappa_1^2}\frac{\kappa}{\kappa_2}^2 b(1-0.29b)(1-b)^2, \tag{3.2}$$

κ, $\kappa_1(T)$ and $\kappa_2(T)$ are the Ginzburg-Landau and Maki parameters, the latter being used for the dirty limit.

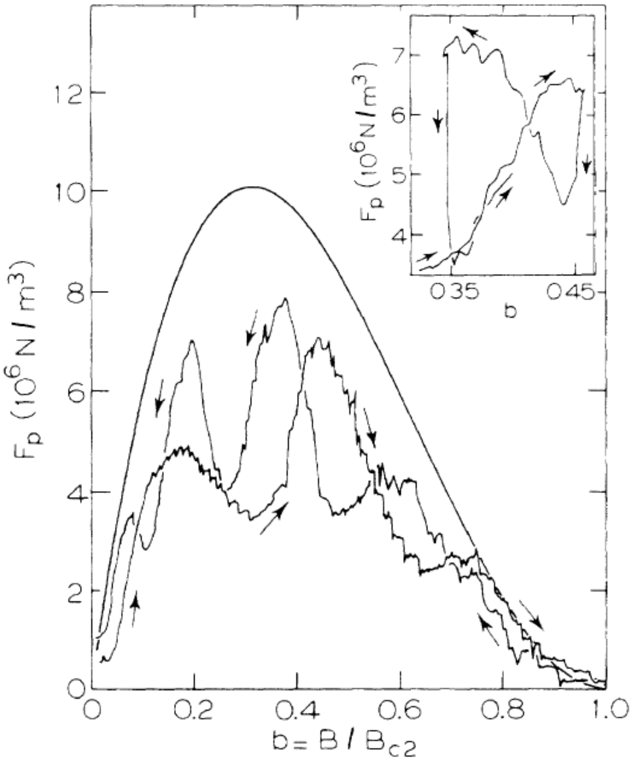

Figure 3.12: Recording traces of F_p vs. $b = B/B_{c2}$ from Pruymboom *et al.* [48]. Measured at 1.74 K ($\simeq 0.6\ T_c$) from the dynamic measurements. The continuum model is in a solid line. (from Pruymboom *et al.*, 1988, p.1430)

As one can see from Figure 3.12, the measurement data lay well between the F_p values. The hysteresis effects were caused by the nucleation and denucleation of the flux lines at the NbN edges. The inset in Figure 3.12 indicates the transfer from nucleation to denucleation could take place in a very small field interval, which was consistent with earlier predictions by Walton *et al.* [53].

A dc-rf interference technique was developed by Kokubo *et al.* [50] for a mode locking measurement of vortex lattice configurations, where an rf force with frequency f was applied through an rf transformer with balanced transmission lines and a matching circuit. A microscopically periodic velocity modulation was induced at the

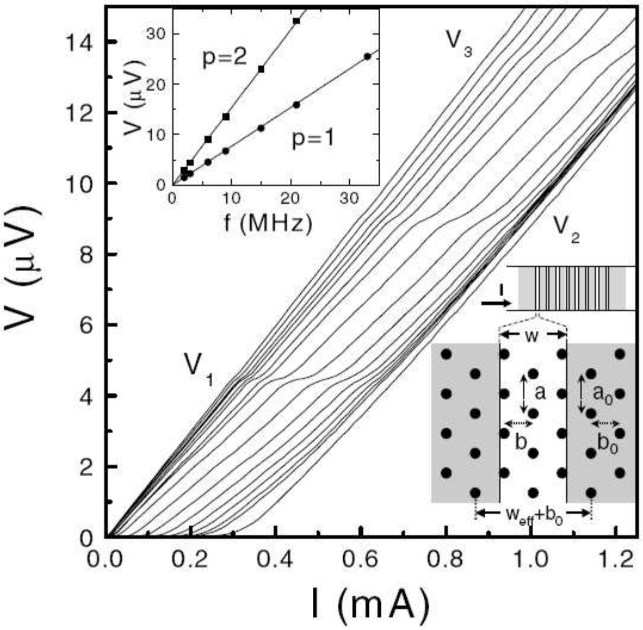

Figure 3.13: IV curves measured with a dc-rf interference technique from Kokubo *et al.* [50]. dc-IV curves measured with superimposed 6 MHz rf currents (amplitude from 4.7 to 0 mA, from left to right). V_p is interference voltages, where p is a integer. Upper inset: $V_p(f)$ for $p = 1$ and 2. Lower inset: schematic of vortices and a single channel. (from Kokubo *et al.*, 2002, p.247004-1)

washboard frequency $f_{int} = v/a$ when a vortex lattice moved coherently at an average velocity v [54], where a is the lattice period in the direction of motion. When $f/f_{int} = p/q$, p and q are both integers, these modulations get mode locked. Consequently, interference plateaus appeared in the IV characteristics (Fig. 3.13).

Because J_c shows oscillations and was globally proportional to c_{66}, the authors discovered that phenomenologically, J_c followed Eq. 3.1, although it was very sensitive to positional disorder of the vortex arrays in the channel edges. As shown in Figure 3.14, the number of vortex rows is better displayed by plotting the ratio of V_1 over f as a function of the field when the vortex lattice is moving coherently. The average interference voltage per channel can be easily derived as [50]

$$\tilde{V}_{p,q} = \frac{p}{q}\Phi_0 f n, \tag{3.3}$$

where n is the number of rows. Since there were $\sim$ 200 channels measured in the experiment, Figure 3.14 indicates that the steps indeed correspond to the numbers of vortex rows moving in the channel.

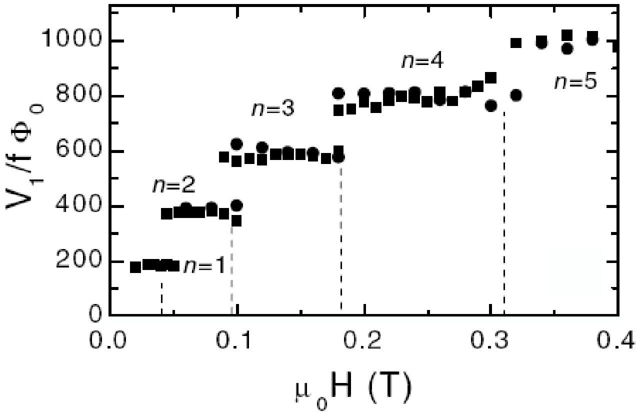

Figure 3.14: The number of vortex rows n, in a mode-locking measurement from Kokubo *et al.* [50]. V_1/f in units Φ_0 versus magnetic field $\mu_0 H$. Two rf frequencies were measured, $f = 6$ MHz (dot) and $f = 60$ MHz (square). (from Kokubo *et al.*, 2002, p.247004-3)

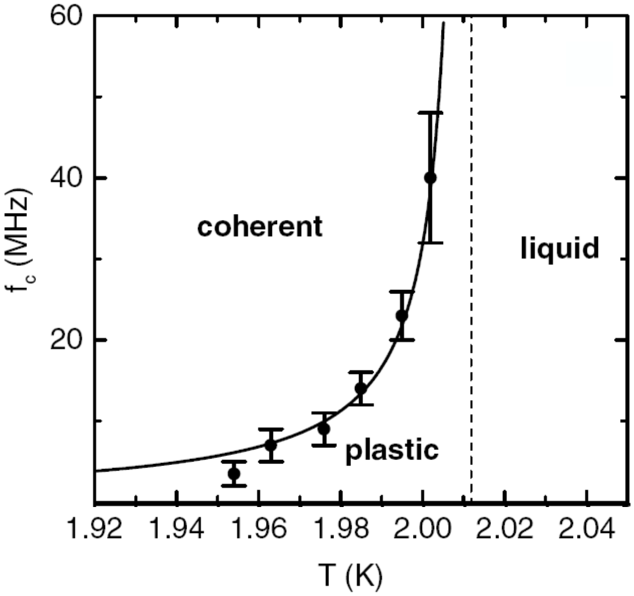

Figure 3.15: A phase diagram for a vortex melting from Besseling *et al.* [51]. Dynamic ordering frequency at $B = 1.16$ T as function of the temperature. Fitted with $f_c \sim (T_{m,e} - T)^{-1}$, where $T_{m,e} = 2.011$ K is indicated by the dashed line. (from Besseling *et al.*, 2003, p.177002-3)

The mode-locking technique can be used as a powerful tool for studying the dynamic melting of confined vortex matter moving in disordered, mesoscopic channels [51]. In the article by Besseling *et al.*, the authors discovered that the melting line was very sensitive to the mode-locking frequency, i.e., the average velocity. A phase diagram with a coherent, plastic, and fluid flow was presented, which characterized the divergence of the ordering velocity upon approaching the equilibrium melting line, as shown in Figure 3.15.

3.4 Conclusion

In this chapter, I have introduced various implementations of periodic pinning arrays as well as the corresponding theoretical work including arrays with nanoscale holes and magnetic dots in superconducting films acting as vortex traps. Periodic pinning experiments beyond the simple periodicities of the initial measurements have been presented as well. Later in the chapter, I reviewed the previous work on weak-pinning channels in the P.H. Kes' group at Leiden University. Here a relatively large field was applied to the channels, and the vortex lattice in the strong-pinning NbN channel edge played an important role in influencing the vortex distribution in the a-NbGe weak-pinning channels. The experiment results were presented, including the fabrication, the studies of commensurability, mode-locking and dynamic melting. In the next chapter, I will introduce the ratchet in general, then review previous work on vortex ratchets. The implementations and simulations of ratchet effects will be covered.

Chapter 4

Superconducting nanostructures with asymmetric pinning potentials: vortex ratchets

4.1 Introduction

The possibility of producing directed motion from a spatially asymmetric potential energy landscape in response to an external drive or non-equilibrium fluctuations with zero mean has inspired many investigations into a variety of ratchet systems [55–59]. Such ratchets could be used as pathways for producing a net transport of matter at the nanoscale. In addition, artificial ratchets can serve as model systems for understanding similar ratchet phenomena in biological systems while allowing for experimental control over many of the ratchet parameters [60–63]. Recent advances in nanofabrication make it feasible to investigate similar ratchets based on solid-state systems. Thus, ratchets allow for the exploration of the fundamental nature of particle transport at the nanoscale, both in solid-state devices and biomolecular systems.

With solid state ratchets, the nanofabricated nature of the devices makes it possible to control the various ratchet design parameters. The operating conditions can also be adjusted, such as the temperature, the waveform, the frequency of the driving force, and particle density so that one can move between regimes of independent and strongly interacting vortices. Thus, such fabricated ratchets can be used to study the rectification of vortex motions in asymmetrical potentials over a wide range of parameter space.

Over the past decade, implementations of ratchets in solid-state devices, including asymmetric structures of electrostatic gates above a two-dimensional electron gas [64], arrays of Josephson junctions with asymmetric critical currents [65], and microfluidics systems [66] were studied by groups around the world. Structures have also been developed for producing a ratchet effect with vortices in superconducting thin films involving either asymmetric arrangements of pinning centers [67, 68] or asymmetric magnetic pinning structures [69, 70].

In this chapter, I will introduce the ratchet in general and then focus on the implementations of the vortex ratchet in superconductors. More comprehensive discussions on ratchets can be found in the recent reviews by Reimann *et al.* [56] and Hanggi *et al.* [55].

4.1.1 Rocking ratchet

A generic ratchet consists of a system with an asymmetric potential energy surface. One such ratchet can be realized with a system in which the periodic potential has a broken parity symmetry [71]. The state of the ratchet can be described with a Langevin equation of the form

$$\eta \dot{x}(t) = f(x(t)) + \xi(t) + F(t), \tag{4.1}$$

where η is the the flux-flow vortex viscosity (Eq. 2.11), $f(x(t)) \equiv -\partial_x V(x)$, represents the potential, $\xi(t)$ is Gaussian noise with strength $2\eta k_B T$ and $F(t)$ is the driving force. A system consists of the tilt ratchet potential with a zero-mean drive, usually referred to as a 'rocking-ratchet' [56], where a spatial asymmetry is engineered into the potential energy $V(x)$ landscape governing particle motion; an external control variable can be adjusted to tilt this potential.

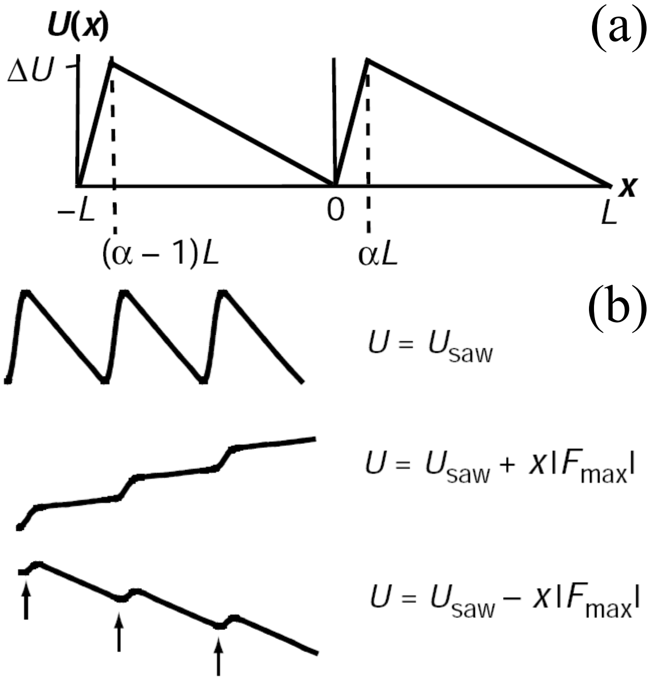

Figure 4.1: A schematic of sawtooth potential surface and the basic mechanism of rocking ratchet from Astumian [60] (a) A simplified potential surface for sawtooth structures. The well period is labelled by L. (b) The basic mechanism of a rocking ratchet with oscillatory driving force F_{max}. (from R. Dean Astumian, 1997, p.917)

Models of anisotropic periodic potential were given in Ref. [60]. The typical anisotropic periodic potential $U(x)$ is illustrated in Fig. 4.1. A rocking ratchet can be achieved by applying a fluctuating or oscillating force. As shown in Fig. 4.1(b), the potential energy decreases monotonically when it is tilted to the left, whereas remained minima in the potential will trap particles when it is tilted to the right. Thus, an alternative between $\pm F_{max}$ will cause a net flow of the particles towards the left. As noted in Astumian, a net flow cannot be generated in a rocking ratchet when the oscillation frequency reaches a limit; the particles cannot respond to the force quickly enough in order to move to the next well before the force reverses sign [60].

A system governed by the law of detailed balance does not produce rectification of thermal fluctuations at thermal equilibrium [26, 55, 60]. Both spatial asymmetry of the potential energy and nonequilibrium are required for a ratchet. An external force can break the thermal equilibrium of such a device and make it a nonequilibrium problem.

The promising applications in nanotechnology, as discussed in the beginning of this chapter, have generated much attention. The controlling of vortex motion in superconductors provides great possibilities for implementations of various vortex ratchets.

4.2 Survey of vortex ratchets

As discussed in Chapter 3, the motion of the magnetic flux trapped in the superconductors can limit the performance of the devices by ways of energy dissipation and internal noise [72]. Methods that are considered to overcome this issue include the pinning of vortices by artificial pinning sites and defects, as discussed in Chapter 3, in which submicron pinning holes/antidots and magnetic dots were nanofabricated in the superconducting films. With different configurations of pinning arrays, strong commensurabilities have been studied both theoretically and experimentally. But the ideal way to over come the issues caused by the presence of vortices would be to remove the vortices from the bulk of the superconductor. With the implementation of vortex ratchets in the superconductor, vortices can be guided in the desired direction as the oscillation force is applied to the system.

A rocking ratchet with 1-D asymmetric pinning potential was studied theoretically by Lee *et al.* [73]. The system consists of superconductors in which surface thickness varies periodically so that the pinning potential is primarily determined by the gradient of the ratchet potential $U(x)$ (Fig: 4.2). The potential energy gradient was largely caused by the variations in vortex line energy due to the thickness change

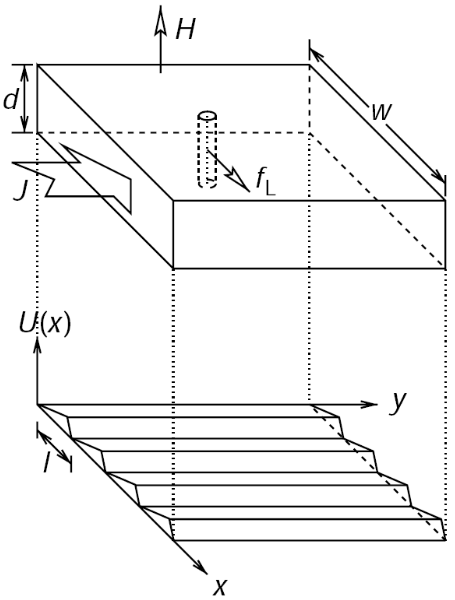

Figure 4.2: A diagram of a surface thickness ramp ratchet from Lee *et al.* [73]. An external magnetic field H is applied to the asymmetric potential ratchet ramp, Lorentz force is generated by applying J along the y direction moving the vortices with a net flow in the x direction. (from Lee *et al.*, 1999, p.337)

[74], where vortices had lower energy at thinner regions. The implementation of such structures in the experiments is difficult due to issues in fabrication.

4.2.1 Antidots

As discussed in Chapter 3, antidots (nanoscale pinning holes) can be used for controlling vortex motion in superconductors. With different shapes and configurations of the antidots, a vortex ratchet can be realized for the removal of unwanted trapped flux in devices. The net dc-voltage V_{dc} is expected to be antisymmetric when the external field H_a is inversed due to the Lorentz force changing sign with an inversed H_a while the spatial asymmetry remains the same.

An array of asymmetric pinning wells has been studied both numerically and analytically by Zhu *et al.* [75]. The asymmetric traps were constructed by arrays of two square antidots, where two different sized square holes were placed next to each other with a separation less than the lattice constant. This provided a sawtooth-type potential surface for the vortices. The net transport of the vortices was shown in the simulation results when a square wave ac-drive was applied to the system. The dependence of the ratchet rectification signal on other parameters, such as the driving amplitude, was studied in this article (Fig. 4.3), where we can see an optimum force amplitude ($F_L \sim 0.4$) and a optimum vortex density ($H = H_1$).

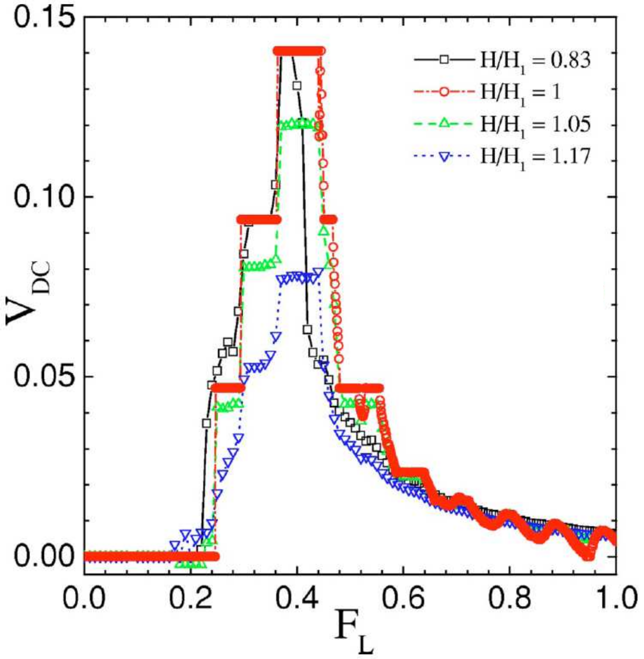

Figure 4.3: Molecular dynamics simulation results of the vortex ratchet V_{dc} response from Zhu *et al.* [75]. V_{dc} as a function of ac-driving amplitude F_L is shown with a different applied magnetic field. H_1 is the first matching field with approximately one vortex per pinning well. (from Zhu *et al.*, 2003, p.014514-6)

The ratchet effects induced by asymmetric antidots have been studied experimentally by Van de Vondel *et al.* [76]. Antidots with small and large square submicron holes were nanofabricated in an Al film. The net dc voltage was observed by applying an ac current in the film with the magnetic field applied perpendicular to the superconductor surface (Fig. 4.4) [76]. The high symmetry of the vortex configuration at the first matching field (H_1) cancels out the vortex-vortex interactions, which caused the largest voltage difference at fields just below H_1 [76]. Varying temperature did not show much difference in the inertia and the rectification features, although the experiment needed to be performed just below T_c in order to avoid the background pinning in the film from dominating the asymmetric antidot potential [26]. As discussed earlier in this chapter, the maximum V_{dc} did show a change in temperature, but the reasons were not fundamental to ratchet physics.

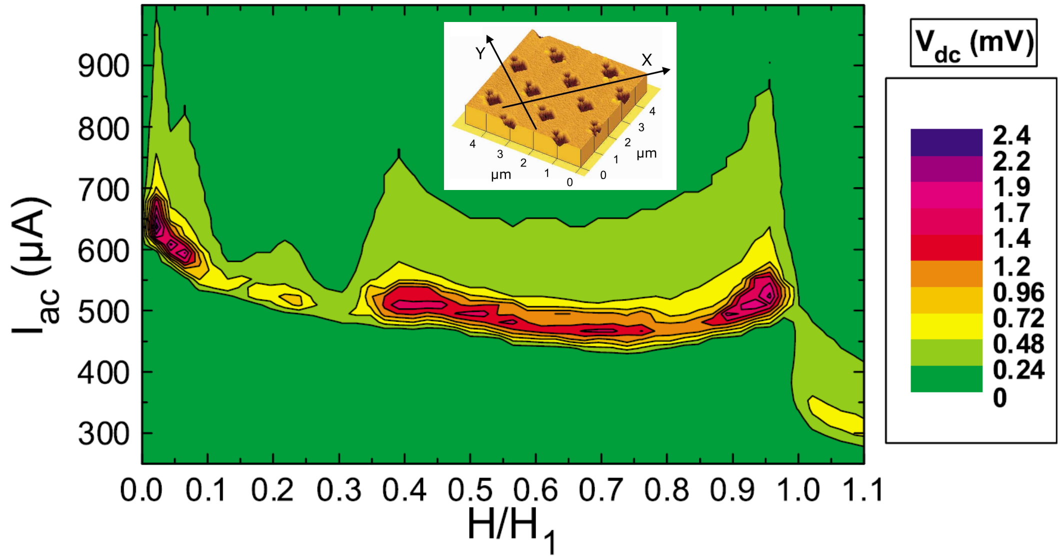

Figure 4.4: Contour plot of ratchet rectification measured at a field near or smaller than the first matching field from Van de Vondel *et al.* [76]. Net dc voltage response as a function of a normalized field H/H_1 and I_{ac}; Inset, an atomic force microscope image of the asymmetric antidots. (from Van de Vondel *et al.*, 2005, p.057003-1/2)

The authors had increased the rocking frequency from 1 kHz up to 10 kHz, and had seen no significant change in the V_{dc} response. This suggests that the experiment was carried out deeply in the adiabatic regime [56].

In fact, all of the vortex ratchets were measured deeply in the adiabatic regime. As discussed earlier, the ratchet rectification is expected to vary with frequency when the frequency reaches a characteristic limit. In general, this frequency limit can be characterized by three critical scales in the case of a rocking ratchet: the driving frequency applied to the ratchet, the thermal and noise activation rate of the vortices, and the ratio of the vortex velocity to the ratchet spatial period. In the recent experiments, with the experimentally attainable frequencies applied to the ratchets, no results show any ratchet variation. Evidences of ratchet signal variations with the temperature were found in other experiments, such as in the study of de Souza Silva *et al.* [77]. The changes in the ratchet signal were mostly due to the changes of the superconductor parameters with varying temperatures, but not caused by the thermal activation expected for a general Brownian motor [78]. Thus, the thermal and noise fluctuations do not play a significant role either. The ratchet spatial period is usually in the scale of a few micrometers. And the vortex critical velocity, where a superconductor switches to the normal state, is in the range of hundreds of meters per second in thin film superconductors [17]. This indicates the maximum frequency that can be achieved is $\sim 10^8$ Hz, without considering the practical experimental limitations. Any frequency that is smaller than $\sim 10^8$ Hz will drive the vortex past at least one ratchet period.

A surprising hysteresis was experimentally observed in the measurements. The vortex effective mass should not play a role in this particular measurement regime since the vortex effective mass was small enough that an inertia would require the oscillation frequency to be above 10^{12} Hz [12, 76]. The inertial effect in the IVC [Fig. 4.5(Inset)] was indeed induced by the vortex deformation. Molecular dynamics simulations based on an underdamped ratchet model were applied to the measurement results, proving the behavior of the so-called inertia ratchets (Fig. 4.5). This hysteretic response of the vortices can be characterized by a delayed re-trapping force [Fig. 4.5(Inset)], which was due to the distortion of the vortex core by the antidot structure [76, 77].

A detailed description of the simulation was presented by de Souza Silva *et al.* [77], where the vortex ratchet effects due to the pinning potential induced by the asymmetric antidots were shown in a similar fashion. The interplay between the 1D motion of weakly pinned incommensurate vortex rows and the 2D motion of the

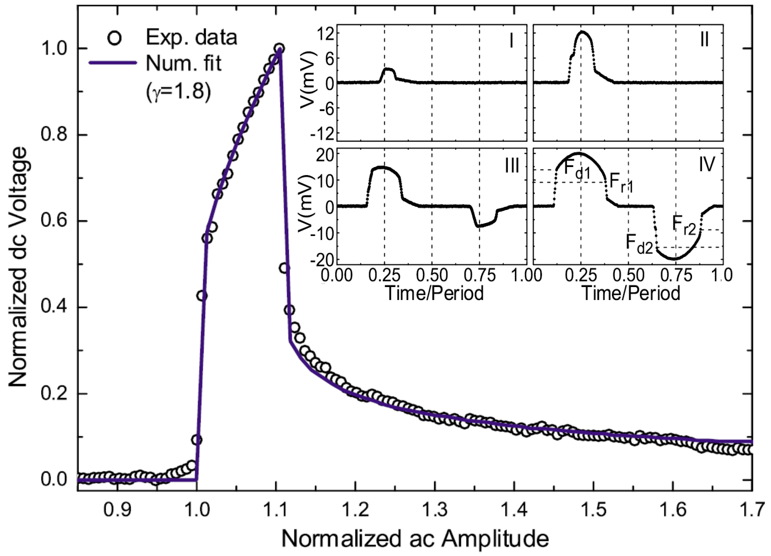

Figure 4.5: V_{dc} response of an inertia ratchet from Van de Vondel *et al.* [76]. Normalized dc voltage as a function of ac current amplitude, and the fitting line is the molecular dynamics simulation results. Samples were measured at $T/T_c = 0.973$ and $H/H_1 = 0.98$. (Inset) Simulation results of $v(t)$ with dashed lines show that the repinning force is smaller than the depinning force. I, II, III, IV are four regimes of vortex motion, explained in the text. (From Van de Vondel *et al.*, 2005, p.057003-3)

vortex lattice at the field just bellow the first matching field (H_1) presented two rectification peaks in the $V_{dc}(I_{ac})$ characteristics (Fig. 4.6), which was modelled by a molecular simulation. The four different regimes of vortex motion illustrated in the Figures (both Fig. 4.5 and Fig. 4.6) are: I) a fraction of vortices is moving in the easy direction; II) all vortices are moving in the easy direction; III) in addition to (II), a fraction of vortices are moving in the hard direction; IV) all vortices are moving in the easy and hard directions back and forth, resulting in the long tail observed in both the measurement and simulation results [77], which indicates a reduced effectiveness of the ratchet.

The temperature dependence of the ratchet signal was reported by de Souza Silva *et al.* (Fig. 4.7). An optimum temperature corresponding to the maximum of V_{dc} was observed at $T \simeq 0.982T_c$. V_{dc} decreased monotonically on both sides of this

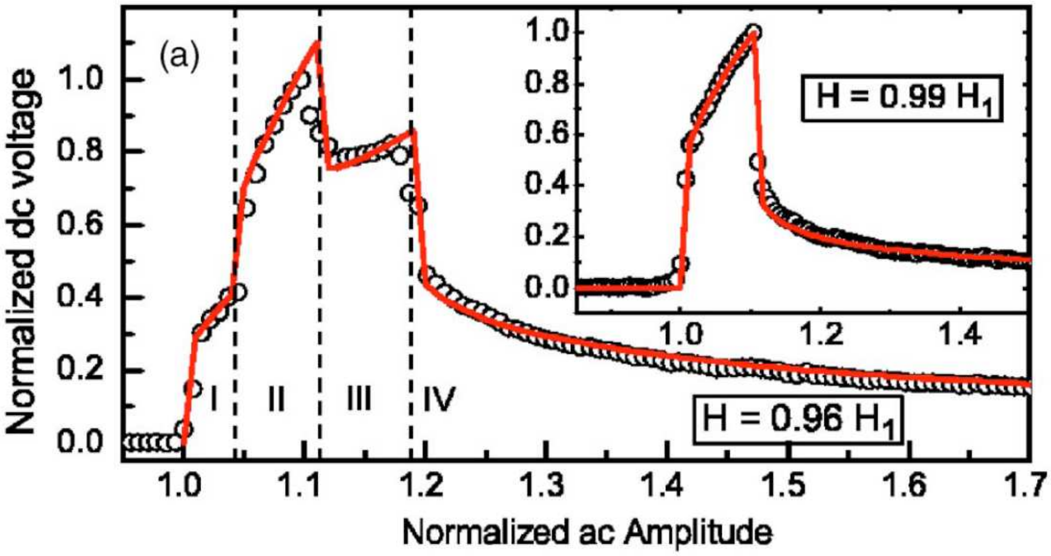

Figure 4.6: V_{dc} showing two rectification peaks at the field just below H_1 from de Souza Silva *et al.* [77]. Normalized dc voltage as a function of driving amplitude. I, II, III, IV are four regimes of vortex motion, explained in the text. (from de Souza Silva *et al.*, 2006, p.014507-7)

temperature. As discussed in Chapter 2, the vortex size largely increases with the temperature approaching the critical temperature. In this case, the vortex size was too big when compared to the size of antidots, and the vortices could not sense the detail of the antidots; thus, a decrease in the effectiveness of the asymmetric potential occurred. At a low temperature, the thermal and noise fluctuations were relatively small so that the vortices were more sensitive to the background pinnings in the Al film, which led to a reduction in the asymmetric rectification. Even though, we can see that the temperatures are all very close to T_c. In fact, all the antidots vortex ratchets are required to operate near Tc in order to avoid background pinning.

Vortex ratchets implemented with submicron antidots were also studied in $YBa_2Cu_3O_7$ thin films with resistive Hall-type measurements by Wordenweber *et al.* [79], and with scanning Hall probe microscopy by Crisan *et al.* [80].

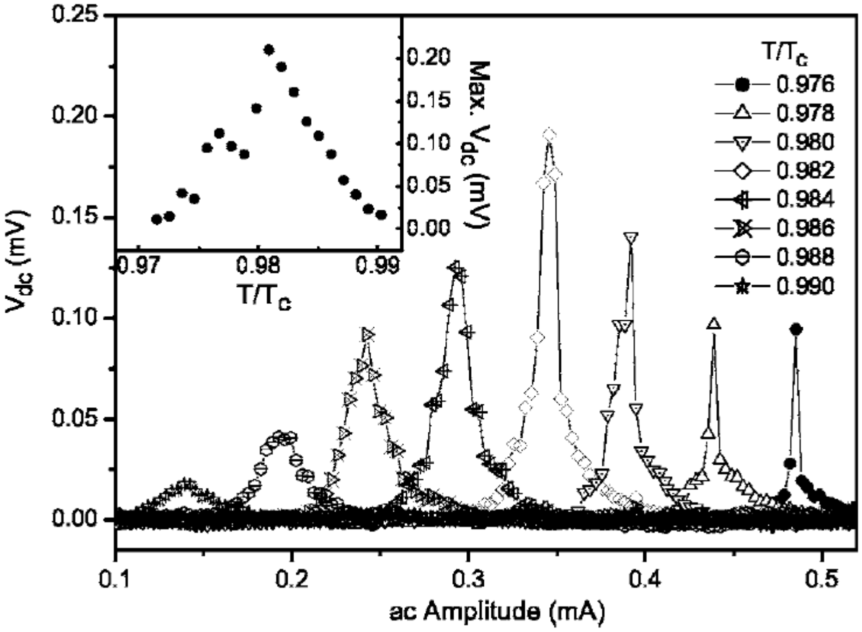

Figure 4.7: Temperature dependence measurements in a vortex ratchet with antidots arrays from de Souza Silva *et al.* [77]. V_{dc} versus driving amplitude for different temperatures as indicated in the figure. All measurement were performed at $H/H_1 = 0.95$ with driving frequency $f = 1$ kHz. Inset, the maximum V_{dc} *vs.* T/T_c. (from de Souza Silva *et al.*, 2006, p.014507-3)

4.2.2 Asymmetry in pinning density

Motivated originally by an experiment carried out by Kwok *et al.* [81], Olson *et al.* proposed a geometry where a graduated density of antidots were periodically arranged in superconductors [82]. The pinned vortices created an asymmetric effective potential, and the rectification corresponded to the motion of the unpinned interstitial vortices. The numerical simulation shows that the system has a net transport of the vortices for $H/H_1 > 1$ (Fig. 4.8) [82].

Triangular arrays of boomerang shaped pinning sites in superconductors were studied numerically by Zhu *et al.* [83]. The simulation results shows a net transport voltage when an ac driving force is applied to the system. By arranging two sets of boomerang arrays pointing towards each other, the molecular dynamics simulation resulted a lensing effect, where the vortex density increases at its "focus" region [83].

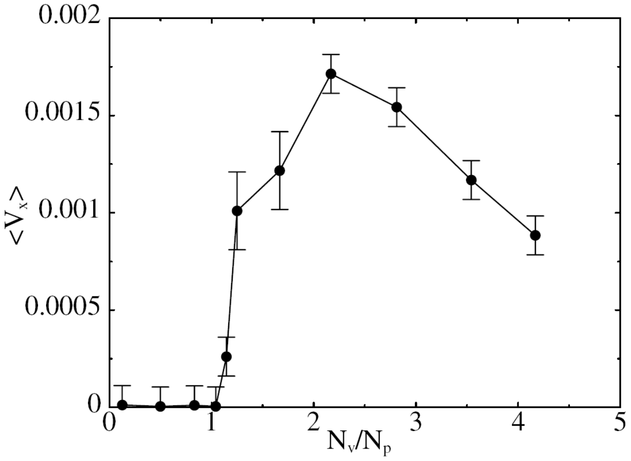

Figure 4.8: Simulation of the net dc voltage as a function of vortex density from Olson *et al.* [82]. The dependence of $< V_x >$ on the ratio of the votices to pins N_v/N_p shows the net motion of vortices only appears after the field exceeds the first matching field. N_v and N_p are the number of vortices and pinning sites. (from Olson *et al.*, 2001, p.177002-3)

Similar to the results presented in Olson *et al.* [82], Zhu *et al.* only observed a net transport of the vortices when $H/H_1 > 1$, and a maximum in dc velocity at $H/H_1 \approx 2$.

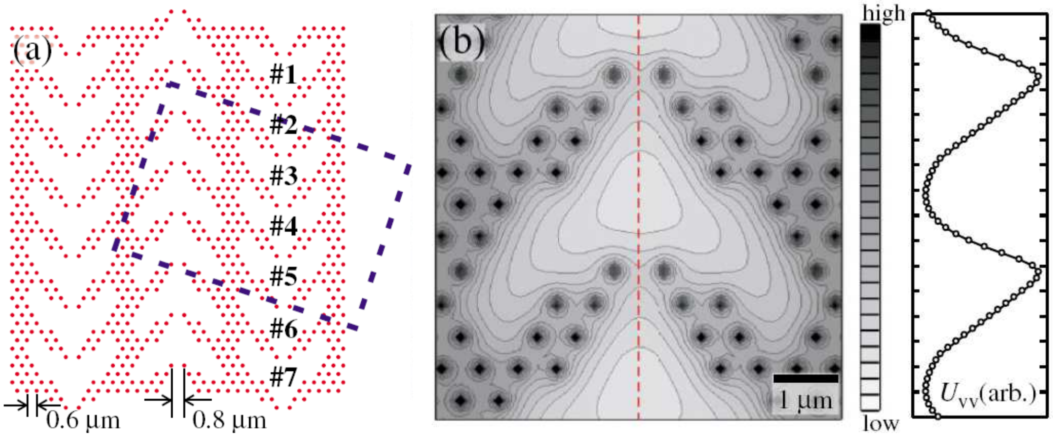

Figure 4.9: Schematic and calculated potential landscape of arrow-shaped pinning lattice from Togawa *et al.* [68]. (a) A schematic with dots represent the pinning site; (b) Calculated potential distribution with an energy landscape along the center line of the contour plot. (from Togawa *et al.*, 2005, p.087002-2)

The idea of boomerang shaped pinning arrays for guiding vortices in superconductors was experimentally implemented by Togawa *et al.* [68]. However, the boomerang shape is the pathway for interstitial vortices in this case (Fig. 4.9). The pinning sites were fabricated by focused gallium ion beam (FIB) irradiation on a Nb superconductor. The arrow-shape wedged cages were referred to as microscopic "funnels" for vortex motion [68], which was directly imaged by Lorentz microscopy [84] unlike most other experiments where transport measurements were performed instead. The vortices were driven by applying an oscillatory field to the Nb film (Fig. 4.9). The field was varied between 15 Oe and 30 Oe at a rate of $\sim 0.2\ Oe/s$. Both open-ended and closed-loop arrow-shape wedges were imaged by Togawa *et al.*. In the open-ended system, vortices were introduced in the 'racetrack' from a flux reservoir, and the number of vortices in the 'racetrack' is a variable. A cyclical motion of fixed-number vortices was demonstrated in the closed 'racetrack' [68].

4.2.3 Magnetic dots

Using magnetic dots in superconducting film as the pinning center and the nature of its pinning mechanism was discussed in Chapter 3. Within such systems, magnetic dots, normally Ni or Co, were nanofabricated either under or above the superconducting films [33, 85].

Square arrays of triangular shaped Ni dots with spatial asymmetry on top of superconducting Nb films were studied by Villegas *et al.* [69, 86]. The triangular dots have an in-plane aligned magnetization. The amplitude of the magnetic field applied in the experiment is always smaller than the magnetic field required to change the in-plane magnetization, which ensured that the magnetization remained invariable. As shown in Fig. 4.10, net dc voltage was observed when an ac-current was applied along the x-axis at the first matching field. The frequency dependence of the net dc voltage was also studied. Increasing the frequency to the highest attainable value (10 kHz) proved a pure adiabatic experiment [86].

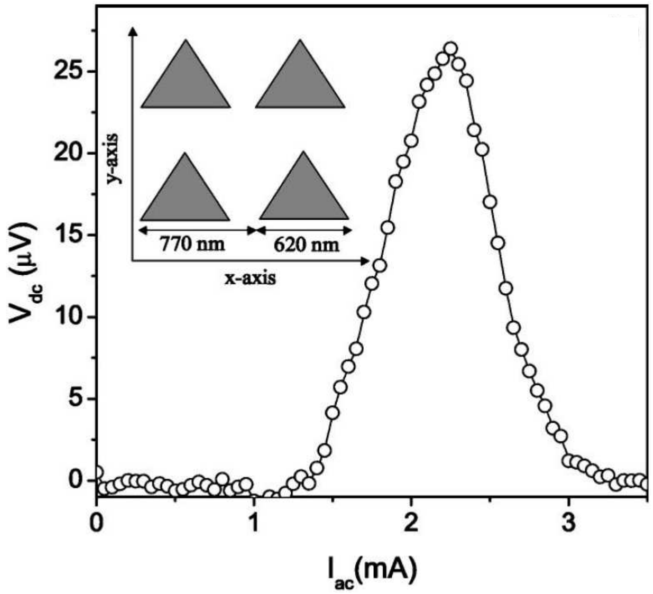

Figure 4.10: Measurement of V_{dc} as a function of the driving current from Villegas *et al.* [86]. V_{dc} vs. I_{ac} showing a maximum in net dc voltage response as a function of driving amplitude. Inset, a schematic of the square array of Ni dots. (from Villegas *et al.*, 2005, p.024519-2)

The interaction between vortices in a thin superconducting film and magnetic dipoles were investigated by Silhanek *et al.* [87] and de Souza Silva *et al.* [70], which were related to an earlier model proposed by Carneiro [88]. In the model by Carneiro, instead of using magnetic dots with permanent magnetization, one magnetic dot with nonpermanent magnetization was placed near a vortex and the interaction between both was simulated. With the possibility of rotating the dipole magnetic moment, the pinning potential generated by the magnetic dots can be tuned by applying an in-plane magnetic field, and the spatial asymmetry in the system is attributed primarily to the vortex-magnetic-dipole interaction [88].

In the experiment by de Souza Silva *et al.*, two types of periodic arrays of in-plane magnetized dipoles were fabricated, including a square array of magnetic bars and a close-packed square array of equilateral triangular Co rings. A nonsuperconducting layer was included between the superconducting and the micromagnet arrays to minimize proximity effect [70]. Unlike other vortex ratchet described earlier, where

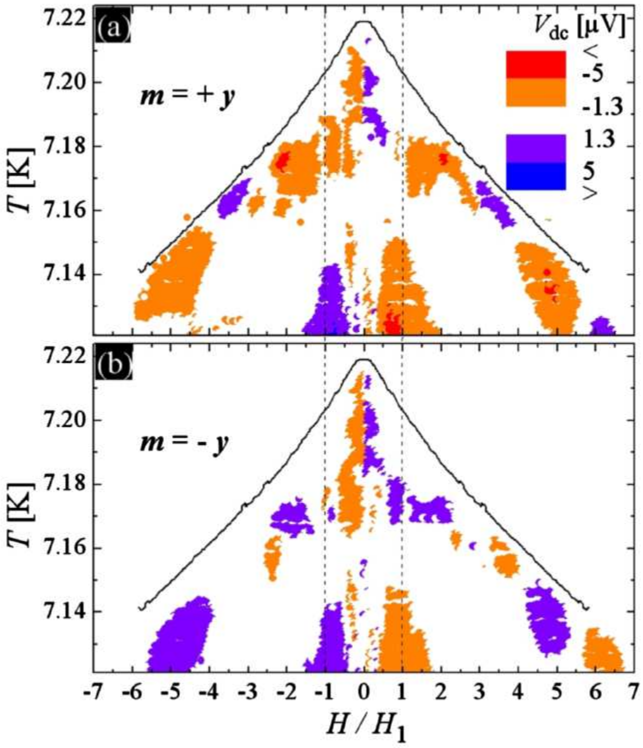

Figure 4.11: Net dc voltage response as a function of H and T for sample with triangular Co ringlike magnetic dipoles from de Souza Silva *et al.* [70]. V_{dc} response in the $T - H$ plane for two different magnetic dipole orientations, $m = +y$ (a) and $m = -y$ (b). (from de Souza Silva *et al.*, 2007, p.117005-2)

antisymmetric dependence of V_{dc} is expected when the external field H_a is inversed, a symmetric response of V_{dc} was observed as the H_a (H in this article) was reversed, but only for $|H_a| > H_1$ (Fig. 4.11) [70]. This symmetric dependence of V_{dc} on H_a was caused by the cancellation between the inversed H_a and the corresponding reversal of the asymmetric potential, which was a non-variable in the case of spatial asymmetric potential as discussed in other ratchet implementations. As shown in Fig. 4.11, the antisymmetric dependence of V_{dc} at a field near or smaller than H_1 was observed for both magnetic orientations ($m = \pm y$), suggesting that asymmetric pinning potential in this field region was dominated by a nonmagnetic ratchet potential as those generated for instance by small asymmetries of the triangles due to fabrication issues

[70].

4.2.4 Ratchet reversal

The ability to reverse particle drift directions in a ratchet system was studied in Ref. [56] and [55]. A simulation particularly for a rocking ratchet by Bartussek *et al.* resulted reversal effects [78]. The theoretical study of overdamped Brownian particle interactions carried out by Derényi and Vicsek shows a reversal of the ratchet rectification direction as particle density was increased [89]. The topic of separating two interacting species of small particles has been studied both analytically and numerically by Savel'ev *et al.* [90–94], which can be a potential application of the ratchet reversal effects.

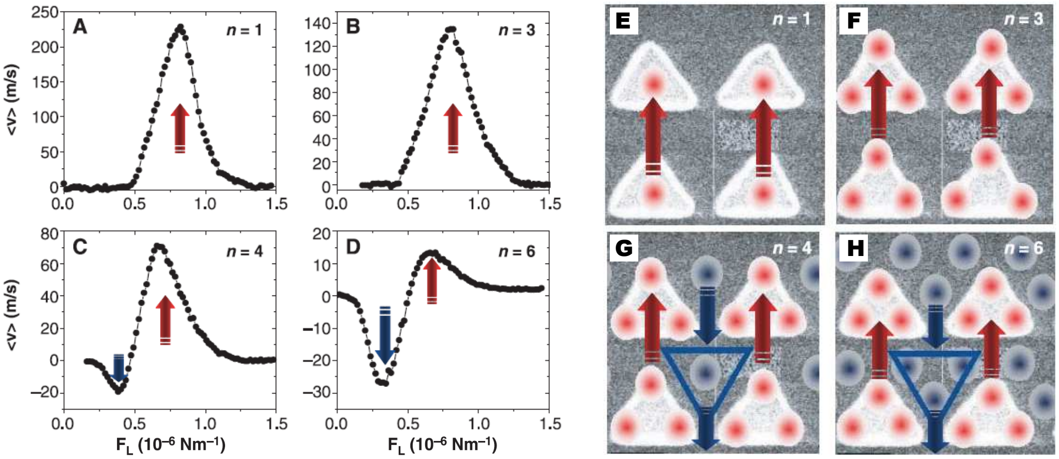

Figure 4.12: Vortex reversals variation with the vortex density and the driving amplitude from Villegas *et al.* [95]. (A to D) Net velocity as function of Lorentz force amplitude for four different vortex densities as indicated by n; (E to H) Schematics of vortex distribution at corresponding vortex density. The red arrows indicate the vortices hopping between triangles, therefore showing the original ratchet direction, whereas the blue arrows indicate the motion of interstitial vortices, therefore showing the reversal ratchet direction. (from Villegas *et al.*, 2003, p.1190)

The vortex ratchet with arrays of triangular magnetic dots fabricated in a Nb superconducting film was studied by Villegas *et al.* [86, 95] as described earlier. In addition to the vortex ratchet that drives vortices in the original direction at relatively small fields, the ratchet reversals were observed at $H > 3H_1$ for a small driving amplitude (Fig. 4.12) [95]. The vortices were expected to be pinned in the magnetic triangles at $H \leq 3H_1$, so that the vortices underwent movement in the original ratchet direction by hopping between the triangular pinning sites. Increasing the field further, subsequent vortices appeared in the interstitial locations between the magnetic triangles, where they experienced the asymmetry potential that was induced by vortices pinned in the magnetic islands. This secondary potential is reversed compared to the original one. Thus, a reversal dc signal appeared at the low drives when the more weakly pinned interstitial vortices moved, and the ratchet recovered its original direction for large drives, where the vortices were depinned from the magnetic islands that were moving in the original direction [95]. The process is summarized in Fig. 4.12.

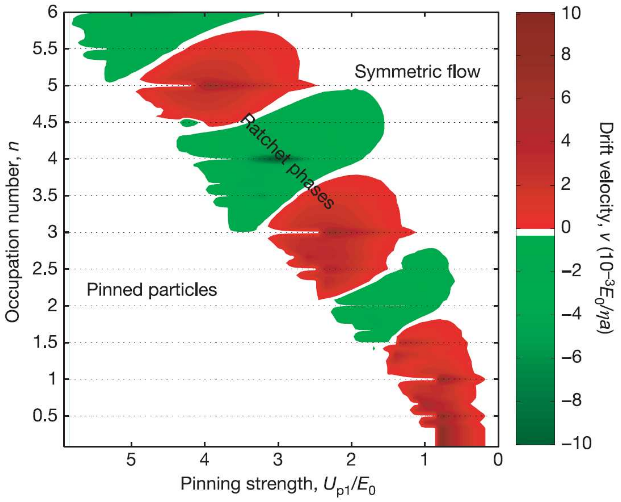

Figure 4.13: Multiple ratchet reversals simulated as a function of temperature and field from de Souza Silva *et al.* [96]. Simulation results showing multiple ratchet sign inversions. The green and red areas correspond to positive and negative V_{dc} respectively. The white region represents $V_{dc} = 0$. (from de Souza Silva *et al.*, 2006, p.652)

Based on the configuration of antidots studied by Van de Vondel *et al.* [67] and de Souza Silva *et al.* [77], de Souza Silva *et al.* [96] investigated the ratchet reversals in such system. Unlike previous experiments, where the vortex ratchet were observed at fields small or less than the first matching field, ratchet reversals, on the other hand, were observed alternating with conventional ratchet at fields near and larger than $2H_1$ (Fig. 4.13). This differs from the study on ratchet reversals reported by Villegas *et al.* [95], where the reversal was due to the effect of interstitial vortices moving in an inverted ratchet potential; the ratchet reversals in this case were caused by subsequent vortices trapped in the large and small holes alternatively with the field progressively increasing after the first matching field [95].

Based on the same geometry, a thickness-modulated surface ramp ratchet proposed by Lee *et al.* [73] showed the reversal effects in the vortex ratchet that were observed at higher vortex densities by Lu *et al.* via numerical simulations [97]. The ratchet reversals were explained by a 2D description of the vortex configuration as a function of vortex density despite the 1D ratchet geometry. The depinning force was observed to be lower in the hard direction at the intermediate vortex density, which resulted in the ratchet reversals due to the weak intervortex interactions. Another reversal appeared in the simulation results with a further increase in the vortex density. The mechanism of the sign reversal was explained by the different phase of the vortex lattice. A conventional ratchet response was expected when the vortex configuration was highly ordered, whereas a ratchet reversal was observed when the vortices formed a smectic or a disordered phase where the intervortex interactions were no longer negligible [97].

When Related to the simulation by Lu *et al.*, ratchet reversals due to the strong intervortex interactions and the vortex positional disordering were studied by Gillijns *et al.* experimentally [98]. In this experiment, an array of Co/Pt magnetic dots fabricated in superconducting Al film was investigated with standard transport measurements. The authors proved that the vortex reversal was determined by both the intervortex interaction and more importantly by the effective interaction distance, which was characterized by the penetration depth λ in the case of the vortex ratchet. Four samples with different asymmetric pinning potential periods d were studied. For

$\lambda < d$, the motion of the vortex was drifting toward the conventional ratchet direction. The ratchet sign reversal was detected when the effective interaction distance was longer than the ratchet potential period, $\lambda > d$.

4.3 Conclusion

The concept of the ratchet was introduced in the beginning of the chapter, followed by an introduction of generic rocking ratchets along with its basic characteristics. An survey of other approaches for the vortex ratchets using nanostructured superconductors were presented. Almost all of the vortex ratchets with artificial pinning sites were required to operate at temperatures very close to the superconductor transition temperature in order to avoid the background pinning from getting too large. Although the generic ratchets are expected to become less effective when the frequency is higher than a characteristic limit, the vortex ratchet measurements were performed almost always deeply in the adiabatic state, where the frequency is far bellow the limit so that the variation of the frequency does not play a significant role in influencing the effectiveness of the ratchet rectification. Our measurements of the vortex ratchet effects in the superconducting weak-pinning channels with periodic constrictions will be presented and discussed later in the thesis.

Chapter 5

Fabrication and measurement scheme

5.1 Sample fabrication

Nanofabricated weak-pinning channels were studied by a group at Leiden University for an extended period of time as we discussed in Chapter 3 [47].

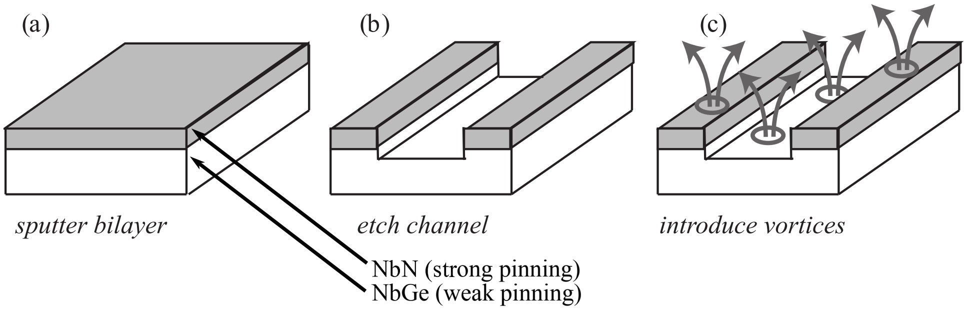
(a)
(b)
(c)
sputter bilayer
etch channel
introduce vortices
NbN (strong pinning)
NbGe (weak pinning)

Figure 5.1: Weak-pinning channel fabrication schematic on a bilayer superconducting film.

Such channels are fabricated from bilayer films of amorphous-NbGe, an extremely weak-pinning superconductor, and NbN, with relatively strong pinning [Fig. 5.1]. In the range we had measured, $T_c^{NbGe} \approx 2.90\ K$, $T_c^{NbN} \approx 10\ K$. A reactive ion etching process removes the NbN from regions as narrow as 100 nm, defined with electron-beam lithography, in order to produce weak-pinning channels through which vortices can move easily. In contrast, the vortices trapped in the NbN banks outside of the channels remain strongly pinned. The lack of pinning allows the vortices to move through the channels, with the dominant interaction determined by the shape of the lithographically-defined channel walls. In the various channel experiments discussed in Chapter 3, the interactions between the vortices in the NbN banks and those in the channels play a key role in the dynamics [99]. A typical sample with wire-bonding pads is shown in Fig. 5.2.

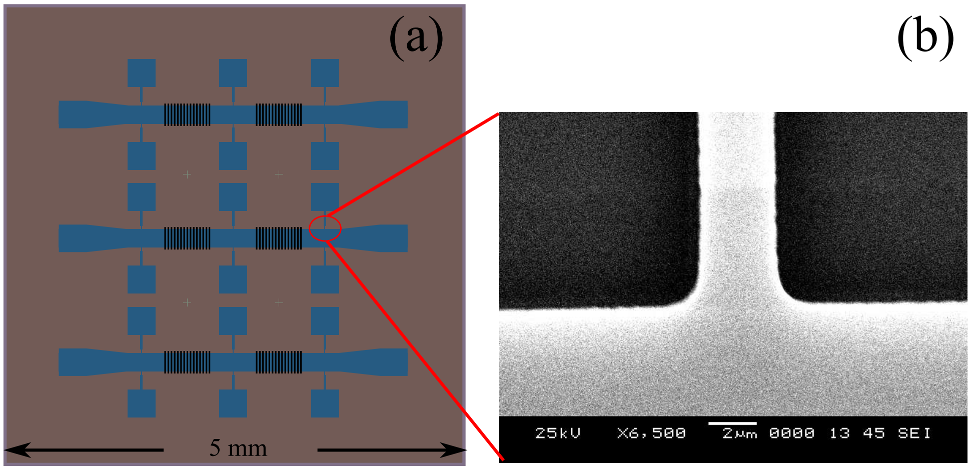

Figure 5.2: (a) A schematic showing 6 sets of weak pinning channels on the superconducting strips. The voltage leads connect the strips with wire-bonding pads symmetrically to both sides across the strip. The line width at the connections to the strips is ~ 5 μm-wide. (b) A zoom on the Scanning Electron Microscope(SEM) image of voltage leads where they connect to the strips.

The channels are arranged across a strip, with H_a oriented along the thin axis of the strip (Fig. 5.3). The strip pattern contains pairs of probes for coupling with a room-temperature low-noise amplifier used for sensing the voltage drop V along the strip due to the vortex motion through the channels. A transport current driven through the strip with an external supply generates a transverse Lorentz force on the vortices. Between each pair of voltage probes is an array of identical channels with inter-channel spacing s. We can tailor the confining potential for the vortices in the channels by controlling the shape of the channel walls. There are three categories of channels we measured: 1) uniform channels with a constant width; 2) ratchet channels with asymmetric sawtooth patterns; and 3) diamond channels with a periodic chain of cells defined by diamond-shaped constrictions. Normally, the period along the channel in the last two categories is defined with parameter p. The ratchet cell or diamond cell can also be characterized by the half-width with a parameter b.

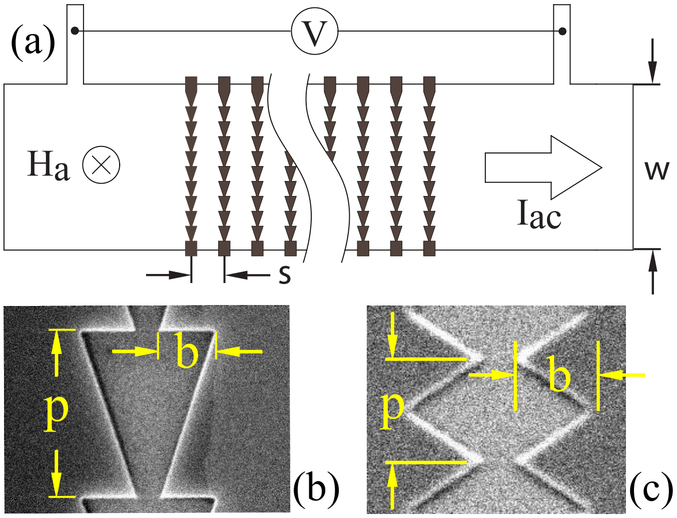

Figure 5.3: (a) Schematic of the strip with ratchet channels showing sample parameters; in this case, channel spacing $s = 10\ \mu m$ and strip width $w = 50\ \mu m$. (b) SEM image of a ratchet channel cell. (c) SEM image of a diamond channel cell.

5.2 Transport measurements

We generate H_a with a superconducting Helmholtz coil, and a μ-metal shield reduces the background magnetic field below 13 mG. For each measurement sequence, the strip was heated to at least $\sim$ 15 K, well above the T_c of both the NbGe and NbN films. The strip was then cooled in $H_a = 0$, while we subsequently increased H_a to the measurement temperature. All of our measurements were performed with the strip immersed in a pumped helium bath with a temperature stability of $\sim$ 0.2 mK/hr.

As discussed in Chapter 2, if vortices are present in a type-II superconductor in the absence of any bulk pinning or entry barriers, an applied current drives vortices causing dissipation [6]. Usually the voltage has a linear dependence over the current at this flux flow regime. If the current is continuing to be increased, the voltage dependence can deviate from a linear flux flow slope so that voltage can increase more quickly. This curvature in the IV curve will quickly reach an instability with an increase of the current, due to the increasing dissipation. This instability switches the sample out to the normal resistance state, causing the sample to become non-superconducting [14].

This critical current characterizes the transition from a static state to the dynamic flux flow regime. The transition can be defined by measuring the critical current I_c in the conventional way. This can be done by monitoring the current-voltage characteristics (IVC), which are proportional to the vortex velocity and density, then applying a $1\,\mu$V criterion. The room temperature pre-amplifier - Stanford SR560 has a noise of $V_{noise} \sim 4\ nV/\sqrt{Hz}$. With the low-pass filter bandwidth we used, $\Delta f = 30\ kHz$, the RMS Voltage $V_{rms} = V_{noise}\sqrt{\Delta f} \approx 0.7\ \mu V$ [100]. This is the main reason we chose this criterion for measuring the critical current. $1\,\mu$V is large enough to exceed the general noise floor and at the same time is not too large, therefore, the critical current extracted characterizes the transition of vortex motion correctly.

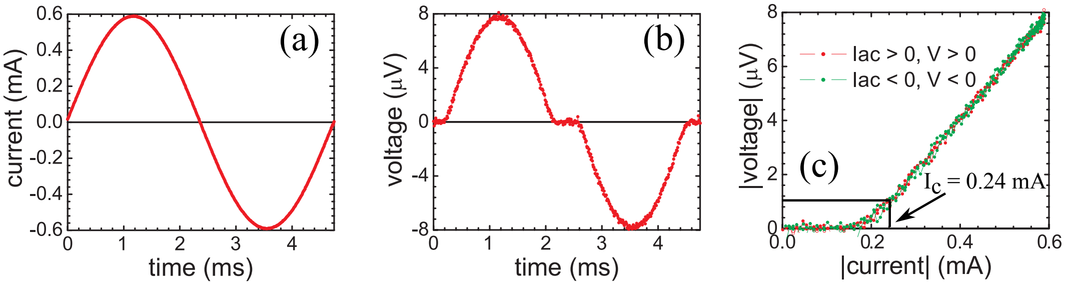

Figure 5.4: (a) A sinusoidal current drive $I(t)$. (b) $V(t)$ for 2 μm-wide uniform channels; $I_{ac} = 0.59$ mA. (c) IVC for 2 μm-wide uniform channels plotted with positive and negative branches in the first quadrant for comparison. We extract I_c with a $1\,\mu$V criterion.

We drive the vortices with 200 cycles of a bias current sinusoid at 210 Hz, then average the resulting voltage response in order to obtain a $V(t)$ curve for one period (Fig. 5.4). We can see that the noise level on the IVC at the static state is much smaller than 0.7 μV as we estimated above due to the averaging, which gives $\sim \sqrt{200} \simeq 14$ times a better signal to noise ratio.

We combine this resulting $V(t)$ curve with $I(t)$ to obtain IVC, where we apply the 1 μV criterion for extracting the critical current[Fig. 5.4(c)].

Chapter 6

Vortex dynamics in weak-pinning channels with periodic constrictions

6.1 Introduction

Vortices, confined to superconducting easy flow channels with periodic constrictions, exhibit reversible oscillations in the critical current when vortices begin moving as the external magnetic field is varied. This commensurability scales with the channel shape and arrangement, although screening effects play an important role. For large magnetic fields, some of the vortices become pinned outside of the channels, leading to magnetic hysteresis in the critical current. Some channel configurations also exhibit a dynamical hysteresis in the flux-flow regime near the matching fields.

In this chapter, I describe measurements of vortex dynamics in weak-pinning channels that contain periodic constrictions at small magnetic fields, generally less than 10 Oe. Thus, this involves considerably smaller fields than much of the previous work on vortex matter in unstructured weak-pinning channels [48, 50, 51]. The nature of the channels provides pathways for the easy flow of vortices, while the lattice of

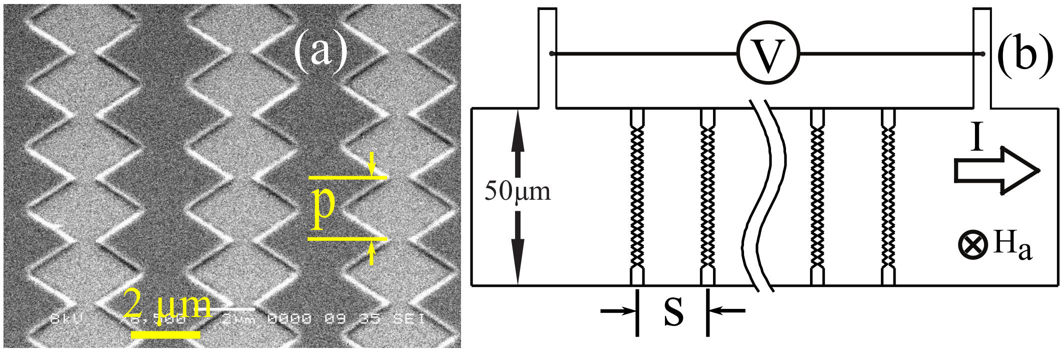

Figure 6.1: (a) Scanning electron micrograph of three channels with periodic diamond constrictions. (b) Strip layout, including channel and magnetic field orientation.

periodic constrictions results in strong matching effects with substantial enhancement of the critical current I_c at certain values of the external magnetic field H_a. Although we do not image our vortex distributions directly, we can determine that over much of the field-range of our measurements, all of the vortices are confined to the channels, with the dynamics determined solely by the channel geometry, screening currents in the film, and the interactions between vortices. Thus, in this field regime, there is no distinction between pinned and interstitial vortices. At larger magnetic fields H_a, the vortices can enter the regions outside of the channels where they become strongly pinned and do not participate in the flux-flow. Rather, these pinned vortices alter the potential for the vortices that are confined to the channels and lead to an irreversibility of $I_c(H_a)$.

6.2 Channel configuration

We fabricated our channels as described in Chapter 5.1. The channels are arranged across a 50 μm-wide strip, with H_a oriented along the thin axis of the strip (Fig. 6.1). Each channel contains a periodic chain of cells defined by diamond-shaped constrictions, all of which are 3.2 μm across at the widest point and 700 nm wide at the constriction, with a period along the channel p. We measured sets of such channels with five different combinations of (s, p) (Table 6.1).

sample label	period(μm)	spacing(μm)
d1	0.5	20
d2	1	20
d3	2	5
d4	2	20
d5	2	50

Table 6.1: Diamond constriction samples with five different combinations of (s, p).

We perform our measurements with the strip immersed in a pumped helium bath. Our results presented here were obtained at a temperature T between 2.61 K and 2.90 K (89% – 99% of T_c^{NbGe}). We can apply the standard dirty-limit expressions (Eq. 2.7 – 2.8) in order to estimate the relevant superconducting parameters of the a-NbGe and NbN films.

For the a-NbGe, the coherence length ξ varies between $20 - 80$ nm over the range of T; thus, the vortex core size is always much less than the smallest dimension of the channels, and the vortex cores are essentially point-like. On the other hand, the penetration depth is relatively large, and the thin-film screening length, $\lambda_\perp = 2\lambda^2/d$, where d is the film thickness, which ranges between $40 - 370\,\mu$m for the a-NbGe.

In the NbN that forms the banks between the channels, $\lambda_\perp^{\mathrm{NbN}} \approx 8\,\mu$m, there is little temperature variation since $T/T_c^{\mathrm{NbN}} \ll 1$ [101].

Thus, the circulating currents for a vortex in a NbGe channel extend along many, if not all, of the diamond cells in that particular channel and penetrate roughly $8\,\mu$m into the NbN banks on either side of the channel. Because $\lambda_\perp^{\mathrm{NbGe}}$ is much greater than both $\lambda_\perp^{\mathrm{NbN}}$ and the width of the channels, vortices will be confined to the channels. The shape of the channel walls will thus play an important role in distorting the circulating currents around each vortex.

6.3 Edge barrier effects on critical currents

As described in Chapter 5, we measured I_c, where the vortices move from a static configuration to a dynamical sliding state by applying a 1 μV criterion to IVCs.

Measurements of the field dependence $I_c(H_a)$ yield information about the vortex dynamics in the channels. For purposes of comparison, we fabricated a set of 0.5 μm-wide uniform channels such that there were no constrictions, and we measured $I_c(H_a)$ (Fig. 6.2). The response is similar to that of the characteristics of an edge barrier for a thin, weak-pinning superconducting strip in a perpendicular magnetic field, where the entry of vortices at the strip edge is determined by the distortion of the current density across the width of the strip [102, 103].

For a standard edge barrier, $I_c(H_a)$ follows two different regimes: for H_a near zero, I_c decreases linearly with H_a, when vortices enter the strip at one edge and are immediately swept across the entire strip width; and for a larger H_a, $I_c \propto H_a^{-1}$, where the external magnetic field is large enough to push vortices into the strip, even for transport current less than I_c.

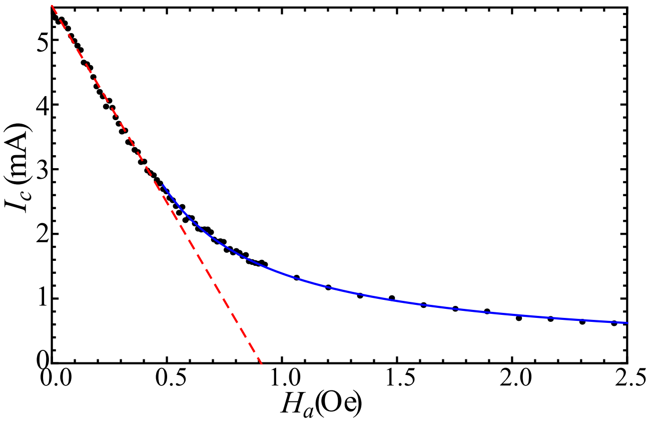

Figure 6.2: $I_c(H_a)$ for uniform-width channels at low magnetic fields along with linear fit (dashed) and H_a^{-1} fit (solid), described with the edge barrier model. H_s is the field limit for the vortex entry into the superconductor at $I = 0$

For a superconducting strip geometry in a perpendicular field, B will be somewhat smaller than H_a due to screening effects until $H_a \gg H_s$ (Fig. 6.3), where H_s is the surface entry field [104]. Note that the average flux density $\bar{B}$ is constant for $H_{ex} < H_a < H_{en}$, because the geometrical barrier prevents vortices from entering or leaving the sample.

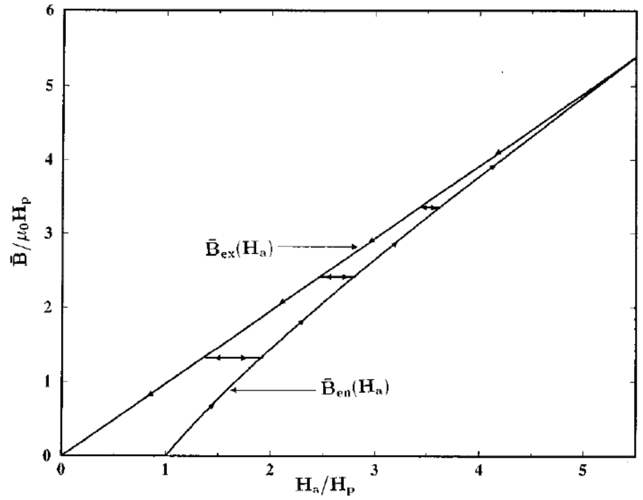

Figure 6.3: The edge barrier effect on the average flux density $\bar{B}$ as a function of the applied field H_a from Benkraouda and Clem [104]. $\bar{B}_{en}$ and $\bar{B}_{ex}$ are the critical entry and exit condition respectively, and $H_{ex} < H_a < H_{en}$ is the constant-flux condition. (from Benkraouda and Clem, 1996, p. 5721).

In order to understand the edge barrier with more detail, let us consider a thin superconductor strip with thickness d and width W in the limit of $d \ll W$ and $d \ll \lambda$. As shown in Figure 6.4, a perpendicular magnetic field H_a is applied along the thin axis, and a transport current I is driven along the long axis of the strip. Vortices can be introduced into the superconducting thin film when the current density at the edge of the strip approaches the Ginzburg-Landau depairing current density j_{GL}:

$$j_{GL} = \Phi_0 / 3\sqrt{3}\pi\mu_0\xi\lambda^2, \tag{6.1}$$

where Φ_0 is the flux quantum, $\Phi_0 = h/2e$. This condition corresponds to an instability, where vortices start to nucleate at the edges of the strip, such that any increase in the current density at the edge of the superconductor will cause vortices to flow into the strip.

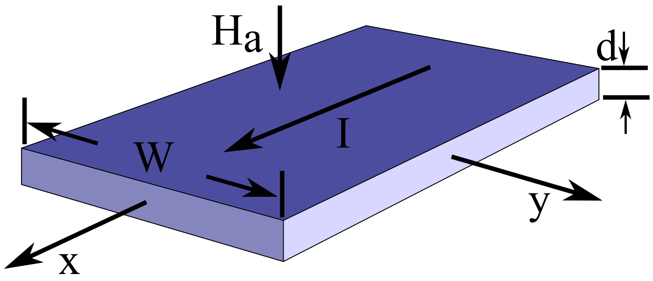

Figure 6.4: A schematic showing a magnetic field applied to a superconductor strip along the thin axis, and a transport current applied along its long axis.

In this particular geometry, the current density varies only along the y-axis; there is no variation along the x-axis by symmetry, nor is there variation along the z-axis because of $d \ll \lambda$. Thus, in the absence of bulk pinning, the critical current for vortices to start flowing inside the superconductor can be determined through the study of such edge barrier effects. In the range of the Meissner regime, there is no vortex in the strip if the transport driving current is smaller than the critical current. The current density along the strip, including contributions from the Meissner screen current and the transport current, can be obtained by solving a 2D Maxwell-London equation for superconducting films in a perpendicular magnetic field [102], [105], but while avoiding the divergence of $j(y)$ at the strip edge by making an analytic approximation to numerical solutions

$$j(y) \approx \frac{H_a y}{d\sqrt{\alpha[(W/2)^2 - y^2] + \beta \lambda_\perp^{'} W}} + \frac{I}{2d\gamma\sqrt{(W/2)^2 - y^2 + \delta\lambda_\perp^{'} W}}, \tag{6.2}$$

where the fitting parameters in the expression are given by:

$$\alpha = \frac{1}{4} - \frac{0.63}{(W/\lambda_\perp^{'})^{0.5}} + \frac{1.2}{(W/\lambda_\perp^{'})^{0.8}}, \tag{6.3}$$

$$\beta = \frac{1}{2\pi} + \frac{\lambda_\perp^{'}}{W}, \tag{6.4}$$

$$\delta = \frac{2}{\pi} + \frac{8.44}{W/\lambda_\perp^{'} + 21.45}, \tag{6.5}$$

$$\gamma = arcsin\frac{1}{\sqrt{1 + 4\delta\frac{\lambda_\perp^{'}}{W}}}. \tag{6.6}$$

It should be noted that there are two different conventions that exist in the literature: The $\lambda_\perp^{'} = \lambda/d^2$ in Eq. 6.2, instead of $2\lambda/d^2$, which was first defined in Pearl's original 1964 paper [20]. Having j reach j_{GL} at the edge of the strip $y = \pm W/2$, that is $j(W/2) = j_{GL}$, we can then plot j as a function of y from Eq. 6.2 using different bias conditions, showing the current density distribution at either H_s for a pure magnetic field [Fig. 6.5(a)] or $I_c(0)$ for a pure transport current[Fig. 6.5(b)]. In Fig. 6.5, the current density $j(y)$ is scaled by j_{GL}, whereas y is scaled by the half strip width $W/2$.

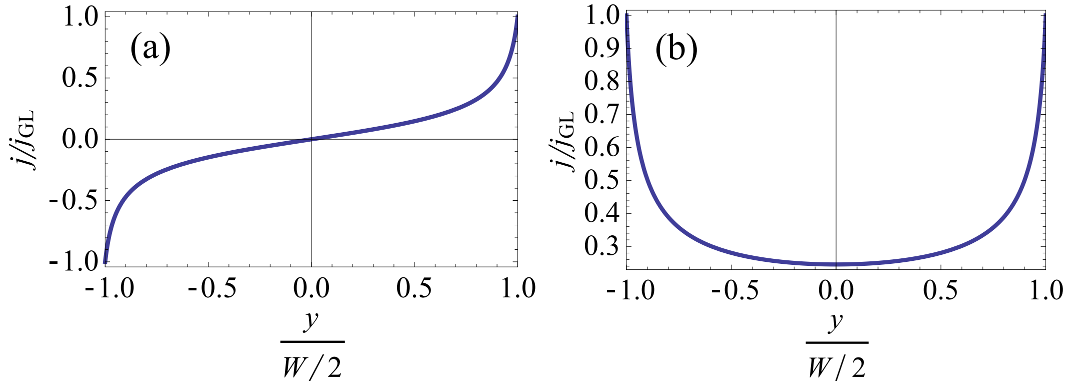

Figure 6.5: Current density along the width ($W = 50\ \mu m$) of the strip for (a) Meissner screening current only, where current $I = 0$, magnetic field $H_a = 1\ Oe$ and (b) transport current only, where current $I = 10\ mA$, magnetic field $H_a = 0$. For both cases, $\lambda_\perp^{'} = 4\ \mu m$, temperature $T = 2.78\ K$.

If we take the value of $j(y)$ at the edge of the strip to be the Ginsburg-Landau depairing current Eq. (6.1), where $y = \pm W/2$, then the critical current that defines the first vortex entering the strip can be described as:

$$I_c(H_a) = I_c(0)(1 - \frac{H_a}{H_s}), \tag{6.7}$$

where

$$I_c(0) = j_{GL} d \sqrt{\lambda_\perp W/\beta} \tag{6.8}$$

is the critical current at the zero applied magnetic field, and

$$H_s = 2 j_{GL} d \sqrt{\beta \lambda_\perp / W} \tag{6.9}$$

is the field at which vortices enter the strip when the transport current $I = 0$ (Fig. 6.2).

Eq. (6.7) describes a linear dependence of the critical current I_c on the applied magnetic field H_a in the Meissner regime. In this regime, there are no vortices in the strip for $I < I_c$, then when I exceeds I_c, vortices enter and are immediately swept across the strip width, thus generating a flux-flow voltage. If there are any defects on the edge, this vortex first entry field can be smaller [106], where the distortion in the current flow pattern causes the current density in the vicinity of the defect to reach j_{GL} earlier.

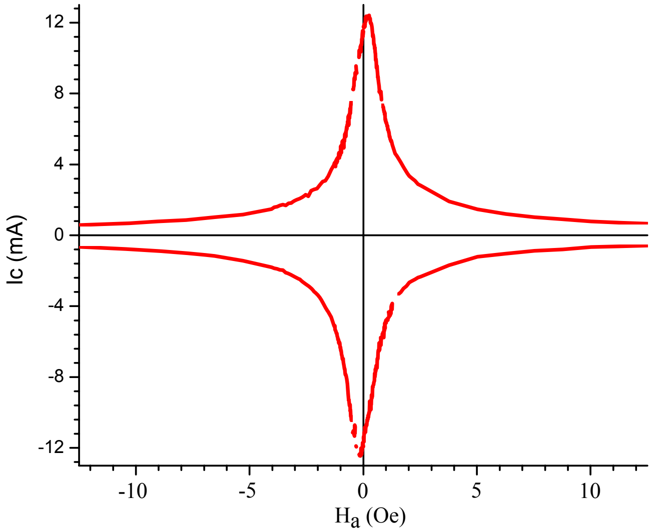

Figure 6.6: Critical current measurement of a NbGe strip showing the asymmetric vortex entry condition caused by the asymmetry on the edge roughness. ± I_c correspond to the entry of vortices from one edge or the other.

We measured a bare NbGe strip, which contained neither a NbN layer, nor any features of channels. In a real sample, it is almost impossible to have identical edges. The roughness of the strip edges will cause the vortices to enter the superconductor more easily from one edge than the other. As shown in Figure 6.6, our measurement results of a bare NbGe strip is consistent with the simulation conducted by Vodolazov and Peeters in 2005 [106]. Not only is the critical current entry condition asymmetric on two edges of the strip, but the measurement results also show an antisymmetric dependence of the critical current on the magnetic field (Figl. 6.6).

For larger H_a, the external field can be sufficient in pushing vortices into the strip, even for $I = 0$. In the absence of any kind of bulk pinning, these vortices arrange themselves in a static dome-shaped structure in the middle of the strip due to the mutual repulsion of the vortices [103, 105]. Assuming the domelike flux distribution extending from a to b, where $a < b$, it then can be characterized by [103]:

$$B_z(y) = \mu_0 H_a \frac{\sqrt{(x-a)(b-x)}}{\sqrt{W^2 - x^2}}, \tag{6.10}$$

where the author in [103] defined the strip width as $2W$, from $-W$ to W.

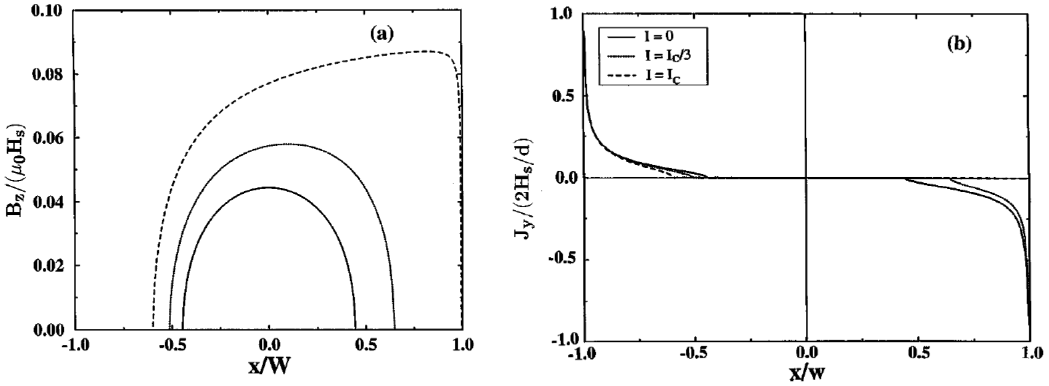

Figure 6.7: Flux-density and current density along the strip width from Benkraouda and Clem [103]. (a) $B_z(x)$ for initial penetration of magnetic flux in an applied field $H_a = H_s/10$, increasing current I pushes the vortex dome toward the right edge, reaching the critical exit condition. (b) corresponding current-density profiles $J_y(x)$. (from Benkraouda and Clem, 1998, p.15105). Note: in this figure, the current is applied along the *y-axis*, and the strip width along the *x-axis* is opposite of the notations discussed in this chapter.

Figure 6.7 shows examples of such results. When fields are applied perpendicular to the strip, and if there are any vortices inside the channels, they will be pushed by the screening current to the middle of the channel and form a dome structure. This process will leave two ends of the channel free of vortices, thus creating a vortex-free region. This means there are no current flows inside the dome and there are no vortices in the current-carrying regions at the edges of the strip.

When $I \neq 0$, the Lorentz force causes the dome to shift toward one edge, and the I_c is reached when the self-field of the transport current plus H_a at the opposite edge overcomes the entry barrier to allow new vortices to enter. New vortices that enter at the left edge of the strip are driven rapidly through the vortex-free region. These vortices join the left side of the dome, and correspondingly push an equal number of vortices out of the dome from the right side of the strip. As in the Meissner regime, I_c decreases as H_a increases [Fig. 6.2(solid line)]. But in the vortex dome regime, the field-dependence is given by [102]:

$$I_c(H_a) = \frac{(j_s d)^2 \lambda_\perp}{2H_a}. \tag{6.11}$$

Our measurement of the uniform channel sample essentially followed the behavior of a standard edge barrier model as described above, particularly in a small field region. $I_c(0)$ and H_s for our uniform channels are not described quantitatively by the

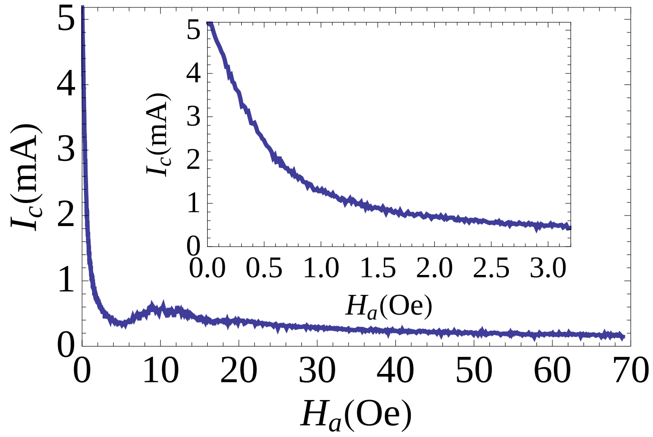

Figure 6.8: $I_c(H_a)$ of a set of 0.5 μm-wide uniform channels on a 50 μm-wide strip, showing basic edge barrier behavior at the small field (inset), and a commensurability effect at the larger field ($H_a \sim 10$ Oe).

simple edge barrier expression because the structure of our sample is not quite the same as the uniform strip (i.e., no channels). Not only can the confinement of the channel change critical current, but the difference of thickness at the edge can also lead to distortion of the screening current, thereby influencing the field entry condition. The confinement effects of the channels can play a role and lead to modifications of $I_c(H_a)$. We always see a slight increase in the critical current at larger H_a (Fig. 6.8), leading us to think that this is caused by the vortex commensurability effect in the confined channels.

6.4 Critical current oscillation with controlling confinement

We extend our study from an unstructured weak-pinning channel to a periodic constriction weak-pinning channel as described in Section 6.2. One can expect that such channel structures will influence vortex dynamics if the confinement from the channel walls distorts the screening currents that circulate around each vortex; this circulation will be different depending on the motion of the vortex through the channel.

6.4.1 Mkrtchyan model for calculating the potential energy in a diamond cell

In the temperature range of our measurements, $\lambda_{\perp}^{NbGe}$, the characteristic extent for the screening currents around a vortex in a thin film is $\sim 40-370\ \mu$m for the a-NbGe in the channels, is clearly much greater than the width of the channels, such that the shape of the channel walls will play an important role in distorting each vortex.

The interaction of a vortex with the channel walls can be understood by considering the model of Mkrtchyan *et al.* for the interaction between a vortex and the interface between two superconductors with different penetration depths [107]. For our strips, the channel corresponds to the superconductor with the larger penetration depth, while the NbN banks have the shorter penetration depth. According to the Mkrtchyan model, a vortex in the channel will experience a repulsive interaction U_i from the i^{th} wall with a distance d_i, keeping the vortex in the channel,

$$U_i \propto \left(\frac{\lambda_{NbGe}^2 - \lambda_{NbN}^2}{\lambda_{NbGe}^2 + \lambda_{NbN}^2}\right) \ln\left(\frac{\lambda_{NbGe}}{d_i}\right). \tag{6.12}$$

If we consider a single vortex located in one of the diamond cells, we can make a crude model of the potential energy landscape by summing the contributions from the interaction of the vortex with each of the four walls of the diamond cell, ΣU_i (Fig. 6.9).

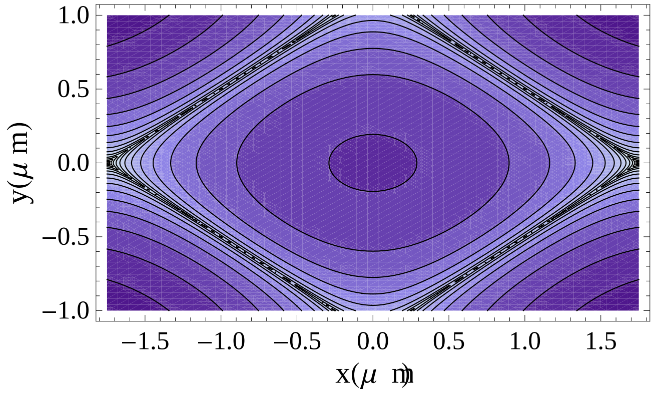

Figure 6.9: Contour plot of model potential for vortex interacting with diamond cell walls, showing the potential energy is at it's lowest point at the center of the diamond cell.

Assumptions in this calculation include the following: first, it does not account for vortices extending beyond one cell; next, it does not treat the aperture at either end of the cell; rather, the cell is treated as a complete diamond; finally, it does not deal with the extended nature of the vortices in the thin-film Pearl regime. This calculation is aiming to give a qualitative understanding of the interaction between vortices and the channel walls. Complex simulations are required for quantitative, more accurate demonstrations of such vortex dynamics and circulating current distribution.

6.4.2 Temperature variation

The presence of diamond-shaped constrictions in the channels results in pronounced oscillations in $I_c(H_a)$ on top of the edge barrier response (Fig. 6.10). $I_c(H_a)$ for the uniform channels does not show the same oscillations of the diamond-shaped channels, although there is a broad increase in I_c around 7 Oe [Fig. 6.10(dashed)]. This is a typical feature that we have observed in most uniform-width channels, as was discussed in Section 6.3. For higher fields, the matching effects are reduced and peaks are absent soon thereafter. This feature had been observed in both numerical simulations [25] and in the experiments [108].

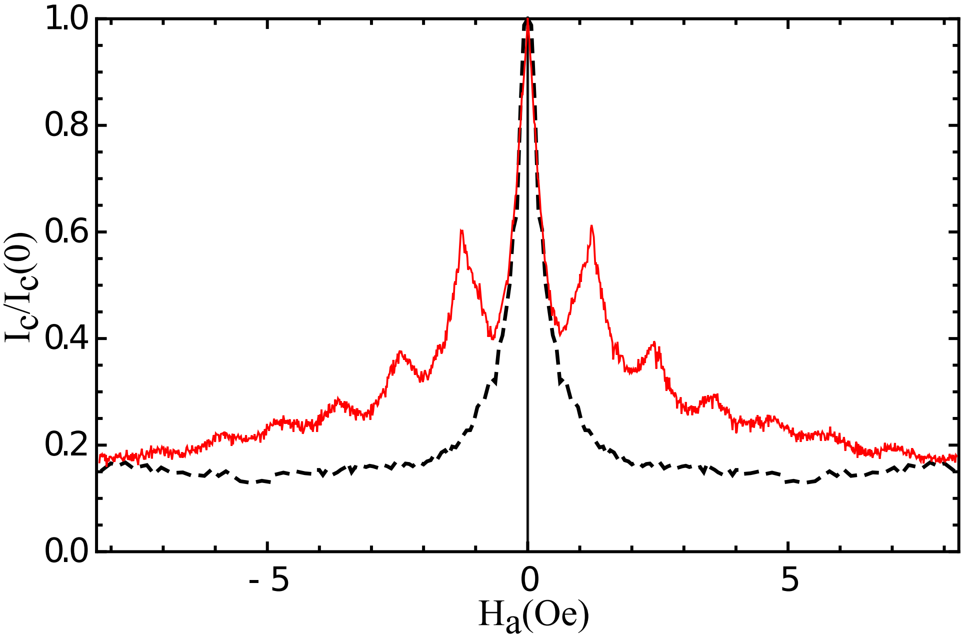

Figure 6.10: Measurement of $I_c(H_a)$ for $p = 2$ μm, $s = 20$ μm, $T = 2.78$ K for a complete field cycle as described in the text (solid). (dashed) $I_c(H_a)$ for 0.5 μm-wide uniform channels ($s = 20\,\mu$m, $T = 2.78$ K).

For this measurement, H_a was increased from 0 to 6.2 Oe, then reduced through 0 to -6.2 Oe, and finally returned to 0. The complete reversibility of $I_c(H_a)$ for this field-cycle indicates that all of the vortices are confined to the channels, as one would expect from a reversible $I_c(H_a)$ for a pure edge barrier. In contrast, if vortices had entered the strong-pinning NbN, observation of hysteresis in $I_c(H_a)$ would be expected.

The oscillations in $I_c(H_a)$ can be observed over a wide range of T [Fig. 6.11(a)], with the relative height of the peaks increasing as T/T_c^{NbGe} approaches 1. A Fourier transform of the $I_c(H_a)$ data [Fig. 6.11(b)] shows that the characteristic frequency of these oscillations, $\omega_H^0 = 1/\Delta H_a$, is independent of T in this range, indicating that the commensurability is determined primarily by the channel geometry.

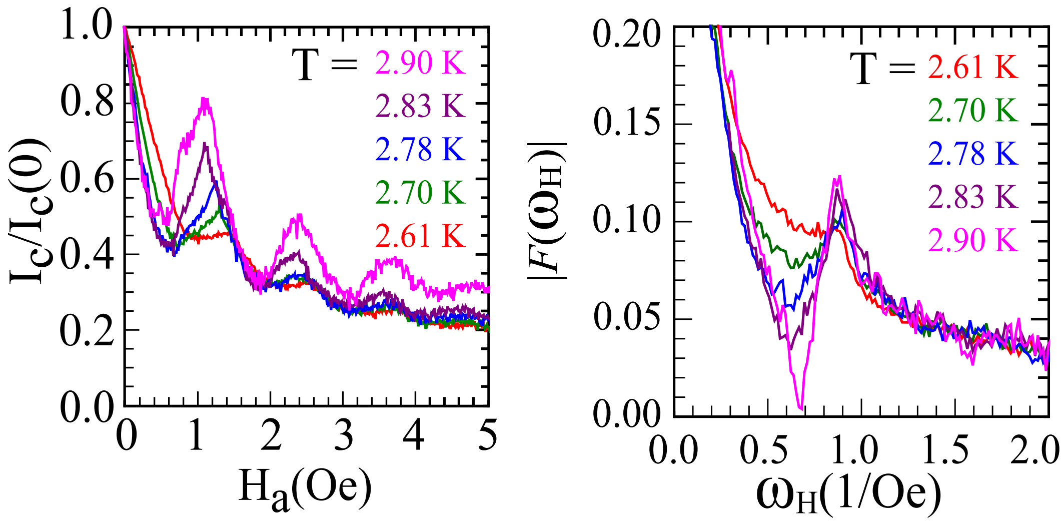

Figure 6.11: (a) Measurement of $I_c(H_a)$ for $p = 2$ μm, $s = 20$ μm for different T as indicated, scaled by corresponding $I_c(0)$. (b) Corresponding Fourier transform magnitudes.

6.4.3 Channel shape variation

We have studied the commensurability in $I_c(H_a)$ further by measuring a series of channel samples with different values of the diamond cell length p and channel spacing s.

Because each vortex corresponds to one Φ_0 of flux ($\Phi_0 \equiv h/2e$), the change in the flux density in the channel ΔB_{ch}, that is required to add one vortex to each diamond cell, will be determined by the area occupied by this flux(Fig. 6.12). For widely separated channels ($s \gg \lambda_\perp^{\mathrm{NbN}}$), the flux will extend $\sim \lambda_\perp^{\mathrm{NbN}}$ into the banks on either side of the channel, while along the channel, the relevant length for the flux is p. Thus, one arrives at a rough estimate, $\Delta B_{ch} \approx \Phi_0/2p\lambda_\perp^{\mathrm{NbN}}$. However, if s is not large when compared to $\lambda_\perp^{\mathrm{NbN}}$, the resulting overlap between vortices in adjacent channels will lead to an underestimate of ΔB_{ch}.

Figure 6.13(a) shows $I_c(H_a)$ at $T = 2.78$ K for $p = 0.5,\ 1,\ 2\,\mu$m, where all three sets of channels had $s = 20$ μm. For smaller p, the dominant peaks in I_c shift to larger H_a,

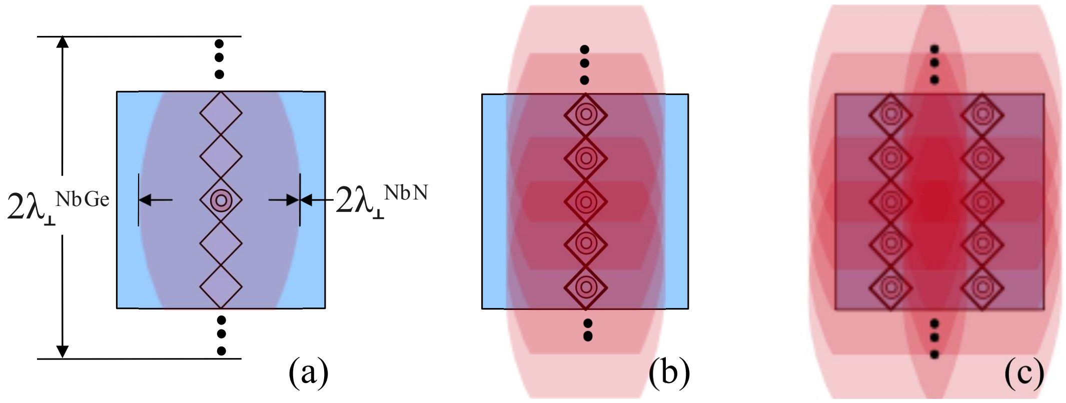

Figure 6.12: Schematic showing the vortex flux distribution in weak-pinning channels and the relation to the matching conditions: (a) showing a single vortex extending over many cells along the channel length and penetrating $\sim 8\mu$m into the NbN banks on either side; (b) at the matching field, with one vortex per cell, where the area occupied by one vortex can be estimated as $2\lambda_\perp^{NbN}p$; (c) when channels are close by, the area occupied by one vortex will simply be $p \times s$ due to the flux overlapping between adjacent channels.

although more complex oscillation patterns develop as well. Nonetheless, the Fourier transforms of the $I_c(H_a)$ data indicate that the lowest characteristic frequency in the spectrum for each p, ω_H^0, varies linearly with p [Fig. 6.13(b)]. This provides evidence that the $I_c(H_a)$ peaks are indeed related to a matching of the vortex distribution to the constriction lattice.

In Figure 6.13(b) we see that $\omega_H^0 \approx 0.6 \times \Delta B_{ch}^{-1}$, thus indicating a somewhat larger ΔH_a is required to achieve a particular ΔB_{ch}. This is likely due in part to neglecting the overlap between vortices ($s = 20\,\mu$m in this case), but is also related to the edge barrier mechanism. As I discussed early in this chapter, B will be somewhat smaller than H_a because of screening effects [104].

In the opposite limit, $s \ll \lambda_\perp^{\mathrm{NbN}}$, vortices in adjacent channels will be highly overlapping and the flux density required for a one-vortex change becomes $\Delta B_{ch} \approx \Phi_0/s\,p$. We have varied the channel spacing s and observed the influence on $I_c(H_a)$, using $s = 5$, 20, $50\,\mu$m with $p = 2\,\mu$m and $T = 2.78$ K for all three sets [Fig. 6.13(c)]. The peak structure shifts to a larger H_a for a smaller s, and the plot of ω_H^0 vs. s in

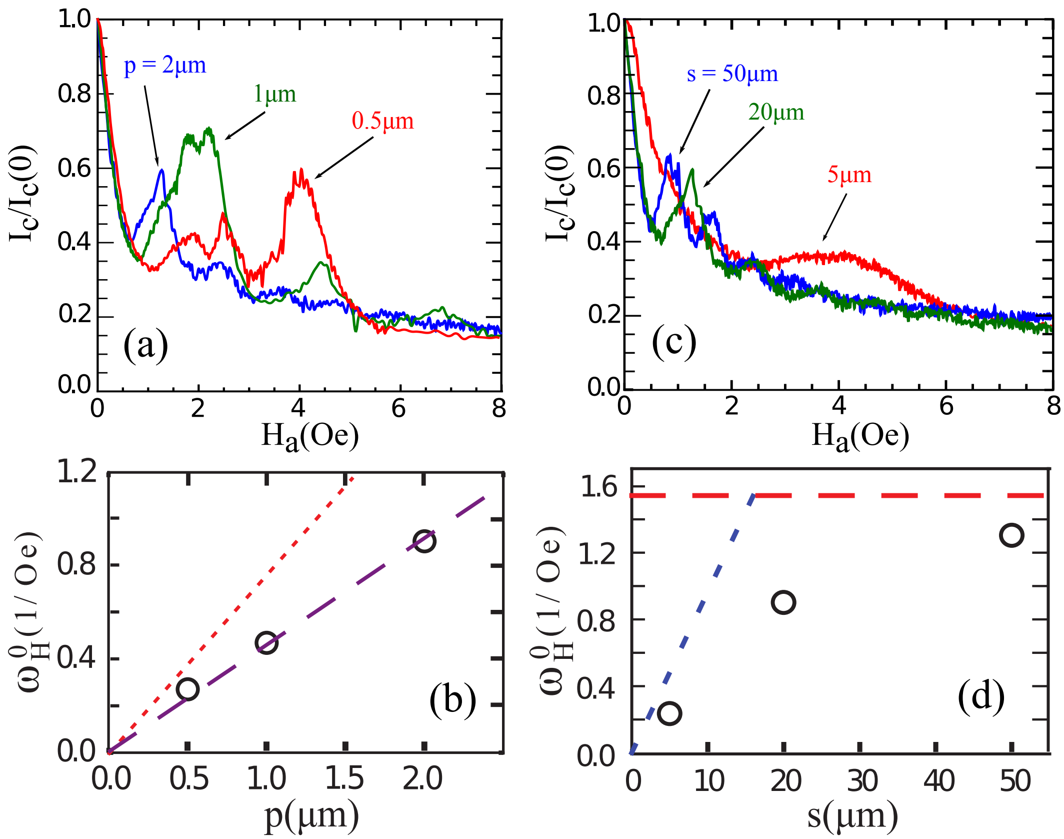

Figure 6.13: (a) $I_c(H_a)$ curves for strips with different p for $s = 20$ μm, $T = 2.78$ K; (b) p-dependence of ω_H^0; dashed line = guide to the eye; dotted line has slope $2\lambda_\perp^{\mathrm{NbN}}/\Phi_0$. (c) $I_c(H_a)$ curves for different s, with $p = 2$ μm, $T = 2.78$ K; (d) s-dependence of ω_H^0; horizontal dashed line at $2p\lambda_\perp^{\mathrm{NbN}}/\Phi_0$, dotted line has slope p/Φ_0.

[Fig. 6.13(d)] follows the trends described above, indicated by the dashed and dotted lines included in the plot. The $s = 50\,\mu$m data approaches the expected ω_H^0 for widely separated channels, while the $s = 5\,\mu$m data is close to the limit of highly overlapping vortices. In both cases, a reduction in ω_H^0 somewhat below ΔB_{ch}^{-1} can be expected because of the edge barrier. A detailed calculation of the flux distribution in the channels that accounts for the channel structure, the two different superconductors, and the strip geometry is beyond the scope of this thesis.

We also measured samples described above at multiple temperatures, as shown in Fig. 6.14. Although more structures are developed at the first few matching

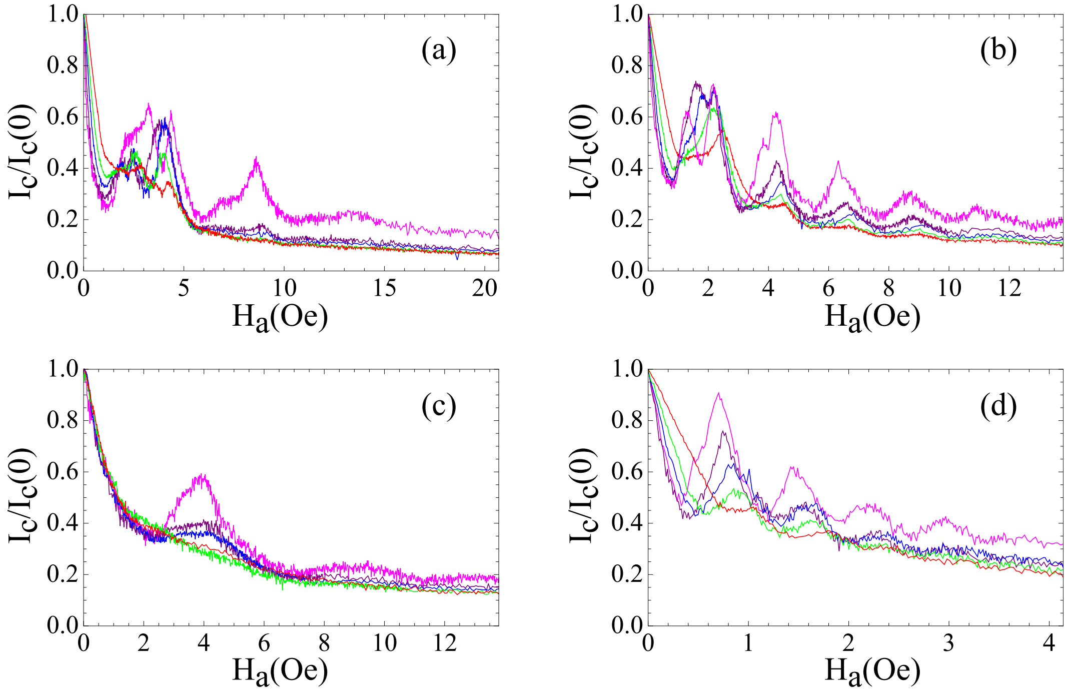

Figure 6.14: Measurement of $I_c(H_a)$ for different T, scaled by corresponding $I_c(0)$. Sample parameters are (a) $s = 20\ \mu m$, $p = 0.5\ \mu m$, (b) $s = 20\ \mu m$, $p = 1\ \mu m$, (c) $s = 5\ \mu m$, $p = 2\ \mu m$, (d) $s = 50\ \mu m$, $p = 2\ \mu m$. All samples have $b = 1.5\ \mu m$ and the temperature variation is such that higher temperature corresponds to a larger magnitude of $I_c/I_c(0)$ oscillations.

peaks for smaller constriction period – cell length, overall structures are similar to the measurement results we discussed above. We also notice that the magnitudes of the oscillation peaks are smaller for $s = 5\ \mu$m [Fig. 6.14(c)] when compared to samples with larger spacing. This reduction in the magnitude of I_c at the matching field is mainly due to the collective effect formed when channel spacing reaches a low limit at, $s < \lambda_{\perp}^{NbN}$. In this case, inter-channel vortices interact, forming a crystalline arrangement and moving in a collective motion. We will discuss this more in Chapter 8.

6.5 Magnetic hysteresis

As discussed earlier in this chapter, at the edge of a superconducting strip, vortices will enter when H_a reaches H_s. Since the penetration depth λ and coherence length ξ vary with T as discussed in Chapter 2, one would expect a longer λ at higher temperatures, thus a smaller H_s, whereas a larger H_s at lower temperatures is expected. Applying the standard edge barrier expression for H_s (Eq. 6.9) with our estimated film parameters leads to $H_s^{\mathrm{NbGe}} \sim 2.6 - 0.7\,\mathrm{Oe}$ in the temperature range we studied, although the entry field into the ends of the NbGe channels is likely somewhat smaller than the H_s^{NbGe} estimate when current distortions are considered at the channel ends. Indeed, we typically observe the first entry of vortices into the channels followed by oscillations in $I_c(H_a)$ for $H_a \sim 1$ Oe. Performing a similar estimate for vortex entry into the NbN banks yields $H_s^{\mathrm{NbN}} \sim 8\,\mathrm{Oe}$. As discussed in Chapter 2, the variation of λ is more abrupt when the T is close to T_c than when T is far from T_c. Since the measurement temperatures are below $T_c^{NbGe} = 2.93\mathrm{K}$, which is far smaller than $T_c^{NbN} \approx 10\mathrm{K}$, there is almost no temperature dependence for $\lambda_\perp^{NbN}$ in our measurements.

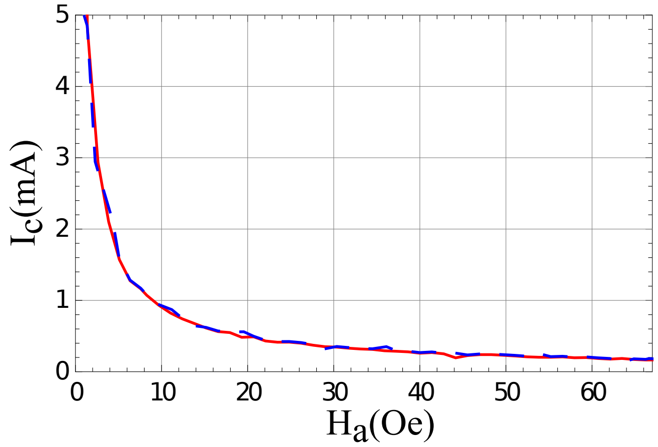

Figure 6.15: Critical current of a wide channel (channel width: ~2 mm) as a function of field while the field was ramped from zero to 67 Oe (solid) and back to zero (dashed) showing a bare NbGe strip $I_c(H_a)$ retraced completely even when $H_{max} \gg H_s^{\mathrm{NbN}}$. Strip width $w = 200\ \mu\mathrm{m}$, and $T = 2.78$ K.

We can probe the possibility of vortex entry into the NbN by increasing H_a to progressively larger values H_{max} before reducing it and checking the reversibility of $I_c(H_a)$, as vortices trapped in the strong-pinning NbN will exhibit an irreversible magnetic response and will offset the net magnetic field experienced by the vortices confined to the channels. For a pure edge barrier, one with no bulk pinning and no channels, I_c is reversible with H_a up to relatively large fields. In Fig. 6.15, the $I_c(H_a)$ curve can be retraced completely even after we ramped H_{max} to $\sim 70\ Oe$. We see the same reversibility in our channels as long as the fields aren't too large (Fig. 6.10).

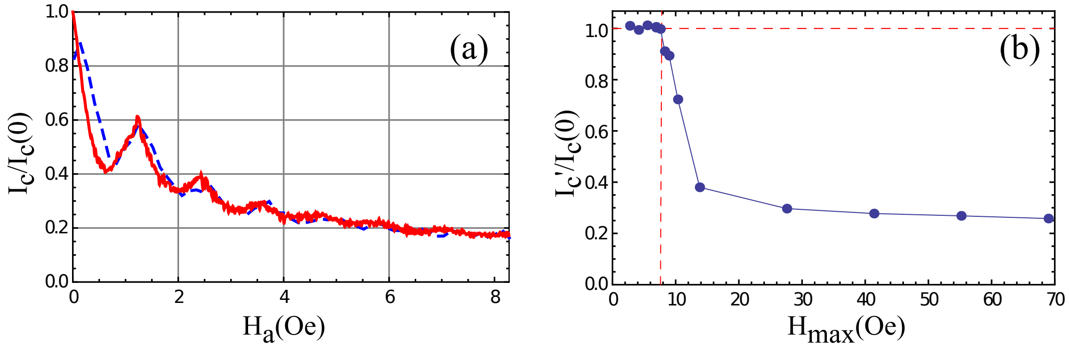

Figure 6.16: (a) Magnetic hysteresis in $I_c(H_a)$ for a sweep field slightly larger than the NbN entry condition, with $H_{max} \sim 8.3$ Oe; solid line is outgoing sweep whereas the dashed line represents a return field sweep; (b) a plot of the critical current when the field reduced to zero $I_c^{'}/I_c(0)$ as a function of H_{max} showing the determination of the NbN vortex entry field. Both have $s = 20\ \mu$m, and were measured at $T = 2.78$ K, and here (a) has $p = 2\ \mu$m, while (b) is a ratchet sample and has $p = 4.5\ \mu$m.

However, when bulk pinning as well as channels are present in the system, for $H_{max} \gtrsim 8\,\mathrm{Oe}$, $I_c(H_a)$ becomes hysteretic, with the opening of the hysteresis loop growing with H_{max} [Fig. 6.16(a)]. To determine the threshold field for magnetic hysteresis experimentally, we measured our samples repeatedly while incrementing H_{max}. If $H_{max} < H_s^{NbN}$, the critical current at $H_a = 0$ on the return sweep which we call $I_c^{'}(0)$, will be the same as it was before the field was increased, that is $I_c^{'}(0)= I_c(0)$. As soon as the maximum sweep field H_{max} is larger than H_s^{NbN}, the pinned vortices in the NbN cause the local fields in the channels to be larger than H_a on the return sweep. At the point of $H_a = 0$ Oe, some vortices will still be trapped in the strong-pinning NbN, which effectively shifts the $I_c'(0)$ to a smaller number. Therefore $I_c'(0)$ will be less than $I_c(0)$ [Fig. 6.16(b)].

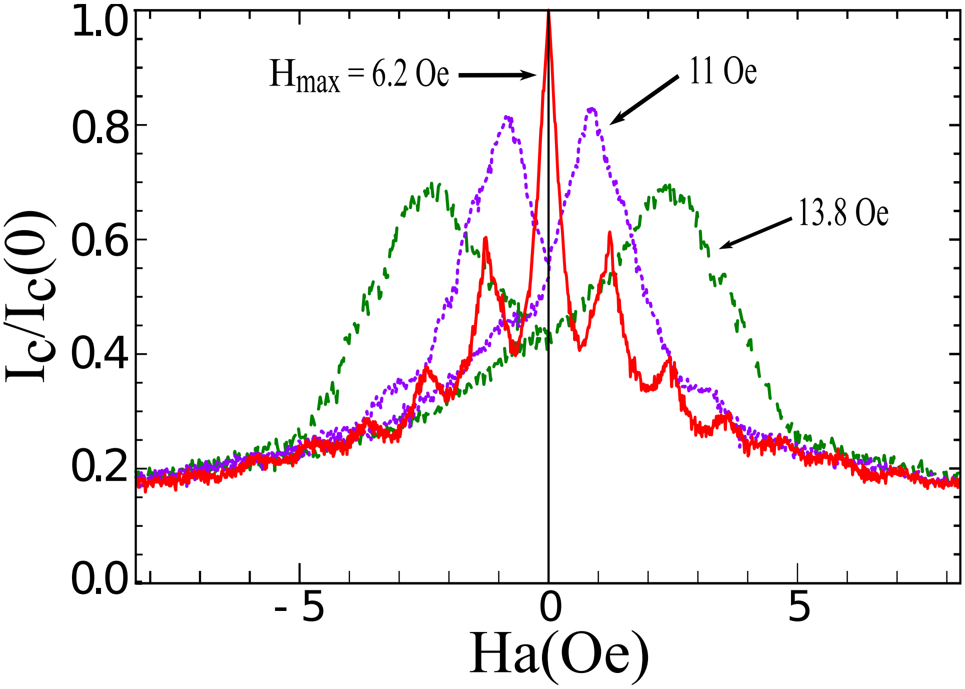

Figure 6.17: Magnetic hysteresis in $I_c(H_a)$ for larger field sweeps, with H_{max} as indicated for $s = 20\ \mu$m, $p = 2\ \mu$m, $T = 2.78$ K. The curve for $H_{max} = 6.2$ Oe is the same as in Fig. 6.10 with no hysteresis.

Also, the matching peak structure on the return branches of $I_c(H_a)$ becomes washed out for larger H_{max}, as the disordered distribution of vortices that occurs in the strong-pinning NbN when H_a is reduced randomizes the potential for the vortices moving in the channels (Fig. 6.17).

6.6 Dynamical hysteresis in IVCs around the matching peaks

For H_a below the threshold to introduce vortices into the NbN banks, in the vicinity of the $I_c(H_a)$ matching peaks, we often observe a completely different type of dynamical irreversibility consisting of hysteresis in the IV curves. Figure 6.18(a) shows two example IVCs for the outgoing and return current sweeps, one between matching peaks with no hysteresis, and the other near the second matching peak with clear hysteresis.

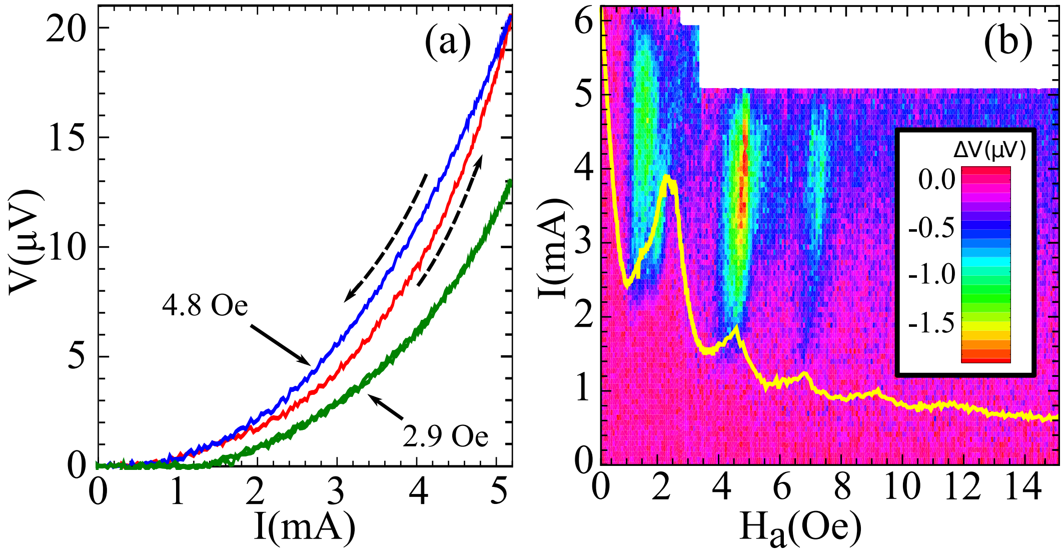

Figure 6.18: (a) Example of dynamical hysteresis in IV curve in the vicinity of one of the matching peaks (red/blue) compared to a reversible IV curve (green) [$s = 20$ μm, $p = 1$ μm, $T = 2.70$ K]. (b) Density plot of the difference of the flux-flow voltage between the outgoing and return current sweeps [$\Delta V = V_{out}(I) - V_{return}(I)$] as the color scale for different H_a; corresponding $I_c(H_a)$ is superimposed (yellow).

We can combine all of the measured IVCs for a particular channel configuration and T by making a density plot, where the color scale is the difference between the voltage on the outgoing and return current sweeps. We superimpose the corresponding $I_c(H_a)$ curve for reference [Figure 6.18(b)]. This particular example shows regions of dynamical hysteresis near the first three $I_c(H_a)$ peaks. Over the range of drive frequency that we have studied, $20 - 400$ Hz, we observe no change in this response. The upper limit of the data on the current axis is set by the point where the flux-flow voltage approaches the Larkin-Ovchinnikov instability point as discussed in Chapter 2, where the channels switch abruptly to the normal state [14].

This hysteresis in the IVCs may correspond to a distortion of the vortex distribution as the driving current is reduced, allowing the vortices to keep flowing at higher velocities than when the current was initially increased.

As discussed in Chapter 3, the hysteretic dynamics for vortices in periodic arrays of antidots were recently reported [43]. These were connected to previous theoretical work involving the transition to turbulent flow related to the interplay between interstitial vortices and those pinned in the antidots [36, 45]. The origin of the hysteresis in our system is likely somewhat different, as all of the vortices are confined to the weak-pinning channels.

sample label	period(μm)	spacing(μm)	number of hysteresis vs. temperature				
			2.61 K	2.70 K	2.78 K	2.83 K	2.90 K
d1	0.5	20	1	1	1	1	0
d2	1	20	3	3	2	2	0
d3	2	5	0	0	0	0	0
d4	2	20	0	1	1	0	0
d5	2	50	0	1	1	0	0

Table 6.2: Number of dynamic hysteresis at different temperature for all the samples we measured.

Other than the sample discussed in this section, where $s = 20$ μm, $p = 1$ μm, we measured samples with other channels spacings ($s = 5$ μm, 50 μm), and samples with other periodicities ($p = 0.5$ μm, 2 μm). All of the samples were measured at five different temperatures ($T = 2.61 \sim 2.90$ K). Table 6.2 shows dynamical hysteresis at multiple samples as well as at multiple temperatures. Although the dynamical hysteresis always appears in the vicinity of the matching peaks that we observe in $I_c(H_a)$, some of the samples show dynamical hysteresis more than once in a single measurement. It appears 3 times in the measurement for the sample d2 at $T = 2.70$ K.

We note that the diamond channels with the smallest spacing, $s = 5\,\mu$m, did not exhibit any such hysteresis, where strong interactions between vortices in adjacent channels may have prevented the instability that produced the hysteresis in other channel samples. Also, none of the channel configurations that we have studied exhibited this type of hysteresis at the highest temperature of our measurements, where $T = 2.90$ K. We are currently investigating further this dynamical hysteresis in our channels.

6.7 Conclusion

To summarize, we have measured vortex dynamics in weak-pinning channels containing periodic constrictions that are small compared to the vortex size. Over much of the magnetic field range that we studied, all of the vortices are confined to the channels and the channel structure results in strong matching effects between the vortex distribution and the constriction lattice. In the vicinity of the matching peaks, we often observe a dynamical hysteresis in the vortex response that may be related to a distortion of the vortex distribution.

Chapter 7

Asymmetric weak-pinning superconducting channels: vortex ratchets

7.1 Introduction

The general issue of interacting particles in confined geometries is important in a variety of physical systems, including colloids flowing through microchannels [109] and Wigner crystals [110] in the presence of constrictions [111]. Using appropriate asymmetries, such tailored potentials can also form model systems for studying ratchet dynamics, with applications ranging from superconducting devices to investigations of biomolecular motors [26].

I demonstrated the matching effects of vortices moving through periodic constrictions in superconducting weak-pinning channels in the previous chapter. In this chapter, I introduce a vortex ratchet using two-dimensional guides in generating asymmetric channels for vortex motion. In our structures, the potential asymmetries arise from differences in the interaction strength between vortices and the channel walls, resulting in a substantial ratchet effect for the motion of vortices through the channels.

Our design is related to a previous vortex ratchet proposal [112], although our ratchet is in a somewhat different parameter regime. In this 1999 paper by Wambaugh *et al.*, a set of 2-D asymmetric channels, each consisting of a chain of triangular cells many times larger than the size of a vortex characterized by the penetration depth λ, had been studied with the molecular dynamics simulations of vortices.

More specifically, I present measurements of vortex dynamics in the channels and compare them with similar measurements on a set of uniform-width channels. While the uniform-width channels exhibit a symmetric response for both directions through the channel, the vortex motion through the asymmetric channels is relatively different, with substantial asymmetries in both the static depinning and dynamic flux flow. This vortex ratchet effect has a complex dependence on the magnetic field and driving force amplitude.

7.2 Sample characteristics

The results presented in this chapter consist of measuring a set of weak-pinning channels with 200 nm-thick films of a-NbGe and 50 nm-thick films of NbN on a Si substrate, and we have designed many of the channels such that the walls have an asymmetric sawtooth pattern as described in Chapter 5.

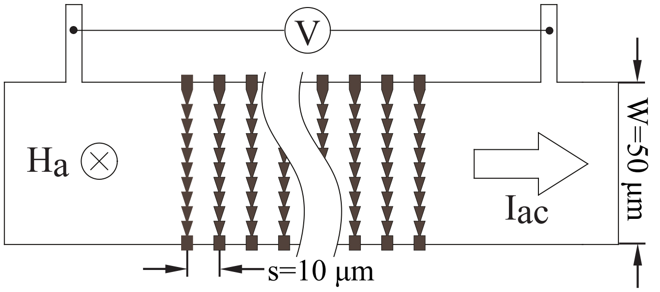

Figure 7.1: Schematic of strip with ratchet channels showing sample parameters; in this case, channel spacing $s = 10\ \mu m$ and strip width $w = 50\ \mu m$.

The sample design and parameters are essentially the same as the diamond sample discussed in the previous chapter (Chapter 6), but in this case the channel size and shape are different; and there is also a slight T_c difference due to different batches of films used. The channel depth is $\sim 88\ nm$. Our layout consists of a strip with multiple pairs of probes for sensing the voltage drop V due to vortex motion (Fig. 7.1). A transport current driven through the strip with an external supply generates a transverse Lorentz force on the vortices.

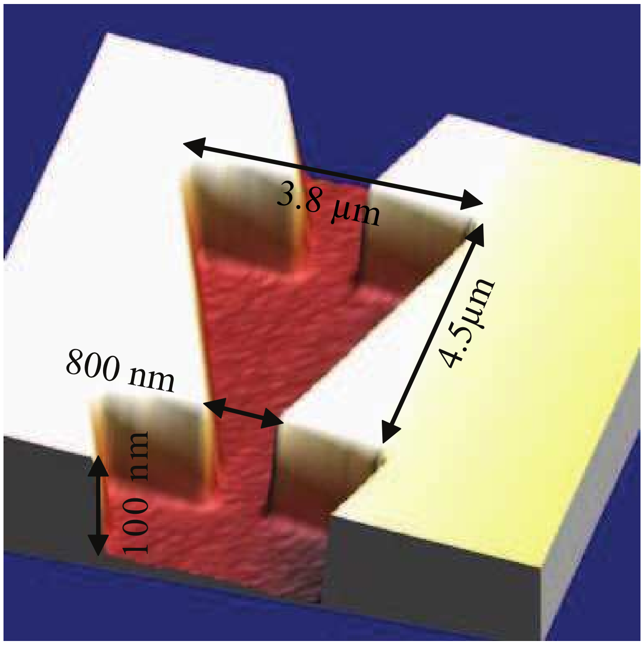

Figure 7.2: Atomic Force Microscope (AFM) image showing a ratchet cell with period $p = 4.5\ \mu$m; and $b = 1.5\ \mu$m.

In between each pair of voltage probes is an array of identical channels – one array consists of 50 channels each with a constant width of 2 μm; another array has 30 ratchet channels with channel spacing $s = 10\ \mu$m, cell period $p = 4.5\ \mu$m and half-width $b = 1.5\ \mu$m [Fig. 7.2]; yet another array contains 30 identical ratchet channels, all oriented in the opposite direction across the strip as a reference sample. Again, we perform our measurements with the strip immersed in a pumped helium bath with a temperature stability of 0.2 mK/hr. Our results presented here were obtained at $T = 2.78$ K, and our measured transition temperature for the a-NbGe is

$T_c = 2.88$ K. The reason in choosing the measurement temperature 2.78 K is largely for the convenience of the experiment's purpose. In the next chapter, I will show measurements of the vortex ratchet at other temperatures.

7.3 Theoretical treatment - calculate potential energy of a vortex with Mkrtchyan model

At the temperature of our measurements, we estimate the penetration depth of the NbN to be $\lambda_{NbN} \approx 0.5$ μm and that of NbGe to be $\lambda_{NbGe} \approx 1.9$ μm, based on the film parameters and the standard dirty-limit expressions (Eq. 2.7 – 2.8), assuming a two-fluid model for temperature dependence. Furthermore, the thin-film penetration length is

$$\lambda_{\perp} = 2\lambda^2/d, \tag{7.1}$$

where d is the thickness of the superconducting film. $\lambda_{\perp}$ sets the characteristic extent for the screening currents around a vortex in a thin film of ~ 42 μm for the NbGe in the channels, clearly much greater than the width of the channels, such that the shape of the channel walls will play an important role in distorting each vortex.

As I discussed in Chapter 6, the interaction of a vortex with the channel walls can be understood by considering the model of Mkrtchyan *et al.* [107] for the interaction between a vortex and the interface between two superconductors with different penetration depths (Eq. 6.12). Similarly, if we consider a single vortex located in one of the ratchet cells, we can make a crude model of the potential energy landscape by summing the contributions from the interaction of the vortex with each of the three walls of the ratchet cell, ΣU_i [Fig. 7.3(a)]. Again, we only expect to get a qualitative picture with this simple model, as the limitations of this model were discussed in the last chapter (Chapter 6).

The derivative of this potential along the central symmetry line of the cell exhibits an asymmetric force on the vortices [Fig. 7.3(b)]. Thus, the two sloped walls result in a gradual increase in the potential energy as the vortex approaches the aperture in the "easy" direction, while the potential energy grows abruptly as the vortex approaches the wide back wall of the ratchet cell for motion in the "hard" direction.

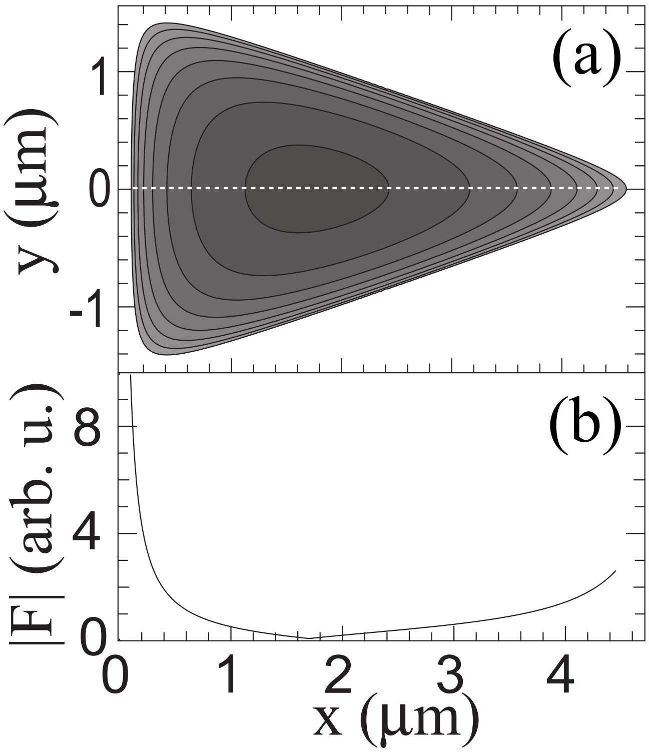

Figure 7.3: (a) Contour plot of model potential for vortex interacting with ratchet cell walls. (b) Magnitude of the corresponding force along the center of the channel.

7.4 Critical current measurements on uniform channels

The measurement procedure here is similar to the one I described in the previous chapter for our diamond samples. For each measurement sequence, the strip was heated to ~ 15 K, above T_c for both the NbGe and NbN films, and was then cooled in a zero applied magnetic field; a μ-metal shield reduced the background magnetic field below 13 mG. All field-dependence data were acquired while increasing the magnetic field H_a from zero, where we generated H_a with a superconducting coil.

We characterize the transition from the static state to a dynamical flux flow regime by measuring the critical current in the conventional way, that is, by measuring the IVC as described earlier, then using a 1 μV criterion to define the critical current I_c as I discussed on Chapter 5. Also as discussed in Chapter 6, measurements of the field dependence $I_c(H_a)$ on the 2 μm-wide uniform channels display a similar response to the characteristic of an edge barrier for a thin, weak-pinning superconducting strip in a perpendicular magnetic field, where the entry of vortices at the strip edge is determined by the distortion of the current density across the width of the strip [102, 105].

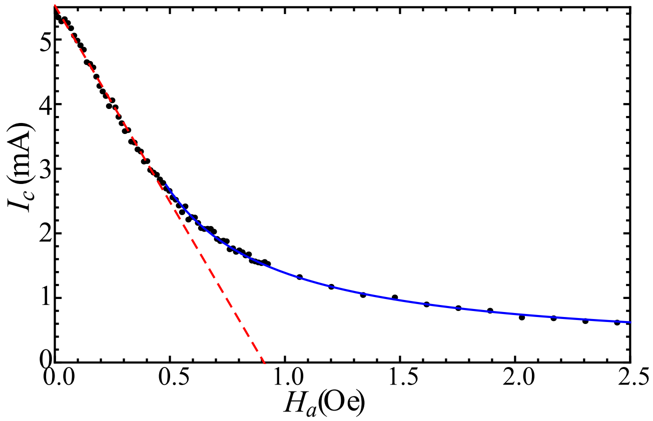

Figure 7.4: $I_c(H_a)$ for uniform-width channels at low magnetic fields with linear fit (dashed) and H_a^{-1} fit (solid), described with edge barrier model. H_s is the field limit for vortex entry into the superconductor at $I = 0$

I_c is at the maximum when $H_a = 0$, where I_c is determined by the entry of vortices and antivortices at opposite edges of the strip due to the self-field of I. As H_a is increased, $I_c(H_a)$ initially decreased linearly [Fig. 7.4(dashed line)], as the self-field and H_a added with the same sense at one edge are able to exceed the vortex entry condition for a progressively smaller I. In this regime, there are no vortices present in the strip for $I < I_c$, while larger currents result in a dynamical flux flow state with vortices entering the strip at one edge and moving across to the other edge.

The measurements of $I_c(H_a)$ for the 2 μm-wide uniform channels essentially follow this behavior. I_c is symmetric with the direction of I and the sense of H_a [Fig. 7.5(dashed line)], indicating that the channels are symmetric and the strip edges at the ends of the channels do not have any significant roughness asymmetries [106]. This is consistent with the entry of vortices only into the channels at the edge of the strip, but not into the strong-pinning NbN banks, as one would expect when $H_a < H_s^{NbN}$ (H_s^{NbN} is the surface entry field of NbN film as described in Eq. 6.9), based on the lower edge barriers at the channel edges compared to the thicker NbN banks.

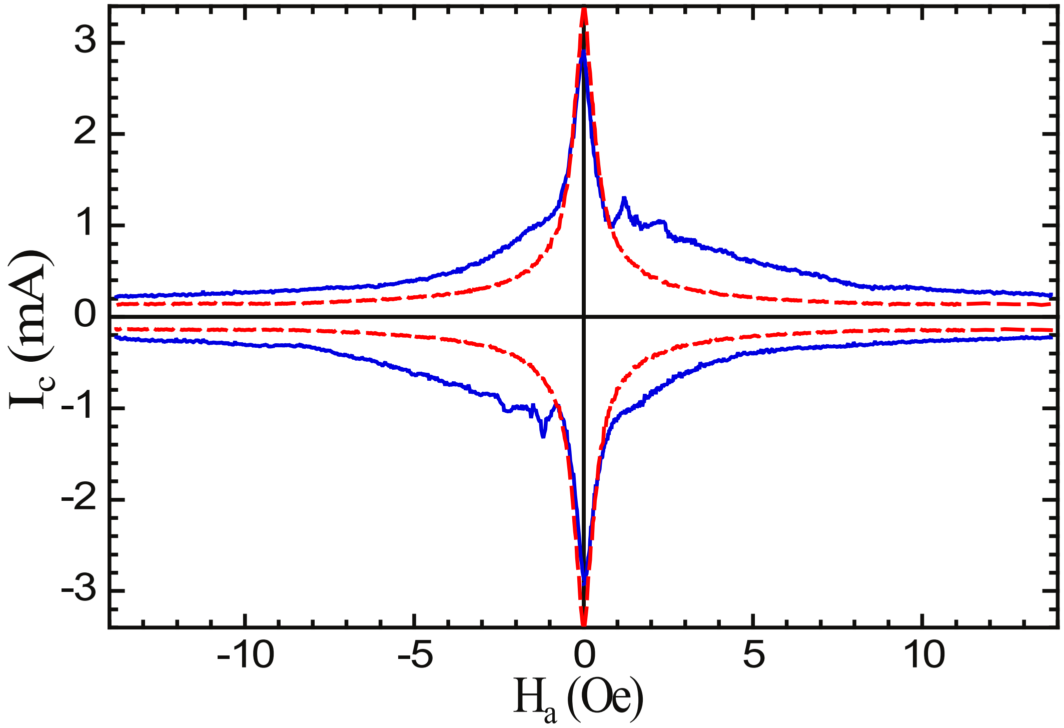

Figure 7.5: Critical current variation with H_a – ratchet channels (solid) and uniform-width channels (dashed).

7.5 Critical current measurements on ratchet channels

For the ratchet channels, I_c is also at maximum when $H_a = 0$, with an initial linear decrease as H_a increased. However, in contrast to the uniform-width channels, I_c is weakly asymmetric with a $\sim 15\%$ difference for the two polarities of I [Fig. 7.6(a)].

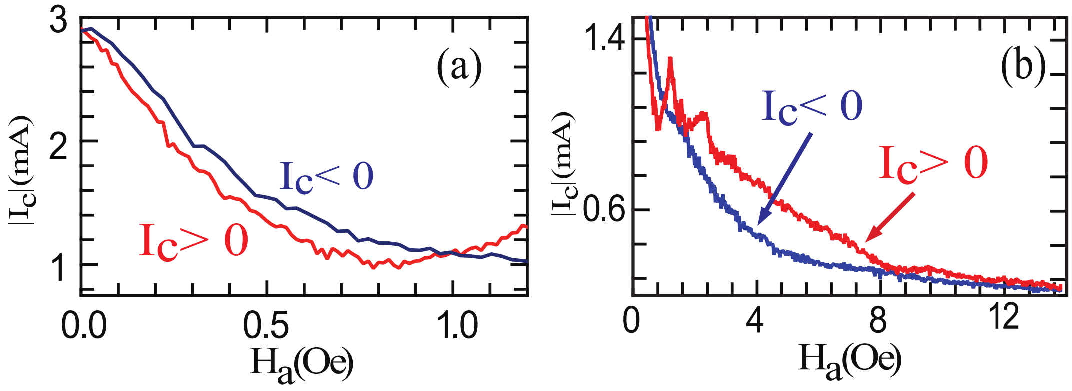

Figure 7.6: Ratchet $I_c(H_a)$ for both senses of I at (a) small H_a, (b) large H_a.

In this low-field regime, where I_c corresponds to the entry of vortices into the vortex-free state of the channels, the smaller I_c has the sense of the bias current pushing the vortices in the hard direction of the ratchet. This is the reverse of what might initially be expected, and I will address this in more detail later in this chapter. As we can see from Fig. 7.5(solid line), when H_a is reversed, the sense with the smaller I_c inverts as well, again corresponding to vortex motion in the hard direction.

For larger magnetic fields, $I_c(H_a)$ deviates from a linear decrease [Fig. 7.6(b)], as in the uniform-width channel measurements when a static vortex dome can be formed in the channels before I reaches I_c. In this regime, the ratchet channel I_c develops a substantial asymmetry with respect to the sense of I. Vortices sit statically in the ratchet channels for $I < I_c$, and thus can explore the asymmetry due to the shape of the ratchet channel walls as I is increased, such that vortices depin and flow at a smaller I when the Lorentz force is oriented in the easy direction. I_c for the sense of

I pushing vortices in the hard direction of the ratchet becomes considerably larger than that for the easy direction and exhibits a sequence of peaks in regions where I_c actually increases with H_a. A more detailed discussion about this type of critical current oscillations was discussed in Chapter 6.

Thus, at the start of this regime, the critical currents for the two directions of vortex motion actually cross [Fig. 7.6(b)]. This is consistent with the antisymmetry of $I_c(H_a)$. That is, for the opposite sense of H_a, the smaller I_c occurs for the opposite sense of I and thus the same spatial direction occurs through the ratchet.

The peak structure in I_c for the hard direction of the ratchet is likely due to the commensurability effect of vortices interacting with the weak-pining periodic constricted channels. This indicates the abrupt crossing of I_c for the two senses of current corresponds to a transition from the vortex entry state to the matching state, where each maxima in the I_c corresponds to an integer number of vortices in each ratchet cell.

7.6 Dynamical flux-flow state - measurement of ratchet rectification signal

With the oscillatory current applied along the sample strip, one side of the curve typically has a larger voltage response than the other for ratchet channels. By plotting both the negative and positive branches of the IVC in the first quadrant, the substantial asymmetry of the response for the ratchet channels is apparent. Furthermore, from the IVC for the ratchet channels, there are clear asymmetries both in the critical currents at which the vortices begin to depin from the static state and in the flux flow resistances, which is inversely related to the vortex dynamic friction in the channels. A general method to characterize asymmetries in both static and dynamic properties involves averaging $V(t)$ over a complete cycle, such as the trace in Figure

7.7(b), to obtain V_{dc}.

$$V_{dc} = \frac{1}{T}\int_0^T V(t)dt, \tag{7.2}$$

where T is the a period of the drive signal.

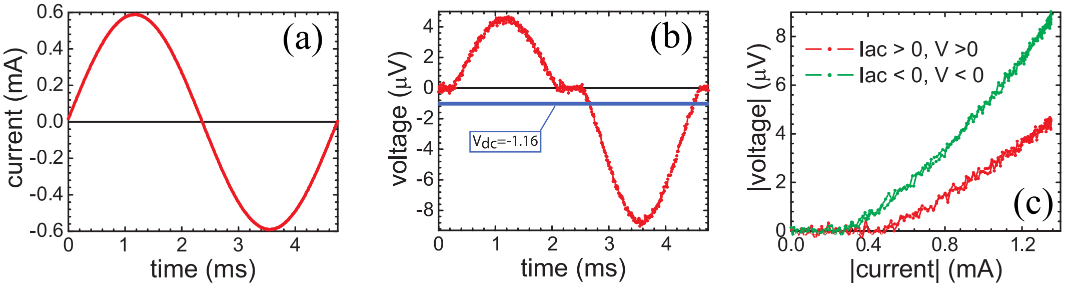

Figure 7.7: (a) A sinusoidal current drive $I(t)$. (b) $V(t)$ for ratchet channels; $I_{ac} = 0.59$ mA. (c) IVC for ratchet channels plotted with positive and negative branches in the first quadrant for comparison.

For a value of H_a corresponding to the IVC of Figure 7.7(c) for the ratchet channels, V_{dc} will clearly be non-zero, while for uniform-width channels, we always observe $V_{dc} = 0$ for all H_a.

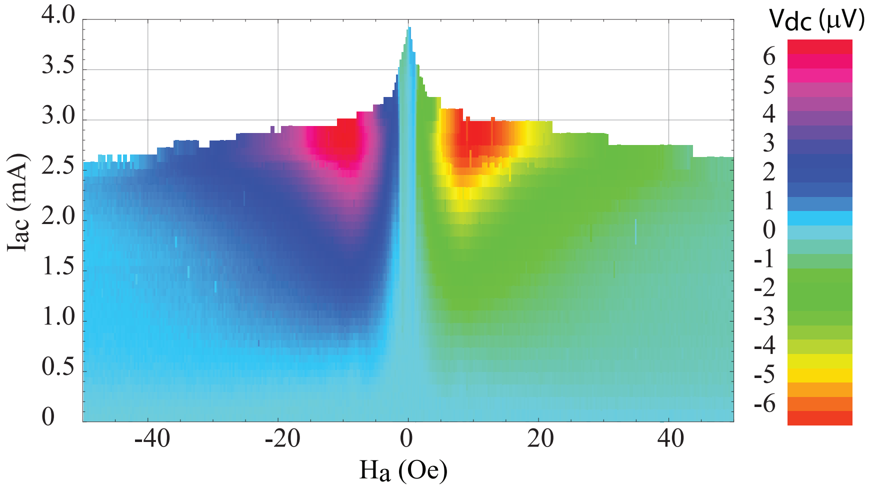

Figure 7.8: Density plot of V_{dc} *vs.* I_{ac} and H_a. Ratchet sample with $p = 4.5$ μm, $b = 1.5$ μm and $s = 10$ μm.

We map the variation of V_{dc} with H_a and I_{ac} for the ratchet channels (Fig. 7.8) by zero-field cooling, then measure $V_{dc}(I_{ac})$ while incrementing H_a toward positive values.

We zero-field cool again in order to measure the $H_a < 0$ response by incrementing H_a from zero toward negative values.

For each H_a, we perform our standard measurement of V_{dc} using a burst of sinusoids with amplitude I_{ac} while stepping to progressively larger values of I_{ac}. For any H_a, $V_{dc}(I_{ac})$ is generally zero for small I_{ac}, when $I < I_c(H_a)$ for both polarities. For larger I_{ac}, $|V_{dc}|$ tends to grow, thus corresponding to an increase in the vortex velocity through the channels, until an instability occurs and the channels switch out to the normal conducting state (Fig. 7.9).

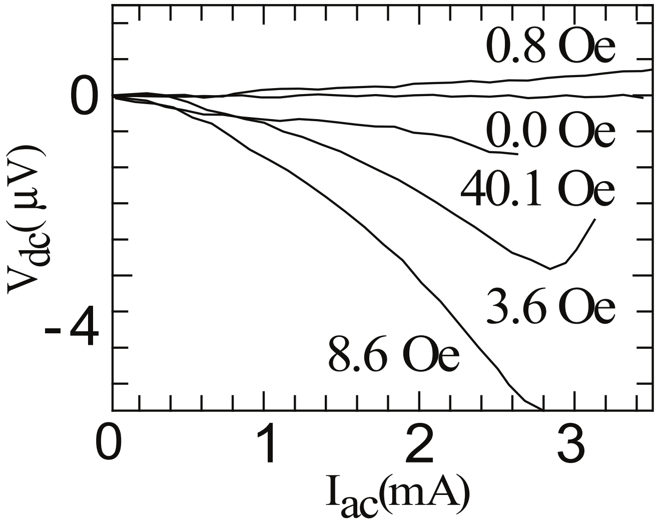

Figure 7.9: $V_{dc}(I_{ac})$ for indicated values of H_a.

In general, for a rocking-ratchet, when the driving frequency reaches a limit, the ratchet rocks too quickly for particles to respond. In this regime, particles won't be able to move to the next cell in one period. A decrease of ratchet rectification is expected [71]. A more detailed discussion about vortex ratchet measurements in adiabatic state can be found in Chapter 4.

The switching point is independent of the frequency of our $I(t)$ sinusoid, at least up to 2 kHz, and the sample is immersed in liquid helium, thus making simple Joule heating unlikely as the cause. Instead, the curvature in the IVC at large I_{ac} (Fig. 7.10) suggests that the switching is related to the Larkin-Ovchinnikov vortex core instability mechanism [14] as discussed in Chapter 2, perhaps with a related self-heating effect as evidenced by the H_a-dependence of the maximum I_{ac} visible in Fig. 7.8 [18].

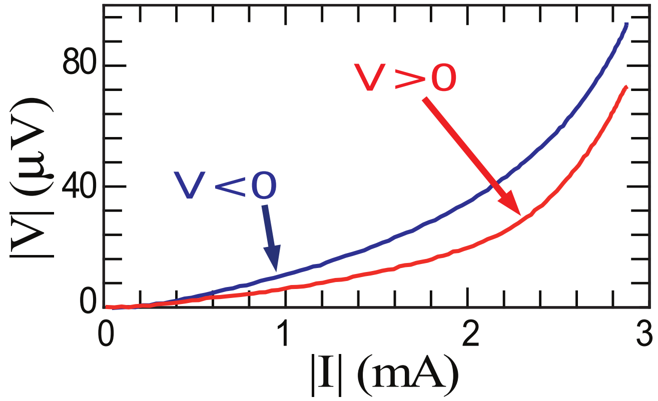

Figure 7.10: IVC for $H_a = 8.6$ Oe measured for large I_{ac} out to Larkin-Ovchinnikov instability.

Due to experimental constrain and the limit on the vortex response imposed by the Larkin-Ovchinnikov instability velocity, it is difficult to increase the frequency to the point of a characteristic frequency limit. Our system, measured at driving current frequency $f = 210\ Hz$, should be far below the characteristic frequency limit, and therefore is operated in an adiabatic state. In fact, almost all of the vortex ratchets implemented are showing an adiabatic response [26, 55].

Normally, the thermal effects can play a significant role in such rocking-ratchet. But this does not seem to be the case for our ratchet, at least not experimentally. It is difficult to test this temperature variation for our ratchet system, not only because of the thermal energy but also because the superconductor parameters, such as penetration depth λ and pinning strength which will change with temperature as well.

As one can see from Fig. 7.9, some of the curves have a magnitude of V_{dc} increasing until the switching point; others reach a maximum in $|V_{dc}|$, then turn around, implying that the vortex motion in the other direction of the ratchet is playing a larger role. In most cases, the Larkin-Ovchinnikov instability limits whether or not we can see the maximum in V_{dc}.

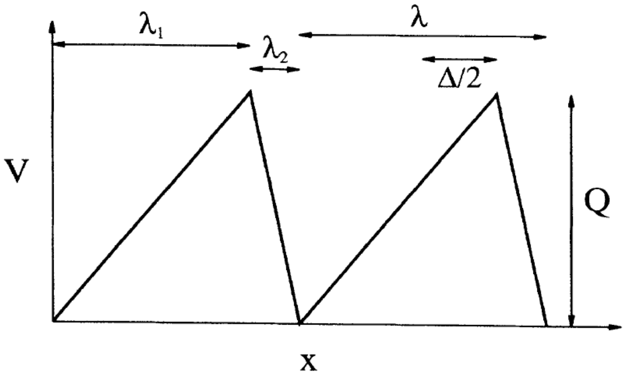

Figure 7.11: A schematic of the linear potential $V(x)$ as a function of position x from Magnasco [71]. The period of the potential is $\lambda = \lambda_1 + \lambda_2$ and the symmetry breaking amplitude is $\delta = \lambda_1 - \lambda_2$. (from Magnasco, 1993, p.1478)

For generic rocking-ratchet, as the driving force increases, particles tend to move toward the easy direction of the ratchet (toward the right in Fig. 7.11). With the driving amplitude increasing to larger values, some particles start to move toward the left of the ratchet causing ratchet effects to decrease(Fig. 7.11). Similar behavior can be found in the Ref. [71], where a rocking-ratchet with sawtooth potential had been studied numerically.

In general, V_{dc} is antisymmetric with H_a, thus indicating that the direction for net vortex motion corresponds to the same spatial direction through the ratchet channels. This means that when a negative field H_a is applied, the anti-vortices in the channels will move to the opposite direction, corresponding to vortices moving in the same spatial direction as if positive H_a had been applied. There are also substantial peaks in $|V_{dc}|$ visible on either side of $H_a = 0$; thus there is an H_a that optimizes the ratchet effect [Fig. 7.12]. For large H_a over the optimum field, $|V_{dc}|$ is diminished, although there is still a non-zero value for H_a considerably beyond the peak, up to 70 Oe.

For $H_a = 0$, $V_{dc} \approx 0$ for all I_{ac}, as there are no screening currents flowing along the channel walls in response to H_a. For $H_a \neq 0$ but still small, the sign of V_{dc} corresponds to the net motion of vortices in the hard direction, consistent with the reversal of the critical currents observed in the measurements of $I_c(H_a)$ [Fig. 7.6(a)]. There is an abrupt transition of V_{dc} to the expected sign for net vortex motion in the easy direction at $H_a \approx \pm 1$ Oe and this can be seen as vertical ridges in Fig. 7.8.

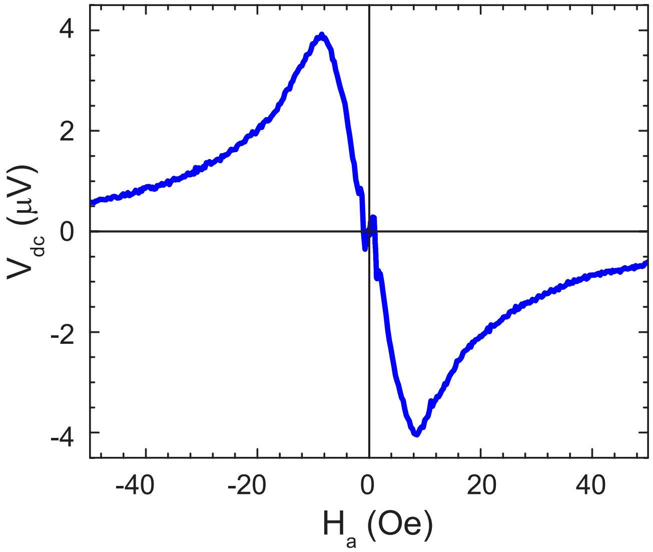

Figure 7.12: $V_{dc}(H_a)$ line cut at $I_{ac} = 2.1$ mA along the density plot in Fig. 7.8.

By comparing the line cuts of $V_{dc}(H_a)$ for a particular value of I_{ac} [Fig. 7.12] with the measurements of $I_c(H_a)$ [Fig. 7.6], we observe that the ridges in V_{dc} [Fig. 7.8] occur at approximately the same H_a as the crossing of the two senses of I_c [Fig. 7.6]. For a small H_a, below this crossover of the two senses of I_c, where no vortices are present in the channels for $I < I_c$, there are screening currents flowing along the channel walls due to the discontinuity in the thickness and penetration depth at each wall. These currents will be concentrated at the outer points of each ratchet cell and can effectively invert the sense of the ratchet potential defined by the shape of the channel walls [99], thus reversing the ratchet effect for the vortices that enter the channels when $I > I_c$ as shown in Fig. 7.13.

We also notice the value of H_a at which $|V_{dc}|$ reaches the maximum ($H_a = 8.6$ Oe) coincides with the approximate convergence of the two senses of current through the strip. Thus at this point, the arrangement of vortices minimizes the asymmetry in the static friction, as characterized by I_c, yet the overall ratchet response as captured

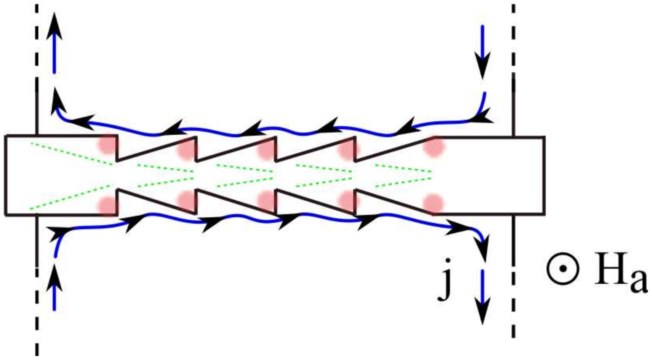

Figure 7.13: Schematic of Meissner screening currents flowing along the channel walls can invert the ratchet potential at the small field. The arrow line indicate the screening current flow in the vortex-free region; the pink dots present the field focus caused by the current flow near the corners of the ratchet channels; the dashed lines in the channel indicate the inverted potential.

by $|V_{dc}|$ is a maximum due to the substantial asymmetry in this regime between the dynamical sliding states for the two directions through the ratchet. The two branches of the IVC measured with a large I_{ac} [Fig. 7.10] exhibit a considerable difference in curvature and this dynamical asymmetry results in the significant ratchet response.

7.7 Magnetic hysteresis in ratchet channels

As discussed in Section 6.5, the vortex dynamics will become hysteretic when the applied field H_a is larger than the vortex entry field of NbN, H_s^{NbN}. In the measurement of the ratchet channels, we can clearly see magnetic hysteresis when we increase H_a to large values (Fig. 7.14). The sample parameters in Fig. 7.14 are: $W = 200$ μm, $s = 20$ μm and $p = 4.5$ μm, measured at temperature $T = 2.78$ K. Note that the strip width is 200 μm, and the vortex entry field ($H_s^{NbN} \sim 4$ Oe) whereas the entry field of a 50 μm-wide strip, $H_s^{NbN} \sim 8$ Oe. This variation of the first vortex entry field is consistent with what would be expected from Eq. 6.9, where H_s shows an inverse square root dependence on W, $H_s \propto W^{-0.5}$. When the strip width varies from 50 μm to 200 μm, the corresponding H_s changes from $\sim$ 8 Oe to $\sim$ 4 Oe.

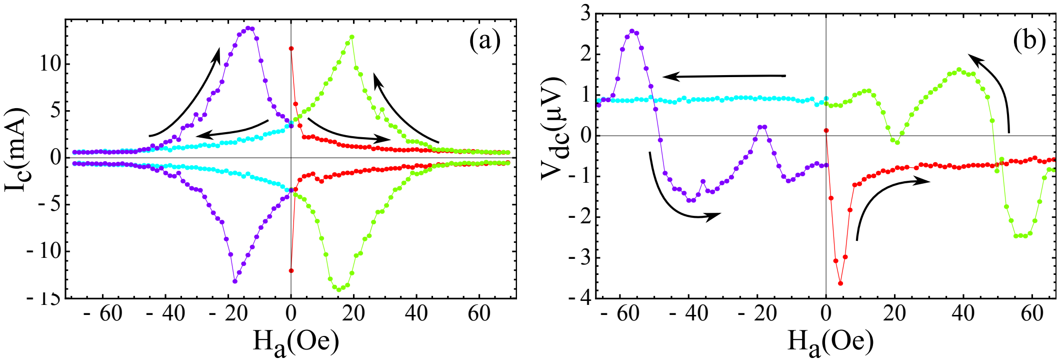

Figure 7.14: (a) Critical current as a function of the field while the field was ramped from zero to 67 Oe and back to zero, then ramped to −67 Oe without resetting the temperature, and finally back to zero, (b) a line-cut of ratchet signal V_{dc} as a function of the field for same measurement as (a). Sample parameters are: $w = 200$ μm, $s = 20$ μm, $p = 4.5$ μm and was measured at $T = 2.78$ K.

The hysteretic response of the critical current in Figure 7.14 is qualitatively similar to the one in the uniform channels (Fig. 6.17). However, the ratchet potential causes asymmetrical between the hard and the easy directions in the critical currents. This asymmetry can be seen in Figure 7.14.

We can see this ratchet magnetic hysteresis effect in a more dramatic form by a comparison of density plots for outgoing and return magnetic field sweeps. Figure 7.15 shows a ratchet response in a magnetic hysteresis measurement.

7.8 Conclusion

To summarize, I discussed the vortex dynamics in the periodic constricted weak-pinning channels in the last chapter, where we addressed the influence of the edge barrier in our system, the commensurability on $I_c(H_a)$ and magnetic hysteresis while vortices are present in strong-pinning NbN film.

In this chapter, we extended our study to a vortex ratchet. I have demonstrated a substantial ratchet effect for a system of vortices moving through weak-pinning channels with asymmetric walls. This ratchet exhibits considerable asymmetries in both the static and dynamic friction, with different dependences on H_a. The edge

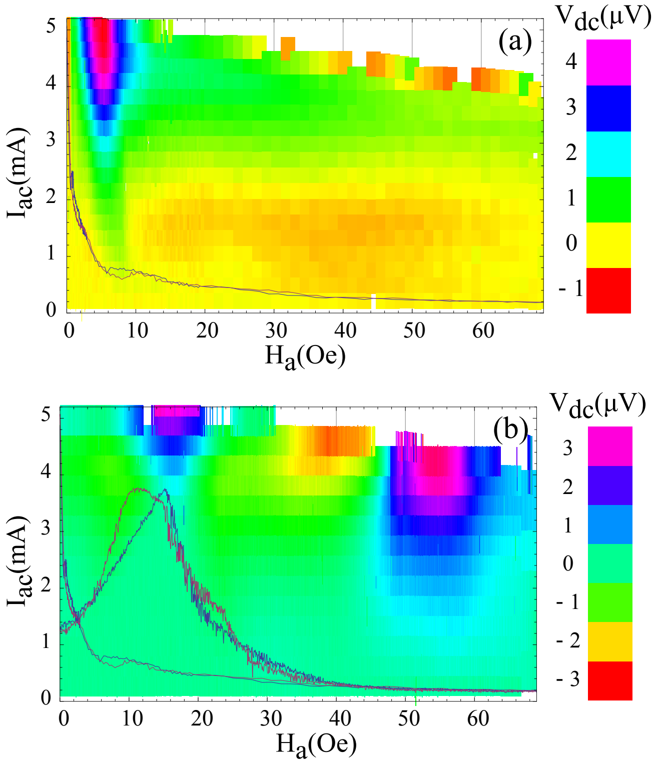

Figure 7.15: Density plot of a ratchet sample superimposed with critical current; (a) density plot while field is ramping up; (b) is measured when field reduces to zero. Sample parameters are: $p = 4.5\ \mu m$, $s = 20\ \mu m$ and $w = 50\ \mu m$.

barrier corresponding to the strip geometry of our structure plays an important role in the vortex dynamics, including delineating a low-field Meissner regime in the channels from a state corresponding to vortices occupying ratchet cells statically for $I < I_c$. However, asymmetries in the edge barriers alone as described in Ref. [106] cannot account for our ratchet effect, although this may be related to the smaller reverse ratchet response that we observed at the small H_a in the Meissner regime of the channels.

The microfabricated nature of our channels allows for future ratchet explorations with different channel wall shapes and configurations. I will discuss these different configurations as well as ratchet cells with smaller periodicity p in the subsequent chapters.

Chapter 8

Controlling confinement and interactions in weak-pinning vortex ratchet channels

8.1 Introduction

I have demonstrated an implementation of the vortex ratchet in asymmetric weak-pinning superconducting channels. These two-dimensional guides for vortices [112] allow us to provide a spatial asymmetry by tailoring the shape of the channel walls. The channels themselves had minimal pinning that could impede the motion of vortices. In Chapter 7, we observed a strong dependence of the ratchet response on the magnetic field, with a particular field resulting in the maximum rectification, where the vortices distributed in the ratchet channels optimized the asymmetric response [101].

By varying the channel geometry and configurations, our weak-pinning channels provide a ratchet system where we control the ratchet dynamics and particle interactions. In this chapter, I present a wider exploration of the parameter space for this weak-pinning channel ratchet system for devices with different channel spacings, ratchet cell shapes and temperatures. All of these parameters influence the nature as well as the magnetic field of the ratchet maximum. In addition, for certain parameter regimes, we find evidence of collective effects due to vortex interactions both within channels, leading to reversals of the direction for net vortex motion, and between vortices in neighboring channels. This results in an enhancement of the rectification strength near the ratchet maximum and influences the nature of the ratchet reversals. In the following sections we explore the ratchet response as we vary each of these parameters.

8.2 Channel spacing

In this section, we vary the spacing between channels, keep all other sample parameters fixed. Varying the channel spacing influences the interaction between vortices in neighboring channels when channel spacing (s) is in the range of the penetration depth of NbN ($\lambda_{\perp}^{NbN}$). We explore this commensurability by measuring identical strips containing identical ratchet channels, meaning there will be roughly the same amount of flux in the channels at the ratchet maximum field; this corresponds to a particular configuration of vortices in the ratchet cell. We have measured samples with different channel spacings covering a wide range – from $\sim 5\mu m$ to $\sim 250\mu m$.

In Figure 8.1, substantial peaks in $|V_{dc}|$ can be seen for each spacing, where the field corresponding to the ratchet maximum shifts to smaller field in larger spacing. The reducing of maximum I_{ac} with the increasing of the applied field is related to the Larkin-Ovchinnikov vortex core instability mechanism [14]. Compared to the density plot we discussed in Chapter 7 (Fig. 7.8), the ratchet V_{dc} in this chapter is positive, because the sample orientations were opposite. Therefore, the positive current drives the vortex motion along the easy direction of the ratchet channels, whereas the positive current drove the vortex motion along the hard direction in the previous chapter.

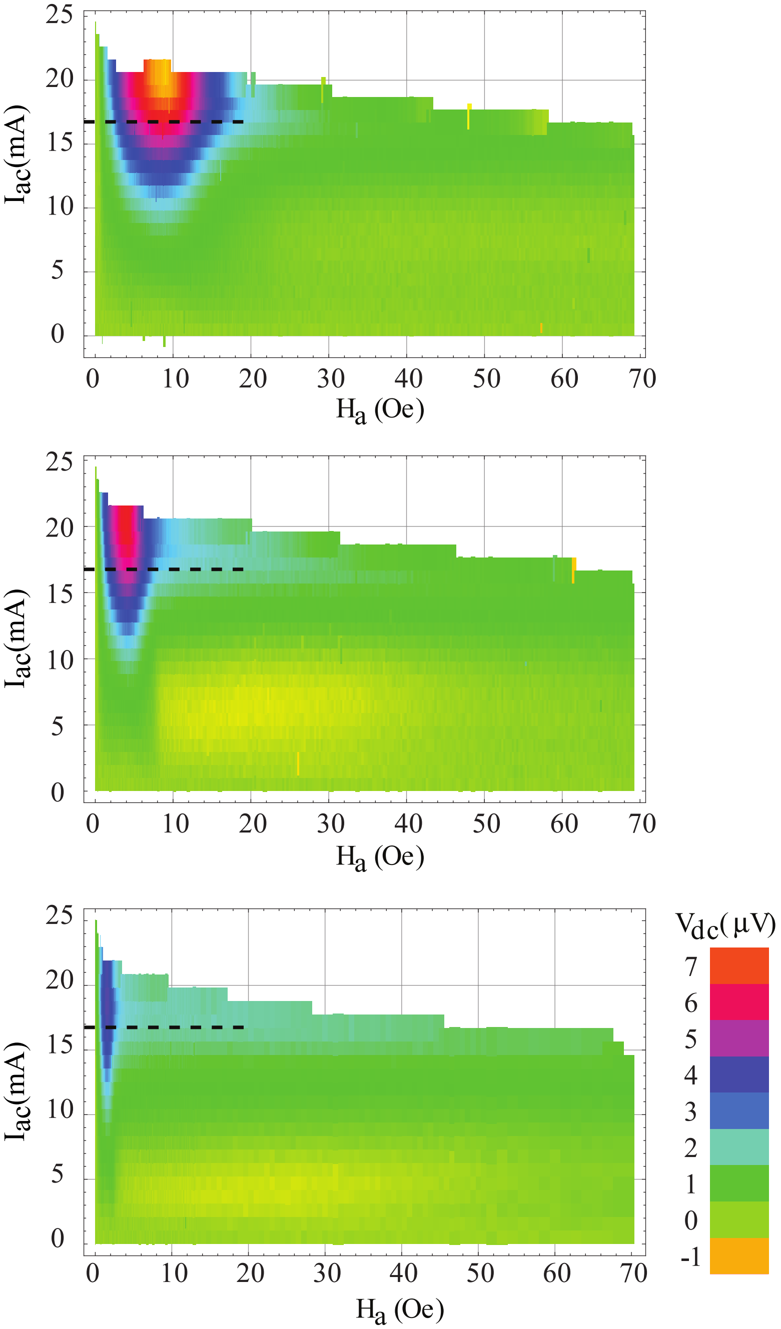

Figure 8.1: Density plots of samples with (a) 10 μm, (b) 20 μm and (c) 75 μm channel spacings, where $T = 2.78\ K$, $b = 1.5\ \mu m$ and $w = 200\ \mu m$.

Making line-cuts through the density plots at certain driving currents can resolve the overall structure of the ratchet response along the field axis (Fig. 8.2). The ratchet maximum moves to a larger field at the spacing. We extract the magnetic

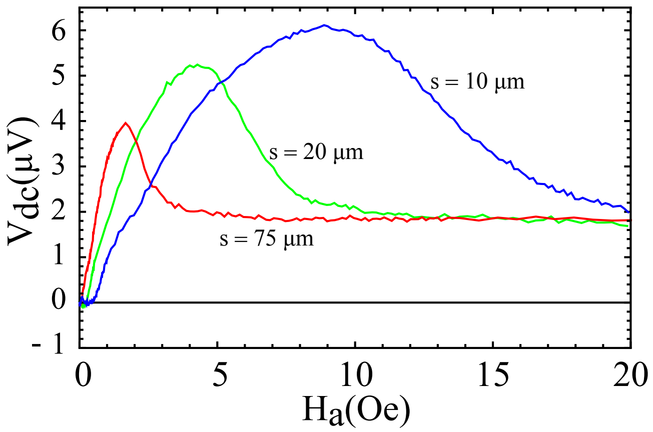

Figure 8.2: V_{dc} vs. H_a line-cuts of different channel spacings, s = 75, 20 and 10 μm from left to right respectively, where $T = 2.78$K , $b = 1.5$ μm, $w = 200$ μm and cutting amplitude I_{ac} as indicated in Figure 8.1 with dashed line is 80% of I_p, where I_p is the switching out current amplitudes at the corresponding ratchet peak fields.

field (H_p) at the ratchet maximum (V_p) and then plot $1/H_p$ as a function of the channel spacing, as shown in Figure 8.3. This demonstrates that a smaller spacing should require a larger applied field in order to result in a particular configuration of vortices in each ratchet cell. In contrast, if channels are far apart, a smaller applied field is needed to reach the same matching condition.

As I discussed previously, the flux density in the channel is primarily determined by the area occupied by the vortex. When the channel spacing is small ($s < \lambda_\perp^{NbN}$), vortices in adjacent channels will be highly overlapping, while along the channel, the relevant length for the flux is cell length p. The flux density required for adding one more vortex, therefore, is determined by $\Delta B \approx \Phi_0/s\ p$. We think the ratchet maximum should correspond to a particular vortex configuration, that is an integer number of vortices per ratchet cell. So the $1/H_p$ should vary linearly with s at small spacings, as one can see in Figure 8.3.

On the other hand, if channels are far apart ($s \gg \lambda_\perp^{NbN}$), the flux will extend $\sim \lambda_\perp^{NbN}$ into the banks on either side of the channels. Thus, the flux density required

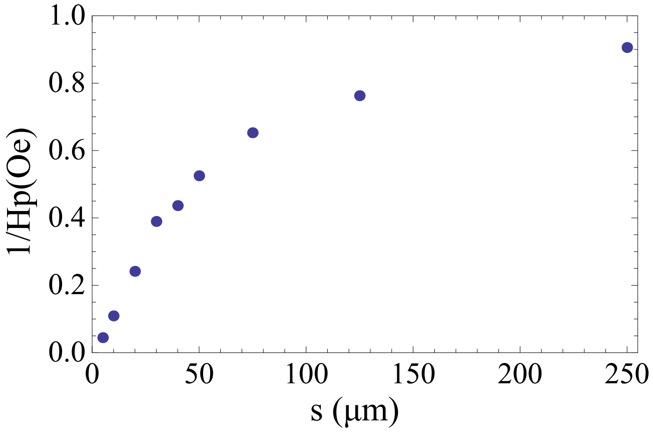

Figure 8.3: Plot of $1/H_p$ versus spacing showing $1/H_p$ varies linearly at the small spacing, but approaches to a constant at the large spacing.

for adding one vortex in the cell is $\Delta B \approx \Phi_0/2p\lambda_{\perp}^{NbN}$. This indicates that the $1/H_p$ should approach a constant at the large spacing (Fig. 8.3).

Intuitively, one would expect that below some threshold channel spacing, vortices in neighboring channels will be able to start interacting. While above this threshold, the vortices in one channel would be independent of vortices in the other channels. As one can see from Figure 8.2, in addition to the variation of the maximum peak field with a channel spacing, we observe an enhancement of the maximum ratchet signal (V_p) for small channel spacings (Fig. 8.4). This increase can be as large as nearly

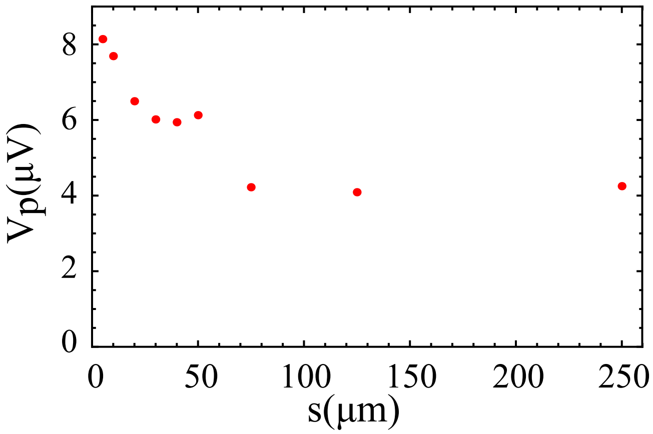

Figure 8.4: Maximum ratchet signal V_p varies with spacing s.

a factor of two. This is most likely due to the collective effects of the vortex inter-channel interactions. At the smaller spacing, where $s < \lambda_{\perp}^{NbN}$, vortices in neighboring channels may start to interact and form a crystallized arrangement, which enhances the ratchet effect [26, 96].

8.3 Ratchet cell shape

In this section, we fix the aperture size and the cell length, but we vary the width at the wide end of each triangular cell ("b" in Fig. 8.5). In addition to ratchet channels

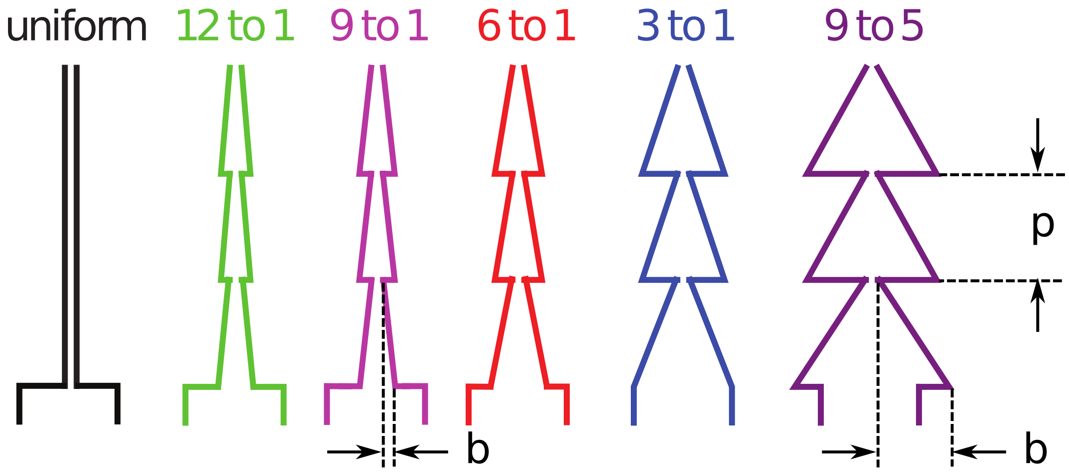

Figure 8.5: Schematic showing different taper shapes from left to right are uniform channel, where $b = 0.375$, 0.5, 0.75, 1.5 and 2.5 μm. These are only portions near one end of each of the channels.

with a taper of 3/1 (the ratio of p/b, where $p = 4.5$ μm.), we have other samples with tapers of 12/1, 9/1, 6/1, 9/5 and 1/1. The aperture sizes are the same for all of the samples, which is $\sim$ 700 nm. In this paper, we show data from the 12/1, 9/1, 6/1, 3/1 and 9/5 tapers. We observed ratchet effects as well as variations of the ratchet maximum field and different magnitudes of maximum rectifications. Of course, within the limit of zero-width at the back of the ratchet cell, the structure approaches a uniform channel; thus, any ratchet asymmetry vanishes.

Because vortex size is much larger than channel width, some fraction of vortex

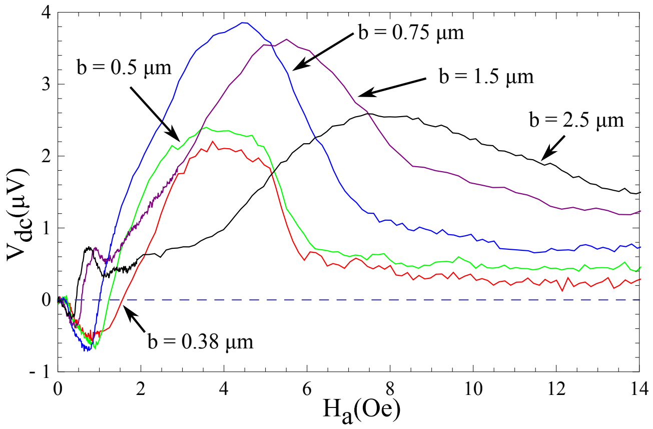

Figure 8.6: V_{dc} vs. H_a line-cuts through the ratchet peak of samples with different cell width. $s = 20$ μm, $T = 2.78$ K , $w = 50$ μm and the cutting amplitudes are $I_{ac} = 80\%$ I_p, where I_p is the switching out current amplitude at the corresponding ratchet peak field.

flux will spill into the NbN banks – which can be carried by the channel wall screening currents. Also, the penetration in the channels is much longer than in the banks, so when b increases, more of the vortex flux is in the channel and thus requires a larger B_{ch}. A larger fraction of vortex flux that resides in NbGe channel will therefore correspond to a larger matching field H_p. Figure 8.6 shows $V_{dc}(H_a)$ for different cell tapers.

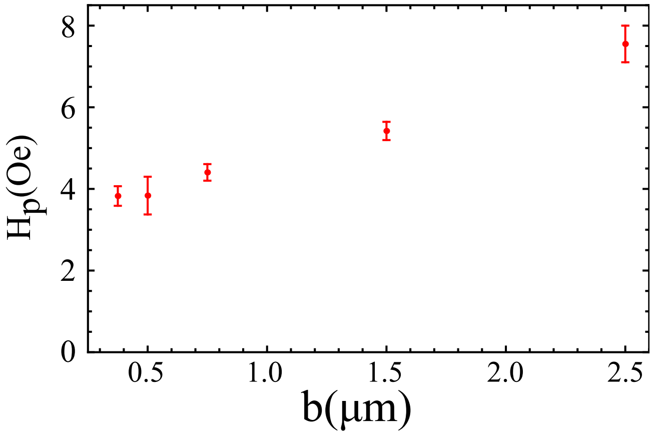

Figure 8.7: The field corresponds to the ratchet maximum plotted as a function of cell width.

As b increases, more and more flux is presented in the channel, and one needs larger field in order to reach the matching condition. We can plot this value as a function of b. Figure 8.7 shows the peak field position vs. the cell width.

We plot the line cuts through the V_{dc} peak of each ratchet sample together (Fig. 8.6). We see an optimum ratchet shape at a particular cell width. The 6/1 taper produces a larger ratchet signal than the other tapers as illustrated in Figure 8.9. When the cell width is zero, the ratchet cell will become a uniform channel, whereas at large cell width, the ratchet asymmetric potential will become less effective, vortices will experience comparable potential on both hard and easy directions. For the different tapers, the following applies: the easy direction gets easier for the shallower tapers – small b; the hard direction is more difficult to model, but it is likely that the enhanced barrier of the vortex motion persists even for small tapers, due to the abrupt step from the channel walls at the back of each ratchet cell. This is consistent with the critical current vs. the field plot (Fig. 8.8).

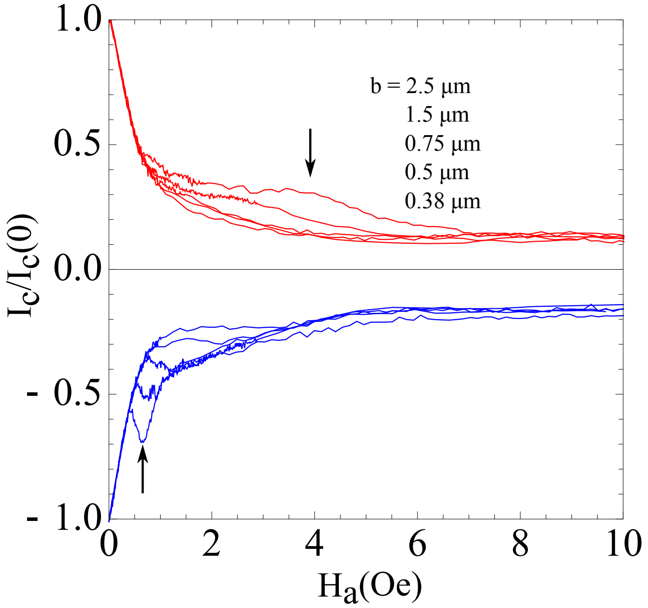

Figure 8.8: The critical current scaled by $I_c(0)$ as a function of the applied field for different cell tapers. Positive I_c corresponds to the vortex motion in the hard direction of the ratchet channel, whereas the negative I_c corresponds to the vortex motion in the easy direction. In this figure, b varies from 0.38 μm to 2.5 μm.

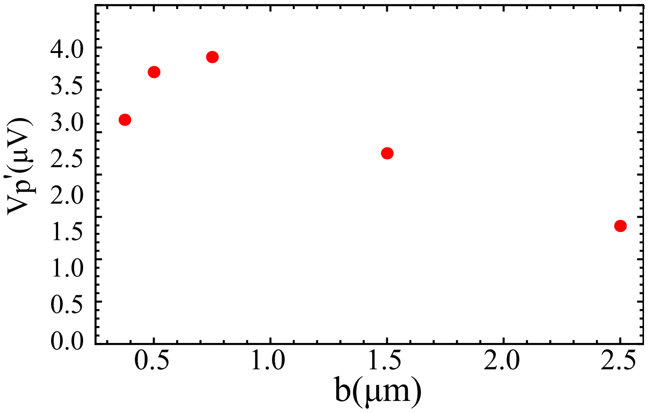

Figure 8.9: The maximum ratchet signal scaled by the flux flow resistance $V_p' = V_p/(R_r/R_u)$ varies with cell width b. Here R_r and R_u are normal resistance of ratchet and uniform samples.

And we see that the smaller critical current in the easy direction has the larger ratchet signal. We can also plot the ratchet maxima as a function of b, where an optimum taper 6/1 is showing the largest ratchet signal (Fig. 8.9). For purposes of comparison, the uniform channel critical current shows a symmetric behavior, which corresponds to zero dc-voltage. We also notice that the I_c+ and I_c- merge at the ratchet maximum, as we generally saw for other ratchet samples we have measured.

8.4 Temperature

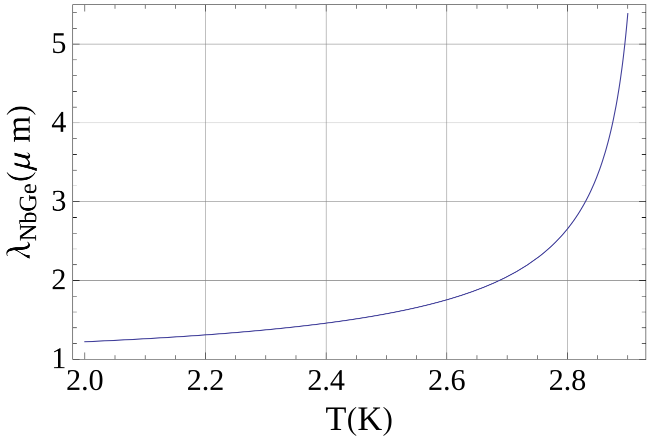

Figure 8.10: Calculation of penetration depth λ_{NbGe} *vs.* T.

We investigated the temperature dependence in our measurements. As temperature decreases, the NbGe penetration depth λ_{NbGe} becomes shorter (Fig. 8.10). In the temperature range of our measurement ($T \ll T_c^{NbN}$), $\lambda_\perp^{NbGe}$ varies much more than $\lambda_\perp^{NbN}$ does, where $\lambda_\perp^{NbN}$ is basically constant. The temperature range is limited by the superconducting transition temperature, namely T_c as well as the thermomagnetic instabilities at lower temperatures.

The maximum V_{dc} shifts to a higher value at a lower temperature. This is partly because we can go further out on the IVCs for lower T, whereas at higher temperatures, the Larkin-Ovchinnikov instability will limit the currents that one can apply.

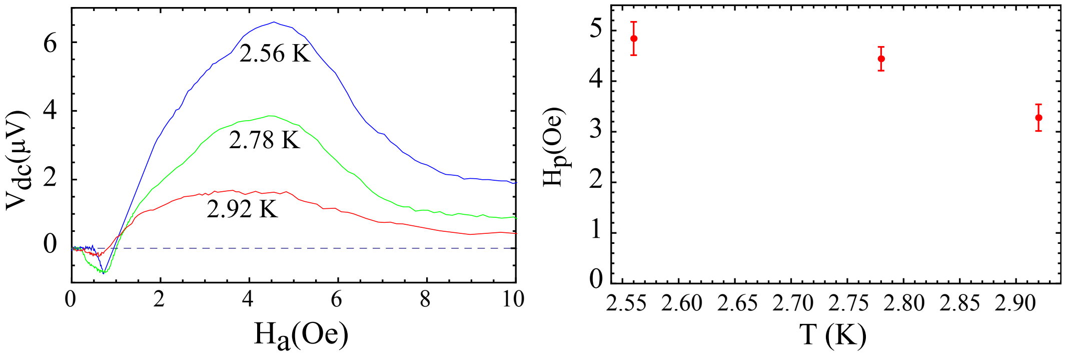

Figure 8.11: (a) V_{dc} vs. H_a line-cuts of different temperatures, where $s = 20\ \mu m$, $b = 0.75\ \mu m$, $w = 50\ \mu m$ and cutting amplitudes $I_{ac} = 80\%\ I_p$, where I_p is the switching out current amplitudes at the corresponding ratchet maximum. (b) The field corresponding to the ratchet maximum plotted as a function of temperature.

More vortex circulating currents come into the NbGe channels from the NbN bank while the $\lambda_\perp^{NbGe}$ becomes shorter. Therefore, the flux inside the channel is increased. At a lower temperature, in order to reach the same number of vortices as required for an optimum field at the ratchet maximum, one needs to increase the applied magnetic field. As we can see from Figure 8.11, the ratchet maximum shifts to larger fields at lower temperatures. Again, due to the nature of our channel structure, it is very difficult to have a detailed calculation of the flux density in the channel. One would need to carefully study the screening current on the strip as well as the interactions between the vortices and channel walls.

8.5 Ratchet reversals - results and discussion

For large channel spacings, in the limit of non-interacting channels for vortex densities beyond the ratchet maximum point, the ratchet response can reverse for low driving amplitudes as one can see from the yellow regions in Figure 8.1(b) and (c).

The occurrence of such ratchet reversals may depends on the configurations of vortex lattice at high vortex density, which can lead to inverted potential [97]. The relative importance of these different components depends on the particular vortex ratchet system being explored.

As shown in Figure 8.12, the reversal ratchet appears at spacings larger than 10μm. NbN thin-film penetration depth $\lambda_{\perp}^{NbN}$ at $T = 2.78$K is $\sim 8\mu$m. When the channel spacing becomes smaller than $\sim 8\mu m$, vortex-vortex inter-channel interaction is enhanced so that vortices in the channel will have a collection-effect and form a strong crystallized arrangement where they move collectively. We have measured the small spacings at $s = 10$ μm and $s = 5$ μm, and we did not observe any reversal effect. A line-cut at $I_{ac} = 5$ mA along the density plot of the 10 μm spacing data is shown in Figure 8.12(a).

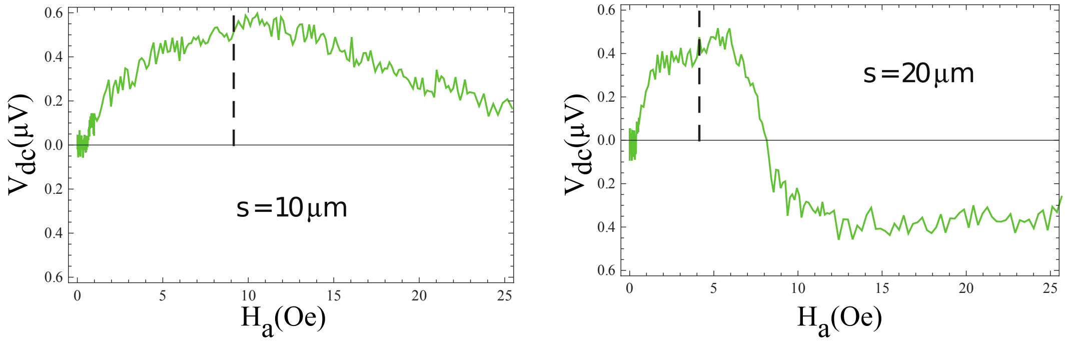

Figure 8.12: V_{dc} vs. H_a line-cuts for different channel spacings showing ratchet reversal.

At large I_{ac}, the Lorentz force would break the crystallized structure, thereby overcoming the inverted potential. This may eventually recovers the designed rectification direction. Vortices in the weak-pinning channel will start to move toward the easy direction of the ratchet, and the reversal ratchet effect disappears (Fig. 8.1).

We also studied such ratchet reversals for different cell shapes by changing the ratchet taper (Fig. 8.5). These are the same varying samples that we looked at earlier in this chapter. Within the range of our measurements, we do not observe a ratchet reversal at the smallest ($b = 0.375\ \mu m$) and larger ($b = 2.5$ and $4.5\ \mu m$) cells. When b is small, strong vortex density forces interaction among vortices within the channel. Therefore, a collective motion will prevent the disordering from occurring. For the larger ratchet cell, as vortices are far apart from each other, there will not be any trapped vortices that will revert the potential.

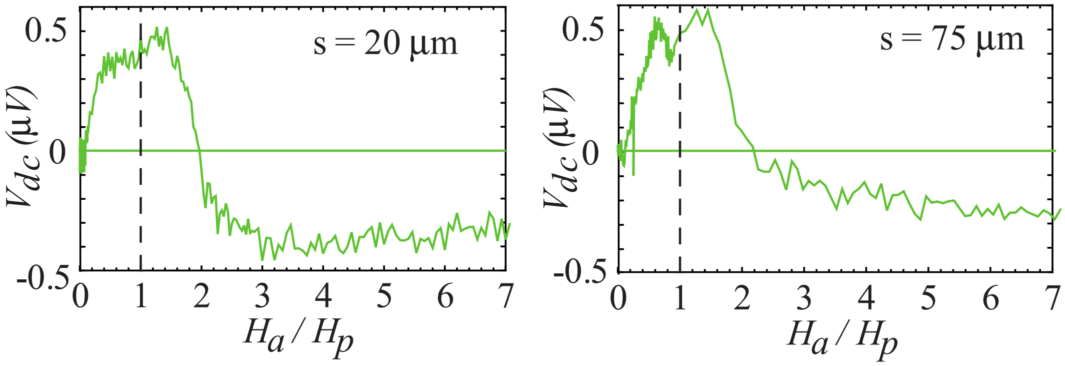

Figure 8.13: V_{dc} vs. H_a line-cuts for different channel spacings showing a ratchet reversal, where the field axes are normalized by the corresponding peak field H_p.

When H_a reaches the surface entry field of NbN, $H_a > H_s^{NbN}$, vortices will enter and become pinned in the strong pinning NbN bank. There might be undiscovered reasoning for the ratchet reversal in our system, but we are confident that the trapped vortices in the NbN bank do not contribute to the ratchet reversal effect. We have studied this effect in many different channel spacings. Based on our measurement results, the ratchet reversals always appear at fields larger than twice that of the main ratchet peak field $H_r \sim 2 \times H_p$ (Fig. 8.13 and 8.14). Although some of the fields are quite similar to the surface entry field of NbN in our system ($\sim 8\ Oe$), which is only determined by the strip width as we have discussed at Chapter 6, the fact that the position of the ratchet maximum is moving with the spacing indicates that the ratchet reversal onset field is changing while the width of the strip is kept

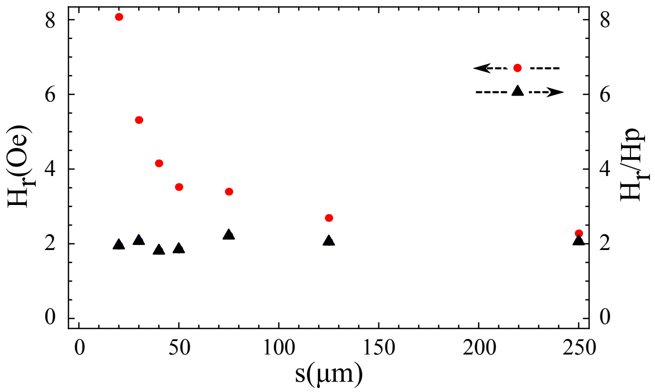

Figure 8.14: The *y-axes* are H_r(dots) and H_r/H_p(triangle), H_p is the field where the ratchet signal reaches the maximum, showing the reversal starting field is twice that of the main ratchet peak field.

constant, which means that the NbN surface entry field is kept constant.

8.6 Conclusion

In summary, we have demonstrated that we can control the ratchet dynamics by changing various ratchet parameters. In particular, we have designed our devices with different channel spacings and ratchet cell shapes. We measured those devices at multiple temperatures, which are well below the critical transition temperature of a-NbGe weak-pinning channel. During some parameter combinations of those measurements, we studied the contribution of the vortex collective effect on the ratchet response; a strong enhancement of the ratchet signal and a reversal of the ratchet potential appeared. The vortex dynamics is a combination of the vortex-vortex interaction and an interaction between the vortex and the interplay of ratchet potential shape and vortex lattice. With the ability to control these ratchet parameters, one can change the ratchet characteristics, fine tune the ratchet rectification strength and even select the direction of the ratchet potential. In the next chapter, I will explore the role of commensurability in the ratchet channels and the relation to the measurements of channels with diamond-shaped constrictions as presented earlier.

Chapter 9

Commensurability in weak-pinning ratchet channels with small cell sizes

9.1 Introduction

In Chapter 6, I discussed the vortex commensurability with vortices confined by periodic constrictions in our weak-pinning channels, where the channels were symmetric constrictions. We see a strong reversible critical current oscillation over the range of the applied magnetic field, which is influenced by the constriction period and channel spacing. We found clear evidence of magnetic hysteresis in the critical current when vortices become trapped in the strong-pinning NbN bank at the large field. In Chapter 7 and 8, we demonstrated substantial ratchet effects for a system of vortices moving through weak-pinning channels with asymmetric walls. Other than a strong rectification signal in the measured V_{dc}, multiple sharp features in the $I_c(H_a)$ curve had been observed, which appeared to be related to a matching effect although not as strong as the periodic constriction sample.

By reducing the cell length of the ratchet cell (p in Figure 9.1), we can see a strong

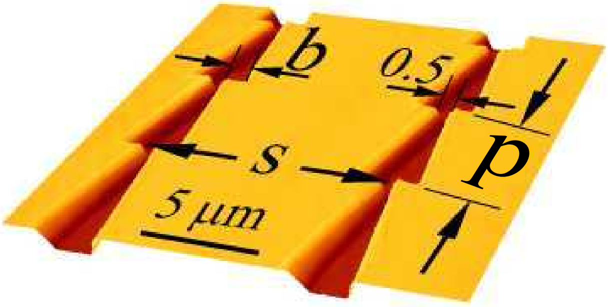

Figure 9.1: An atomic force microscopic image of ratchet channels with reduced cell size.

oscillation in the critical current as well as in the ratchet signal. In this chapter, I will present measurement results of matching effects on smaller cell sizes than those discussed in Chapter 8. For all of the samples discussed in this chapter, the half cell width $b = 1.5\ \mu m$ and were measured at a temperature of $T = 2.78\ K$.

9.2 Commensurability effects in ratchet channel measurements

In Chapter 7 and 8, I discussed ratchet channels with various parameters, including the half cell width b, channel spacing and measurement temperature. But within all the ratchet samples we covered so far, the cell length p was kept constant at $4.5\ \mu m$. We varied the cell length p for different ratchet channels. Within all the samples we have measured (cell length: $p = 1,\ 2,\ 3,\ 4.5,\ 6\ and\ 9\ \mu m$), regardless of the spacing and strip width, we only observe oscillations for $I_c(H_a)$ data at $p \leq 4.5\ \mu m$. But more significantly, the ratchet signal V_{dc} also exhibits a substantial matching effect (Fig. 9.2). The ratchet signal oscillations are most significant at a field range between zero and the ratchet maximum.

The fundamental oscillation period on the ratchet signal coincides with the oscillation period on the critical current as shown in Figure 9.2(b). It appears immediately

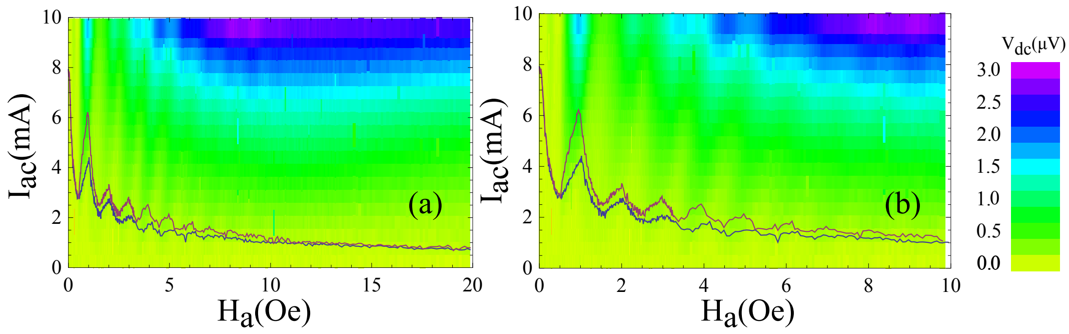

Figure 9.2: A ratchet rectification density plot of V_{dc} showing a ratchet signal with a strong oscillation at $p = 2$ μm. The color scale corresponds to the measured ratchet voltage V_{dc}. Corresponding $I_c(H_a)$ is superimposed. (b) same as (a) but only shows the field to 10 Oe.

after the driving current exceeds the critical current, where vortices start to flow in the channel dynamically.

Taking the Fourier transform on the $I_c(H_a)$ data as we have been doing for the diamond shape sample (Chapter 6), we can take the Fourier transform on the V_{dc} data with respect to H_a. The characteristic frequency of the ratchet signal oscillation can be better displayed using a density plot with the Fourier spectra at the corresponding driving current, as shown in Figure 9.3. The x-axis is the characteristic frequency of the ratchet data. The color scale ($|F(\omega_H)|$) corresponds to the Fourier transform of V_{dc}. A strong oscillation frequency at $\omega_H \sim 0.86$ Oe^{-1} can be identified in Figure 9.3.

In Figure 9.4, $I_c(H_a)$ curves of different cell periods p were plotted. The channel spacing $s = 20$ μm is the same for all four sets of data. For smaller p, the dominant peaks in the critical current shift to larger H_a.

The ratchet maximum field (H_p), where the ratchet rectification signal V_{dc} reaches the maximum value, can be identified from the corresponding density plot (Fig. 9.5) as we did for some of the earlier measurement results presented in Chapter 7 and 8. For a small cell length ratchet, it is difficult to extract the field position of an exact 'maximum point' as some of the ratchet maximum are very broad in field. A quantitative method in order to define H_p could be to take the field range that is

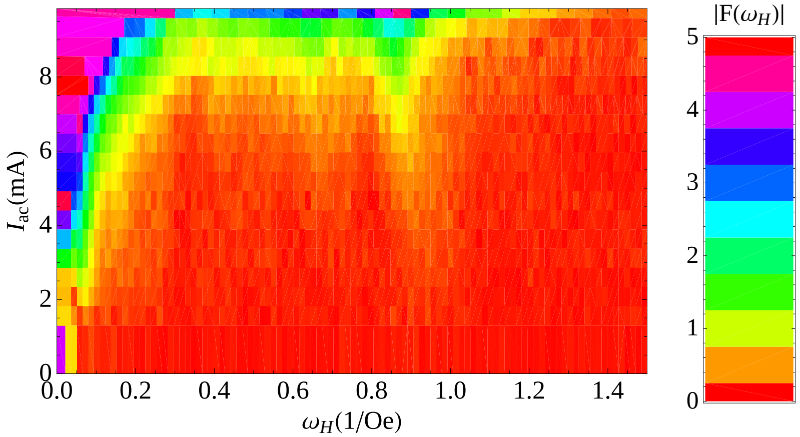

Figure 9.3: A density plot showing the characteristic frequency of ratchet oscillations, the color scale corresponding to the Fourier transform of V_{dc} for each field step.

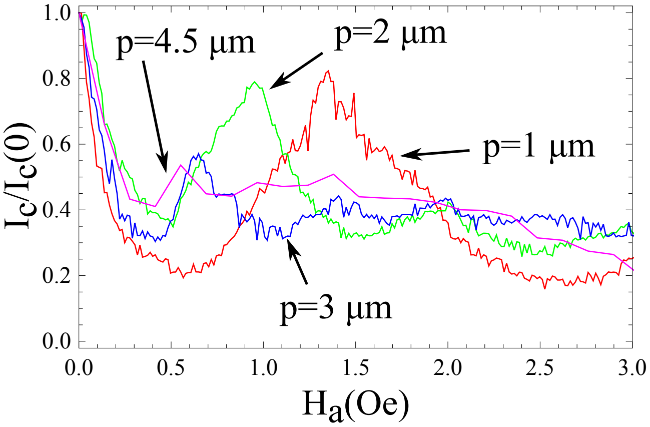

Figure 9.4: Normalized critical current (in the hard ratchet direction only; the easy direction also shows similar oscillations) as a function of the field showing the first oscillation peaks for samples with different cell periods.

covered by a $\sim 10\%$ drop of the V_{dc} from the 'maximum point' as the error bar for its corresponding H_p.

Although the oscillation magnitude gets smaller with longer cell length, Figure 9.6 shows that the Fourier transform of the $I_c(H_a)$ data provides a linear dependence of the characteristic frequency ω_H^0 on the cell length p. It behaves qualitatively in the same manner as the oscillations of the periodic pinning samples discussed in Chapter 6 [Fig. 6.13(a)]. As the inverse of H_p is shown in Figure 9.6(b), $1/H_p$ has a linear

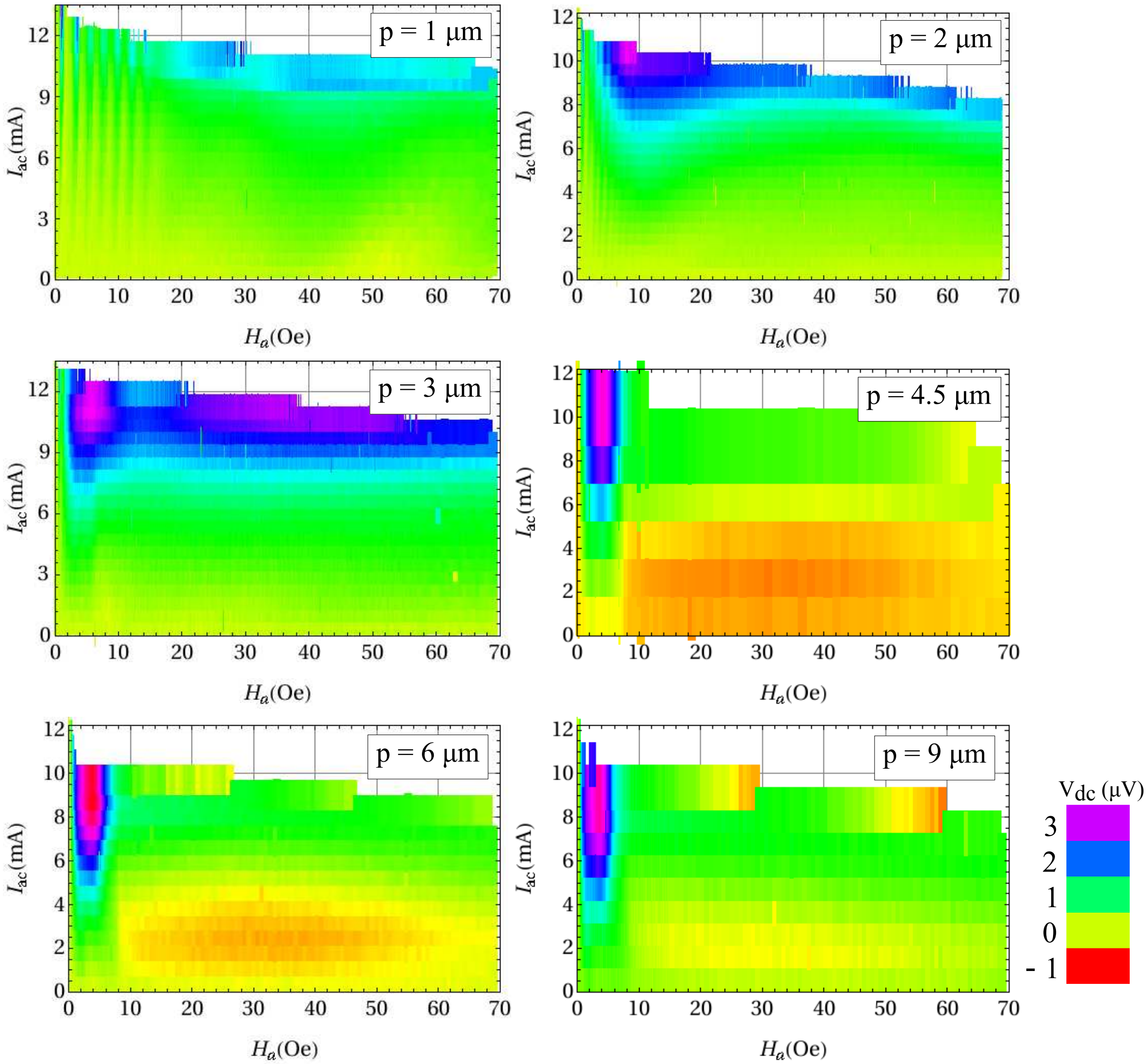

Figure 9.5: Density plots for different cell length p from $p = 1$ μm to $p = 9$ μm as they were labeled directly on each plot. [$s = 20$ μm, $b = 1.5$ μm, $W = 200$ μm and $T = 2.78$ K]

dependence on p. The data includes points where we cannot see any oscillation on the $I_c(H_a)$ curve, namely $p = 6$ and 9 μm. If H_p corresponds to a particular vortex configuration in the channel, it should have the same integer number of vortices per cell for different p. So we attempted to match Figure 9.6(a) with Figure 9.6(b). Surprisingly, both sets of data overlap very well with a scale factor of 13. Because the fields at the ratchet maxima are bigger than NbN entry field, some vortices are trapped in the NbN bank. The similarities by the linear p-dependence for $1/H_p$ and

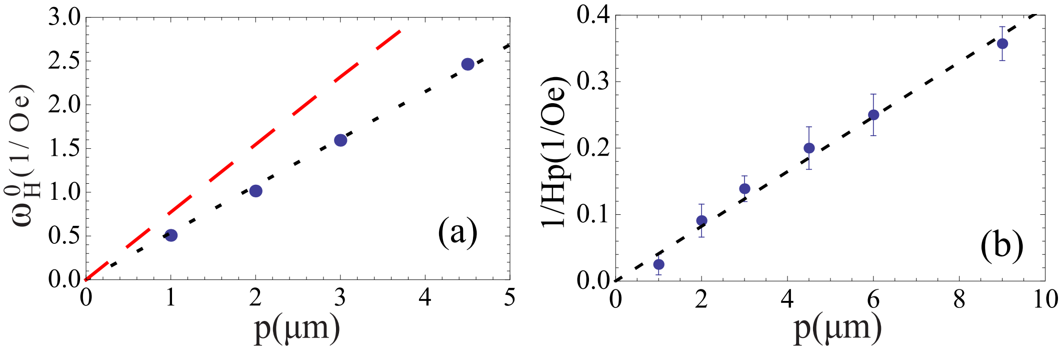

Figure 9.6: (a) The characteristic frequency of critical current oscillations ω_H^0, (b) $1/H_p$, where H_p is field corresponding to the ratchet maximum extracted from density plots, are plotted as functions of cell length p; dotted lines are for a guide to the eye; dashed lines have slope $2\lambda_\perp^{NbN}/\Phi_0$. [$w = 200$ μm, $s = 20$ μm].

ω_H^0 suggest that the V_{dc} maxima likely also correspond to optimum configurations with less than 13 vortices per ratchet cell.

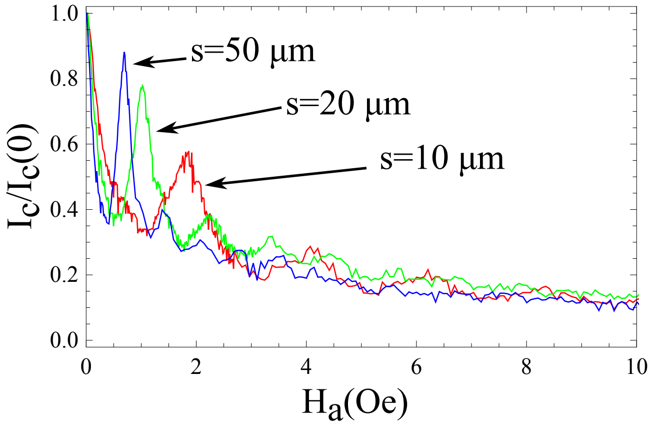

Figure 9.7: Normalized critical current (on the hard ratchet direction only; easy direction also shows similar oscillations) as a function of the field, showing the first oscillation peaks for samples with different a channel spacing.

With different channel spacing s, the dominant oscillation peaks move to the smaller field with a larger channel spacing (Fig. 9.7). Here the cell length $p = 2$ μm remains the same for all spacings.

We extracted the field that corresponded to the ratchet maximum, H_p, and plotted

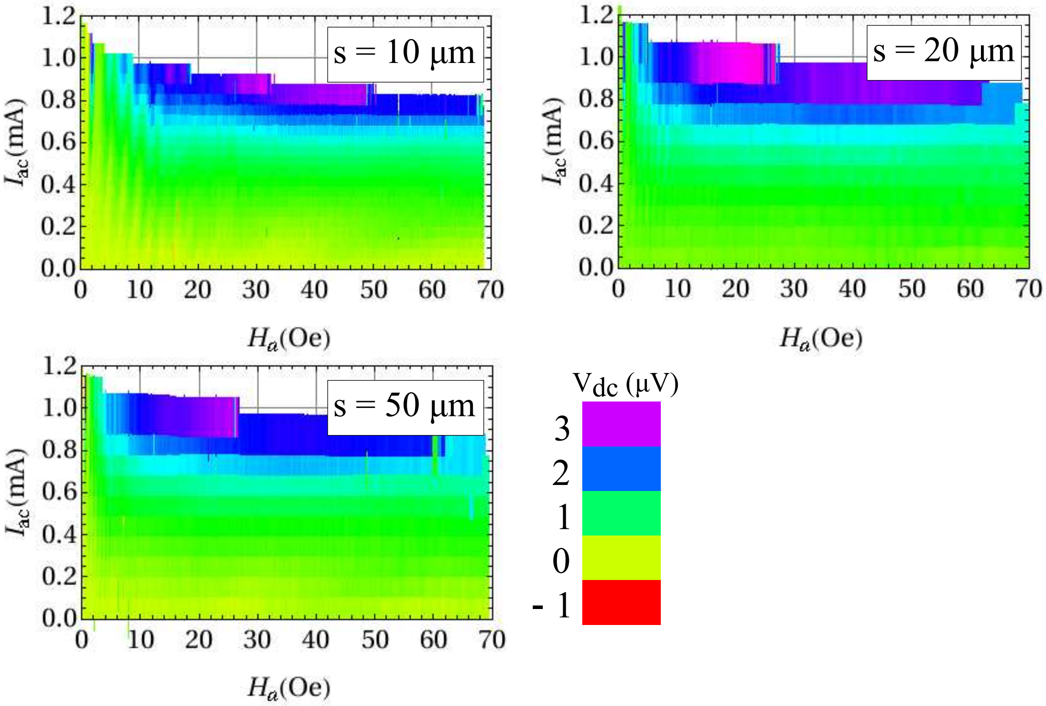

Figure 9.8: Density plots for different channel spacings s from $s = 10$ μm to $s = 50$ μm as they were labeled directly on each plot. [$p = 2$ μm, $b = 1.5$ μm, $W = 50$ μm and $T = 2.78$ K]

it as a function of s. Again, it is difficult to extract H_a from such broad main peaks on the V_{dc} density plot (Fig. 9.8). We utilized the same strategy in plotting the error bar as was used for the cell length data. As with the p-dependence, the inverse of H_p has a similar variation with s as ω_H^0 [Fig. 9.9(b)].

As shown in Figure 9.9(a), a Fourier transform applied to the data also indicates a similar trend as shown in Figure 6.13(b) in Chapter 6. At the smaller spacing, the field in the channel required to add one more vortex in each cell is $\sim \Phi_0/sp$. At the large spacing, so that the vortices in adjacent channels do not overlap, the flux density corresponding to the matching will become independent of s, approaching a constant $\sim \Phi_0/2p\lambda_\perp^{NbN}$.

During our measurements, we also found that the period, as well as the position of those oscillations, is independent of the temperature. The period is also independent of the NbGe thickness.

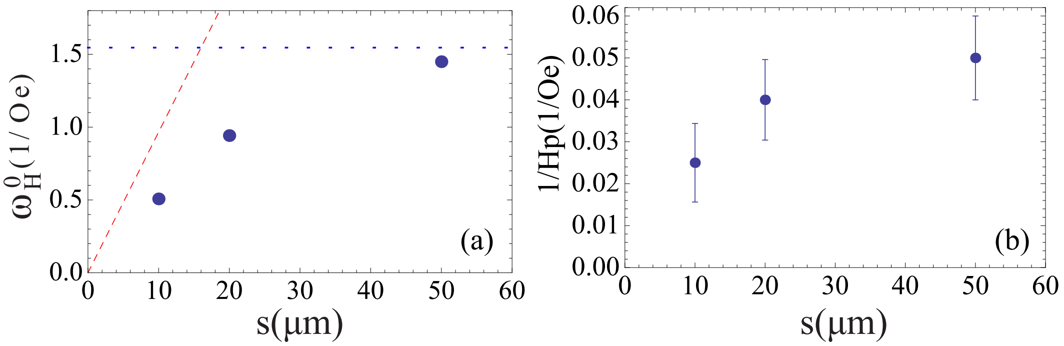

Figure 9.9: (a) The characteristic frequency of critical current oscillations and (b) $1/H_p$ are plotted as functions of the spacing; dashed line has a slope of p/Φ_0; horizontal dotted line corresponds to $2p\lambda_\perp^{NbN}/\Phi_0$. The strip width is $w = 50$ μm and $p = 2$ μm.

9.3 Conclusion and future work

The dynamics of vortices in confined superconductor geometries has generated much interest in recent years, with studies conducted of both fundamental properties of vortex matter as well as devices based on the motion of vortices. Nanoscale channels for guiding vortices through superconducting films with a minimal influence from pinning have been developed for exploring vortex melting [51], commensurability [48], mode locking [50], and ratchets [101]. These channels are typically arranged across the width of a superconducting strip, so that the vortices enter the channel at one edge of the strip and exit at the other edge, resulting in edge barriers to the vortex motion through the channels [102, 103, 105]. The strip geometry also allows for the use of multiple channel copies in parallel to boost the flux-flow signal strength for measurement with a room-temperature amplifier.

9.3.1 Future directions and challenges

It is possible to eliminate the edge barriers characteristic of a strip arrangement by using a Corbino geometry, consisting of a superconducting disk, with the current injected radially between the center and the perimeter. Vortices in such a disk experience an azimuthal Lorentz force and can flow in closed circular orbits without crossing any edges. The Corbino geometry has been used for many studies of vortex matter in different superconductors, including bulk crystals of $YBa_2Cu_3O_{7-\delta}$ [113] and $NbSe_2$ [114]. We have patterned thin-film Corbino disks with submicron circular channels for probing vortex dynamics in a narrow region free from edge barriers. Because the current density decreases radially in a Corbino geometry, such that vortices at different radii experience a different Lorentz force [115], we have designed our devices to only have a single channel. This poses a challenge for the amplifier used to detect the vortex motion. In this section, I present a scheme for driving a small number of vortices through a single, circular submicron channel and a picovoltmeter for resolving the ensuing flux-flow voltages.

Corbino channel fabrication

We fabricated our channels from bilayers of 200 nm-thick films of amorphous-NbGe, an extremely weak-pinning superconductor ($T_c^{NbGe} = 2.88$ K), and 50 nm-thick films of NbN with relatively strong pinning ($T_c^{NbN} = 9.6$ K), on a Si substrate. After patterning and etching a 1.5 mm-diameter Corbino disk into such a bilayer, we defined a 520 nm-wide channel in a circle with a 500 μm diameter using electron beam lithography (Fig. 9.10). We etched this region down to a depth of 120 nm using a reactive ion etch with CF_4, thus completely removing the NbN in this region and etching partially into the NbGe layer. In addition to the circular channel, we etched two radial channels (portals) that extend from opposite sides of the circular channel out to the edge of the Corbino disk. These portals allow for the introduction of vortices into the channel by field-cooling from temperatures $T_c^{NbGe} < T < T_c^{NbN}$, as they break up the circulating supercurrent in the outer NbN region.

We attach leads for driving the bias current I_b through the Corbino disk using 1.25 mil Al wirebonds, with 32 I_b^+ bonds around the perimeter of the disk. The I_b^- connection to the center consists of a superconducting Nb wirebond using annealed 2 mil Nb wire [Fig. 9.10(c)]. The azimuthal Lorentz force from I_b causes the vortices

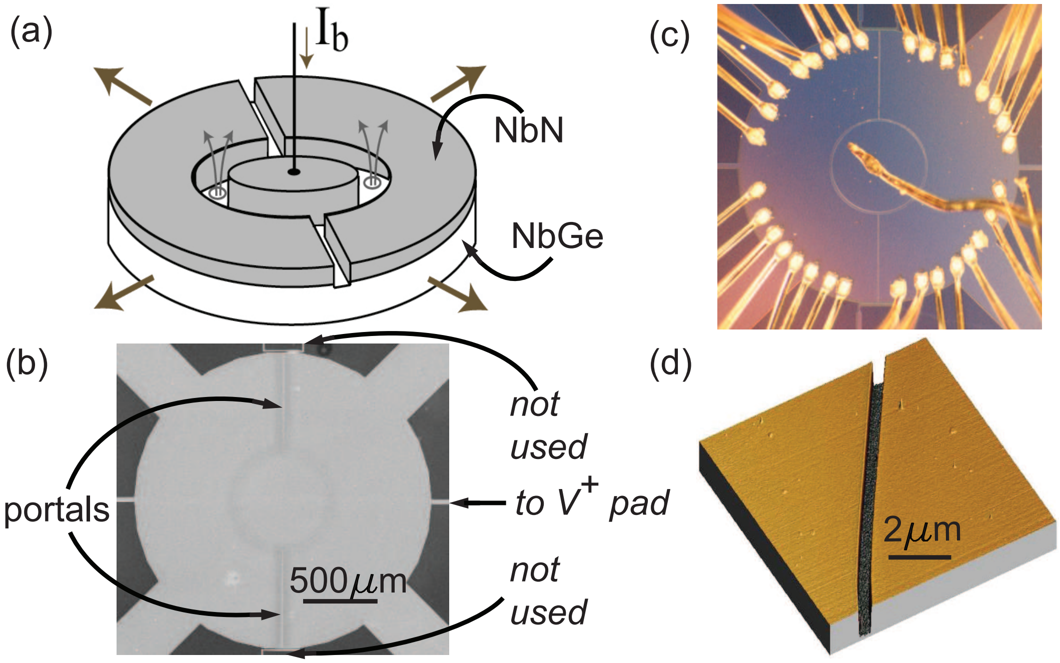

Figure 9.10: (a) Corbino channel schematic. (b) Scanning electron micrograph of Corbino disk; narrow lines at top and bottom not connected to disk. (c) Optical micrograph of disk showing wirebonds. (d) Atomic Force Microscope (AFM) image of channel.

to flow around the channel when this force exceeds the residual pinning in the NbGe channel. The ensuing vortex dynamics in the channel can be characterized by measuring the radial voltage drop across the channel, V_x, which is proportional to the vortex velocity and density.

Picovoltmeter design and characterization

The flux-flow voltage for vortices moving in a single channel at a low velocity can be relatively small. For example, vortices with a density corresponding to a magnetic induction of $B_{ch} = 1$ G in the channel moving at a velocity of 1 m/s, less than one percent of the typical Larkin-Ovchinnikov instability velocity for NbGe [14, 17], produce a flux-flow voltage of $\sim$ 50 pV. The measurement of such small signals would not be possible with a conventional low-noise room-temperature voltage amplifier with a noise floor of a few nV/Hz$^{1/2}$. In order to resolve these small flux-flow voltages, we have developed a voltmeter based on a Nb dc SQUID, which we obtained from ez SQUID. Sensitive voltmeters were one of the original applications of SQUIDs [116], and SQUID voltmeters have been used previously to probe the nature of the vortex state in bulk crystals of $YBa_2Cu_3O_7$ [117] and $Bi_2Sr_2CaCu_2O_{8+\delta}$ [118]. To the best of our knowledge, our scheme is the first application of a dc SQUID to form a picovoltmeter for resolving vortex dynamics in a patterned thin-film structure, as well as in a Corbino geometry.

We connected the voltage leads across the NbGe channel to the SQUID input coil with a resistor, R_{st}, consisting of a segment of brass foil (3.7 x 3.2 x 0.025 mm^3). This converted the flux-flow voltage to a current through the input coil, which has a self inductance L_i and a mutual inductance M_i to the SQUID [Fig. 9.11(a)]. Except for R_{st}, all of the voltage connections are superconducting. We made the voltage contacts on the Corbino disk with Nb wirebonds, where the V_x^- connection shares the superconducting Nb wire to the center of the Corbino disk with the I_b^- connection, while the V_x^+ Nb wirebond is attached to a pad of the NbGe/NbN bilayer that extends from the perimeter of the Corbino disk [Fig. 9.10(b)]. The other ends of these Nb wirebonds are attached to superconducting solder-tinned copper traces on our chip carrier using Pb washers. The V_x^+ connection is soldered to R_{st}, then the traces are attached to a twisted pair of 3 mil Nb wire with a second set of screw terminals using Pb washers. Finally, this Nb twisted pair is coupled to the input circuit on the SQUID holder with superconducting screw terminals.

We operated the SQUID in a conventional flux-locked loop, using a 4 MHz electronics system from ez SQUID, with the feedback signal V_{fb} supplied through a feedback resistor R_{fb} to a wire-wound coil with a mutual inductance M_{fb} to the SQUID. The SQUID holder is mounted in a Nb cylindrical shield that is closed on one end. The entire bottom end of the experimental insert is enclosed in a Pb cylindrical shield, and the dewar is surrounded by a μ-metal shield that is closed on the bottom.

A simple circuit analysis leads to the following expression relating V_{fb} to the

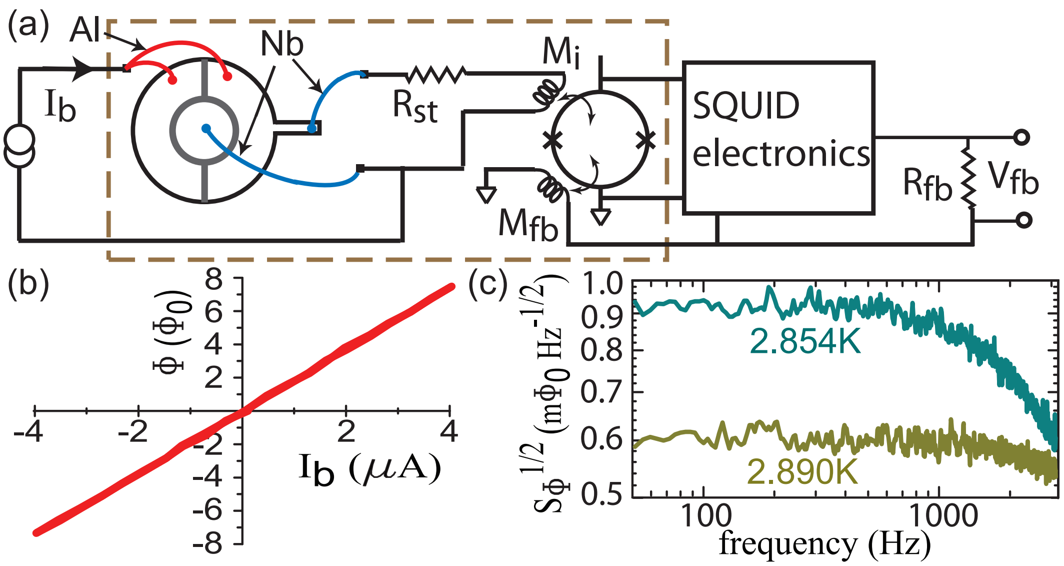

Figure 9.11: (a) Voltmeter circuit schematic; portions outside dashed box are at room temperature. (b) Flux coupled to SQUID vs. I_b at 4.2 K. (c) Flux noise spectra above and below T_c^{NbGe}, both measured with $I_b = 0$, $H_a = 0$.

voltage across the channel V_x:

$$V_{fb} = \left(\frac{R_{fb}}{R_{st}}\right)\left(\frac{M_i}{M_{fb}}\right) V_x. \tag{9.1}$$

The ratio R_{fb}/M_{fb} can be obtained in the usual way by measuring the difference in V_{fb} with the SQUID locked in adjacent wells (590 mV), and M_i was measured to be 6.6 nH through a separate calibration. We estimated R_{st} to be 2 mΩ based on the size of the brass foil, but we would be able to obtain a more careful calibration of the voltmeter gain through a series of low-temperature measurements.

We first measured the current-voltage characteristic of the Corbino channel at 4.2 K, where the NbGe channel is in the normal state, while the NbN banks are superconducting. Figure 9.11(b) shows the flux coupled to the SQUID plotted against the bias current I_b, which was monitored by tracking the voltage drop across a room-temperature current-sensing resistor. Because the channel is in the normal state, I_b divided between the channel, with resistance R_n, and the SQUID input coil with series resistance R_{st}. Based on 4.2 K measurements of similar NbGe channels of various geometries, we estimated R_n for this Corbino disk to be 3 mΩ.

The flux noise at $I_b = 0$ and zero field is essentially white with a high-frequency roll-off determined by L_i and the relevant resistance in the voltmeter circuit. By comparing the flux noise below this roll-off for temperatures above and below T_c^{NbGe}, we could obtain measurements of both R_{st} and R_n. Above T_c^{NbGe}, the flux noise is determined by the Nyquist noise current generated by $R_{st} + R_n$ flowing through M_i, while for $T < T_c^{NbGe}$, the only resistance is R_{st} [Fig. 9.11(c)]. In both cases the flux noise is more than an order of magnitude larger than the intrinsic flux noise for the SQUID, 10 $\mu\Phi_0/Hz^{1/2}$ at 100 Hz and 4.2 K from a separate measurement with the voltmeter circuit disconnected from the input coil. This analysis leads to $R_{st} = 1.9$ mΩ and $R_n = 2.6$ mΩ, consistent with our rough estimates. In addition, the location of the flux noise roll-off corresponds to $L_i = 110$ nH, consistent with the design of the input coil on this particular SQUID.

Applying our measured circuit and SQUID parameters with Eq. 9.1 yields a gain of 9.8×10^8. The measured flux noise at $T = 2.854$ K can be referred to as a voltage noise across the Corbino channel of 0.55 pV/Hz$^{1/2}$, more than three orders of magnitude lower than would be possible with the best conventional room-temperature voltage amplifier. Integrating over the 2.7 kHz bandwidth of the voltmeter yields an rms noise level of 25 pV. Of course, this noise could be reduced further, simply by using a smaller value of R_{st}, with a concomitant reduction in the measurement bandwidth. While a smaller R_{st} couples a larger flux noise to the SQUID by $R_{st}^{-1/2}$, the gain increases by R_{st}^{-1}, according to Eq. 9.1. Thus, the voltage noise referenced in the sample decreases like $R_{st}^{1/2}$.

Measurements of Flux-Flow in Corbino Channel with Picovoltmeter

We applied our voltmeter to measure the current-voltage characteristics (IVCs) of our single Corbino channel at $T = 2.874$ K for several cooling fields H_a. During our measurements, the Corbino disk and SQUID circuitry are immersed in a pumped helium bath. For each value of H_a, the insert was raised just above the bath and heated to 6 K, above T_c^{NbGe}, and was then cooled in H_a, generated with a superconducting coil. We recorded V_{fb} and I_b with a digital oscilloscope, taking 1024 averages per point for convenience on our particular oscilloscope. Fewer averages could be used, thus speeding up the acquisition while increasing the noise level on the acquired signal by $\mathrm{N}^{-1/2}$, where N is the number of averages.

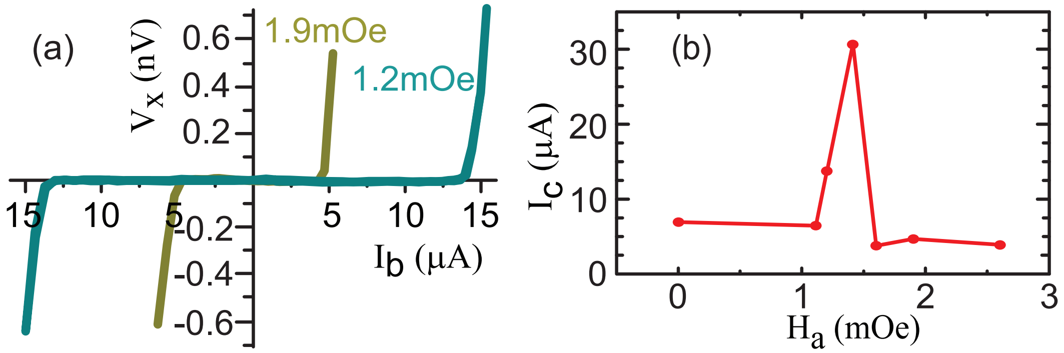

Figure 9.12: (a) IVCs for two different cooling fields at $T = 2.874$ K. (b) I_c for different H_a, extracted from IVCs.

The IVCs [Fig. 9.12(a)] exhibit a zero-voltage region at small I_b followed by an increasing flux-flow voltage for I_b beyond a depinning critical current I_c. Using a voltage criterion of 50 pV, we extract $I_c(H_a)$, which has a peak around 1.4 mOe. This peak points to zero absolute field, or to the limit of no vortices trapped in the channel. In contrast to a superconducting strip, which has a moderate critical current even in zero applied field corresponding to the entry of vortices and anti-vortices at the strip edges from the self-field of the strip [103, 105], the Corbino disk should have a large critical current when no vortices are present, as I_c in this case would correspond to the breakdown of superconductivity in the entire disk.

While the values of H_a in our measurements are relatively small, the intermediate field-cooling scheme generates substantial flux-focusing effects in the NbGe channel due to the superconducting NbN. A rough estimate, considering screening currents around the central disk of NbN inside the channel and along the outer NbN banks [105, 119], indicates the enhancement of B_{ch} may be of the order of 10 x H_a. Thus, cooling in an absolute applied field of 1 mOe should nucleate at least $\sim$ 10 vortices in the channel, where the effective area includes not only the channel, but the penetration of the vortex circulating currents into the NbN banks as well. A more detailed treatment of this flux focusing in the channels is beyond the scope of this paper.

Our measurements presented here have been performed close to T_c^{NbGe}, where the residual pinning in the channels was especially weak. This was necessary because of our wiring configuration, where the I_b^- lead was shared with the V_x^- connection to the center of the Corbino disk along a superconducting Nb wirebond. This Nb wirebond had a somewhat small critical current, thus requiring us to operate at temperatures where I_c was below the Nb wirebond critical current. In future Corbino measurements, it should be possible to separate these leads attached to the center of the disk, with the Nb wirebond used only for the SQUID input connection. The input connection does not need to sustain large currents because of the presence of R_{st}, with separate Al wirebonds for the I_b^- connection, which does not need to be superconducting.

9.3.2 Conclusion

We have studied vortex commensurability in the small ($p < 4.5$ μm) symmetric periodic constricted weak-pinning channels as discussed in Chapter 6, and we demonstrated the vortex ratchet effect in Chapter 7 and 8 on a relatively large cell length ($p = 4.5$ μm) with asymmetric weak-pinning channels. In this Chapter, we have shown the possibility of having a vortex ratchet rectification coexist with periodic oscillation in our system. Oscillations are mostly appearing at small constriction periods where $p \lesssim 4.5$ μm, and the oscillations show strong matching peaks before the main peak both on the critical current and the ratchet signal. Similar to the basic ratchet effect, there are asymmetries between the hard and easy directions of the critical current. Generally speaking, the larger critical current appeared in the hard direction at the field near the matching peaks. The responses of the oscillations have been compared between the small cell length ratchets and the periodic constricted diamond channels. The results show similar variations with both the cell length and the spacing. The characteristic frequency varies with the cell length linearly. It has a linear dependence on the small spacing, but it becomes independent of s when the channel spacing is large.

The possibility of probing the flux flow in a single channel and at low velocities by using the SQUID picovoltmeter is presented. This could be potentially useful for measuring single-particle dynamics in ratchet potentials.

Ratchet cells of all sizes that we measured show an asymmetric transport and a non-zero V_{dc}. We only see commensurability effects in the smaller ratchet cells, where confinement plays a stronger role. It is difficult to calculate the exact vortex distribution in the channel and eventually estimate the number of the vortices based on the applied field H_a. Without considering the screening effect or the interaction between vortices and the two different superconductors (NbN and NbGe), the estimate will not be able to reflect the true vortex distribution, not to mention the influence of the step from the channel to the NbN bank. All of those difficulties are caused by the nature of the channel geometry, the strip layout, as well as the edge barrier, factors which cannot be easily avoided.

Bibliography

[1] H. Kamerlingh Onnes, Leiden Comm. **120b, 122b, 124c** (1911).

[2] P. H. Kes, unpublished (2010).

[3] W. Meissner and R. Ochsenfeld, Naturwissenschaften (1933).

[4] F. London and H. London, Proc. Roy. Soc.(London) **A149**, 71 (1935).

[5] V. L. Ginzburg and L. D. Landau, Zh. Eksperim. i Teor. Fiz. **20**, 1064 (1950).

[6] M. Tinkham, *Introduction to superconductivity, 2nd edition* (Dover Pubns, 2004).

[7] A. A. Abrikosov, Zh. Eksperim. i Teor. Fiz. **32**, 1442 (1957).

[8] J. Bardeen, L. N. Cooper, and J. R. Schrieffer, Phys. Rev **108**, 1175 (1957).

[9] L. P. Gor'kov, Zh. Eksperim. i Teor. Fiz. **36**, 1918 (1959).

[10] P. H. Kes and C. Tsuei, Phys. Rev. B **28**, 5126 (1983).

[11] J. Bardeen and M. Stephen, Phys. Rev **140**, A1197 (1965).

[12] H. Suhl, Phys. Rev. Lett. **14**, 226229 (1965).

[13] Y. B. Kim, C. F. Hempstead, and A. R. Strnad, Phys. Rev. **139**, A1163 (1965).

[14] A. I. Larkin and Y. N. Ovchinnikov, Zh. Eksp. Teor. Fiz. **68**, 1915 (1975).

[15] S. G. Doettinger, R. P. Huebener, R. Gerdemann, A. Kühle, S. Anders, T. G. Träuble, and J. C. Villégier, Phys. Rev. Lett. **73**, 1691 (1994).

[16] W. Klein, R. P. Huebener, S. Gauss, and J. Parisi, J. of Low Temp. Phys. **61**, 413 (1985).

[17] D. Babić, J. Bentner, C. Sürgers, and C. Strunk, Phys. Rev. B **69**, 92510 (2004).

[18] A. I. Bezuglyj and V. A. Shklovskij, Physica C **202**, 234 (1992).

[19] G. S. Mkrtchyan and V. V. Shmidt, Zh. Eksp. Teor. Fiz. **61**, 367 (1971).

[20] J. Pearl, Appl. Phys. Lett. **5**, 6566 (1964).

[21] J. Pearl, Low Temp. Phys. **LT-9**, 566 (1965).

[22] M. Baert, V. V. Metlushko, R. Jonckheere, V. V. Moshchalkov, and Y. Bruynseraede, Phys. Rev. Lett. **74**, 3269 (1995).

[23] U. Welp, Z. L. Xiao, V. Novosad, and V. K. Vlasko-Vlasov, Phys. Rev. B **71**, 014505 (2005).

[24] M. Van Bael, J. Bekaert, K. Temst, L. Van Look, V. Moshchalkov, Y. Bruynseraede, G. Howells, A. Grigorenko, S. Bending, and G. Borghs, Phys. Rev. Lett.s **86**, 155 (2001).

[25] C. Reichhardt, G. Zimányi, and N. Gronbech-Jensen, Phys. Rev. B **64**, 014501 (2001).

[26] B. L. T. Plourde, IEEE Trans. Appl. Supercon. **19**, 3698 (2009).

[27] V. V. Moshchalkov, M. Baert, V. V. Metlushko, E. Rosseel, M. J. Van Bael, K. Temst, Y. Bruynseraede, and R. Jonckheere, Phys. Rev. B **57**, 3615 (1998).

[28] L. Van Look, B. Y. Zhu, R. Jonckheere, B. R. Zhao, Z. X. Zhao, and V. V. Moshchalkov, Phys. Rev. B **66**, 214511 (2002).

[29] U. Patel, Z. Xiao, J. Hua, T. Xu, D. Rosenmann, V. Novosad, J. Pearson, U. Welp, W. Kwok, and G. Crabtree, Phys. Rev. B **76**, 020508 (2007).

[30] C. Meingast, P. Lee, and D. Larbalestier, Journal of Applied Physics **66**, 5962 (1989).

[31] K. Harada, O. Kamimura, H. Kasai, T. Matsuda, A. Tonomura, and V. Moshchalkov, Science **274**, 1167 (1996).

[32] J. I. Martín, M. Velez, J. Nogues, and I. K. Schuller, Phys. Rev. Lett. **79**, 1929 (1997).

[33] M. J. Van Bael, K. Temst, V. V. Moshchalkov, and Y. Bruynseraede, Phys. Rev. B **59**, 14674 (1999).

[34] O. Geoffroy, D. Givord, Y. Otani, B. Pannetier, and F. Ossart, Journal of Magnetism and Magnetic Materials **121**, 223 (1993).

[35] D. Morgan and J. Ketterson, Phys. Rev. Lett.s **80**, 3614 (1998).

[36] V. R. Misko, S. Savel'ev, and F. Nori, Phys. Rev. B **74**, 024522 (2006).

[37] V. Misko, S. Savelev, and F. Nori, Phys. Rev. Lett.s **95**, 177007 (2005).

[38] J. E. Villegas, M. I. Montero, C.-P. Li, and I. K. Schuller, Phys. Rev. Lett. **97**, 027002 (2006).

[39] R. B. G. Kramer, A. V. Silhanek, J. V. de Vondel, B. Raes, and V. V. Moshchalkov, Phys. Rev. Lett. **103**, 67007 (2009).

[40] M. Kemmler, C. Gürlich, A. Sterck, H. Pöhler, M. Neuhaus, M. Siegel, R. Kleiner, and D. Koelle, Phys. Rev. Lett. **97**, 147003 (2006).

[41] C. Reichhardt, Phys. Rev. B **76**, 094512 (2007).

[42] M. Kemmler, D. Bothner, K. Ilin, M. Siegel, R. Kleiner, and D. Koelle, Phys. Rev. B **79**, 184509 (2009).

[43] J. Gutierrez, A. V. Silhanek, J. Van de Vondel, W. Gillijns, and V. V. Moshchalkov, Phys. Rev. B **80**, 140514(R) (2009).

[44] C. Reichhardt, J. Groth, C. J. Olson, S. B. Field, and F. Nori, Phys. Rev. B **54**, 16108 (1996).

[45] C. Reichhardt, C. J. Olson, and F. Nori, Phys. Rev. Lett. **78**, 2648 (1997).

[46] C. Reichhardt, C. Olson, and F. Nori, Phys. Rev. B **58**, 6534 (1998).

[47] E. V. Drift, S. Radelaar, A. Pruymboom, and P. Kes, Microelectronic Engineering **6**, 181 (1987).

[48] A. Pruymboom, P. H. Kes, E. van der Drift, and S. Radelaar, Phys. Rev. Lett. **60**, 1430 (1988).

[49] A. Pruymboom, P. Kes, E. van der Drift, and S. Radelaar, Applied Physics Letters **52**, 662 (1988).

[50] N. Kokubo, R. Besseling, V. M. Vinokur, and P. H. Kes, Phys. Rev. Lett. **88**, 247004 (2002).

[51] R. Besseling, N. Kokubo, and P. H. Kes, Phys. Rev. Lett. **91**, 177002 (2003).

[52] E. Brandt, Phys. Status Solidi B **77**, 551 (1976).

[53] B. L. Walton, B. Rosenblum, and F. Bridges, Phys. Rev. Lett. **32**, 1047 (1974).

[54] A. Troyanovski, J. Aarts, and P. Kes, nature **399**, 665 (1999).

[55] P. Hänggi and F. Marchesoni, Reviews of Modern Physics **81**, 387 (2009).

[56] P. Reimann, Physics Reports **361**, 57265 (2002).

[57] P. Hanggi and F. Marchesoni, Rev. Mod. Phys. **81**, 387 (2008).

[58] R. D. Astumian and P. Hänggi, Phys. Today **55**, 33 (2002).

[59] F. Jülicher, A. Ajdari, and J. Prost, Rev. Mod. Phys. **69**, 12691282 (1997).

[60] R. D. Astumian, Science **276**, 917 (1997).

[61] Y. Hiratsuka, T. Tada, K. Oiwa, T. Kanayama, and T. Uyeda, Biophysical Journal **81**, 1555 (2001).

[62] E. Kay, D. Leigh, and F. Zerbetto, Angewandte Chemie-International Edition **46**, 72193 (2007).

[63] T. Omabegho, R. Sha, and N. Seeman, Science **324**, 67 (2009).

[64] H. Linke, Phys. Lett **74**, 2194 (1999).

[65] D. E. Shalóm and H. Pastoriza, Phys. Rev. Lett. **94**, 177001 (2005).

[66] S. Matthias and F. Müller, Nature **424**, 5357 (2003).

[67] J. V. de Vondel, C. C. de Souza Silva, B. Y. Zhu, M. Morelle, and V. V. Moshchalkov, Phys. Rev. Lett. **94**, 057003 (2005).

[68] Y. Togawa, K. Harada, T. Akashi, H. Kasai, T. Matsuda, F. Nori, A. Maeda, and A. Tonomura, Phys. Rev. Lett. **95**, 87002 (2005).

[69] J. E. Villegas, E. M. Gonzalez, M. I. Montero, I. Schuller, and J. L. Vicent, Phys. Rev. B **68**, 224504 (2003).

[70] C. C. de Souza Silva, A. V. Silhanek, J. Van de Vondel, W. Gillijns, V. Metlushko, B. Ilic, and V. V. Moshchalkov, Phys. Rev. Lett. **98**, 117005 (2007).

[71] M. Magnasco, Phys. Rev. Lett. **71**, 1477 (1993).

[72] J. Clarke, *Superconducting Devices (eds Ruggiero, S. T. Rudman, D. A.)* (Academic Pr, 1990).

[73] C. Lee, B. Janko, I. Derenyi, and A. Barabasi, Nature **400**, 337 (1999).

[74] D. Morrison and R. Rose, Phys. Rev. Lett. **25**, 356359 (1970).

[75] B. Y. Zhu, F. Marchesoni, V. V. Moshchalkov, and F. Nori, Phys. Rev. B **68**, 014514 (2003).

[76] J. Van de Vondel, C. C. de Souza Silva, B. Y. Zhu, M. Morelle, and V. V. Moshchalkov, Phys. Rev. Lett. **94**, 057003 (2005).

[77] C. C. de Souza Silva, J. Van de Vondel, B. Y. Zhu, M. Morelle, and V. V. Moshchalkov, Phys. Rev. B **73**, 014507 (2006).

[78] R. Bartussek, P. Hanggi, and J. G. Kissner, Euro. Phys. Lett. **28**, 459464 (1994).

[79] R. Wördenweber, P. Dymashevski, and V. R. Misko, Phys. Rev. B **69**, 184504 (2004).

[80] A. Crisan, A. Pross, D. Cole, S. J. Bending, R. Wördenweber, P. Lahl, and E. Brandt, Phys. Rev. B **71**, 144504 (2005).

[81] W. K. Kwok, R. J. Olsson, G. Karapetrov, U. Welp, V. Vlasko-Vlasov, K. Kadowaki, and G. W. Crabtree, Physica C **382**, 137 (2002).

[82] C. J. Olson, C. Reichhardt, B. Janko, and F. Nori, Phys. Rev. Lett. **87**, 177002 (2001).

[83] B. Y. Zhu, F. Marchesoni, and F. Nori, Phys. Rev. Lett. **92**, 180602 (2004).

[84] A. Harada, J. Li, and M. Kamachi, Nature **356**, 325 (1992).

[85] J. I. Martín, M. Vélez, A. Hoffmann, I. K. Schuller, and J. L. Vicent, Phys. Rev. B **62**, 9110 (2000).

[86] J. E. Villegas, E. M. Gonzalez, M. P. Gonzalez, J. V. Anguita, and J. L. Vicent, Phys. Rev. B **71**, 24519 (2005).

[87] A. V. Silhanek, W. Gillijns, V. V. Moshchalkov, V. Metlushko, F. Gozzini, B. Ilic, W. Uhlig, and J. Unguris, Appl. Phys. Lett. **90**, 182501 (2007).

[88] G. Carneiro, Phys. Rev. B **72**, 144514 (2005).

[89] I. Derenyi and T. Vicsek, Phys. Rev. Lett. **75**, 374377 (1995).

[90] S. Savel'ev, F. Marchesoni, and F. Nori, Phys. Rev. Lett. **91**, 10601 (2003).

[91] S. Savel'ev, F. Marchesoni, and F. Nori, Phys. Rev. Lett. **92**, 160602 (2004).

[92] S. Savel'ev, F. Marchesoni, and F. Nori, Phys. Rev. E **70**, 061107 (2004).

[93] S. Savel'ev, V. R. Misko, F. Marchesoni, and F. Nori, Phys. Rev. B **71**, 214303 (2005).

[94] S. Savelev and F. Nori, Chaos **15**, 026112 (2005).

[95] J. E. Villegas, S. Savel'ev, F. Nori, E. M. Gonzalez, J. V. Anguita, R. García, and J. L. Vicent, Science **302**, 1188 (2003).

[96] C. C. de Souza Silva, J. V. D. Vondel, M. Morelle, and V. V. Moshchalkov, Nature **440**, 651 (2006).

[97] Q. Lu and C. Reichhardt, Phys. Rev. B **75**, 54502 (2007).

[98] W. Gillijns, A. V. Silhanek, V. V. Moshchalkov, and C. Reichhardt, Phys. Rev. Lett. **99**, 247002 (2007).

[99] N. Kokubo, T. G. Sorop, R. Besseling, and P. H. Kes, Phys. Rev. B **73**, 224514 (2006).

[100] P. Horowitz and W. Hill, *The art of electronics, 2nd edition* (Cambridge University press, 1999).

[101] K. Yu, T. W. Heitmann, C. Song, M. P. DeFeo, B. L. T. Plourde, M. B. S. Hesselberth, and P. H. Kes, Phys. Rev. B **76**, 220507(R) (2007).

[102] B. L. T. Plourde, D. J. Van Harlingen, D. Y. Vodolazov, R. Besseling, M. B. S. Hesselberth, and P. H. Kes, Phys. Rev. B **64**, 014503 (2001).

[103] M. Benkraouda and J. R. Clem, Phys. Rev. B **58**, 15103 (1998).

[104] M. Benkraouda and J. R. Clem, Phys. Rev. B **53**, 5716 (1996).

[105] D. Y. Vodolazov and I. L. Maksimov, Physica C **349**, 125 (2000).

[106] D. Y. Vodolazov and F. M. Peeters, Phys. Rev. B **72**, 172508 (2005).

[107] G. S. Mkrtchyan and Others, Zh. Eksp. Teor. Fiz. **63**, 667 (1972).

[108] V. Metlushko, U. Welp, G. W. Crabtree, R. Osgood, S. D. Bader, L. E. DeLong, Z. Zhang, S. R. J. Brueck, B. Ilic, K. Chung, et al., Phys. Rev. B **60**, R12585 (1999).

[109] M. Köppl, P. Henseler, A. Erbe, P. Nielaba, and P. Leiderer, Phys. Rev. Lett. **97**, 208302 (2006).

[110] V. J. Goldman, M. Santos, M. Shayegan, and J. E. Cunningham, Phys. Rev. Lett. **65**, 2189 (1990).

[111] G. Piacente and F. M. Peeters, Phys. Rev. B **72**, 205208 (2005).

[112] J. F. Wambaugh, C. Reichhardt, C. J. Olson, F. Marchesoni, and F. Nori, Phys. Rev. Lett. **83**, 5106 (1999).

[113] D. López, W. K. Kwok, H. Safar, R. J. Olsson, a. M. Petrean, L. Paulius, and G. W. Crabtree, Phys. Rev. Lett. **82**, 1277 (1999).

[114] Y. Paltiel, E. Zeldov, Y. Myasoedov, M. L. Rappaport, G. Jung, S. Bhattacharya, M. J. Higgins, Z. L. Xiao, E. Y. Andrei, P. L. Gammel, et al., Phys. Rev. Lett. **85**, 3712 (2000).

[115] A. a. Babaei Brojeny and J. Clem, Phys. Rev. B **64**, 184507 (2001).

[116] J. Clarke, Philosophical Magazine **13**, 115 (1966).

[117] P. L. Gammel, L. F. Schneemeyer, and D. J. Bishop, Phys. Rev. Lett. **66**, 953 (1991).

[118] H. Safar, P. L. Gammel, D. J. Bishop, D. B. Mitzi, and A. Kapitulnik, Phys. Rev. Lett. **68**, 2672 (1992).

[119] J. R. Clem and A. Sanchez, Phys. Rev. B **50**, 9355 (1994).

VITA

NAME OF AUTHOR: Kang Yu

PLACE OF BIRTH: Anshun, Guizhou, China

DATE OF BIRTH: October 29, 1976

GRADUATE AND UNDERGRADUATE SCHOOLS ATTENDED:

Syracuse University, Syracuse, New York

Central University for Nationalities, Beijing, China

DEGREES AWARDED:

Certificate of Advanced Study in
Information Systems and Telecommunications Management, 2009
Syracuse University

Bachelor of Science in Applied Physics, 1998
Central University for Nationalities

PROFESSIONAL EXPERIENCE:

Teaching Assistant, Syracuse University, 2006

Sales Engineer, Beijing JONES Co., Ltd, Beijing, China, 2003

Research Assistant, Institute of Electrical Engineering
Chinese Academy of Sciences, Beijing, China, 2002